Thermodynamic Properties and Structure of Aqueous Fluids in Geological Processes

Inaugural-Dissertation

zur

Erlangung des Doktorgrades

der Mathematisch-Naturwissenschaftlichen Fakultät

der Universität zu Köln

vorgelegt von

Johannes Stefanski

aus Weimar

Köln, 2020

INSTITUT FÜR GEOLOGIE UND MINERALOGIE

Öffentliche Verteidigung: 26.09.2019, Universität zu Köln, Institut für Geologie und Mineralogie, Zülpicher Strasse 49b

Promotionskommission: Prof. Dr. Georg Bareth, Universität Köln (Vorsitzender)
Prof. Dr. Sandro Jahn, Universität Köln (Erstgutachter)
Prof. Dr. Thomas Wagner, RWTH Aachen (Zweitgutachter)

ACKNOWLEDGEMENTS

I wish to express my gratitude to Prof. Dr. Sandro Jahn for the supervision of my PhD project. In particular, for the support in scientific paper writing as well as the preparation of conference presentations and the inspiring discussions over the last years. I want to especially thank Dr. Clemens Prescher for his patient training in the performance of high pressure experiments and data analysis. Furthermore, also Dr. Christian Schmidt who helped me in the beginning of my PhD to construct a hydrothermal diamond anvil cell and showed me how to perform experiments with this device. Just as well Gunther Pillunat for his collaboration in planning and in constructing the in house diamond anvil cell heating system. I would also like to thank Dr. Sergio Speziale for the support and help to carry out high pressure experiments in combination with Brillouin spectroscopy in a side project of my PhD study. For helpful discussions regarding solute complexation and aqueous geochemical modeling I want to thank Prof Dr. Thomas Wagner. Moreover, I also want to thank Prof Dr. Ladislav Bohatý for providing BeO samples for experiments in the first year of my PhD.

I owe a great debt of gratitude to the Deutsche Forschungsgesellschaft that financed parts of this PhD work in the framework of the project: JA 1469/10-1, as well as the Gauss Centre for Supercomputing e.V. for funding this thesis by providing computing time through the John von Neumann Institute for Computing (NIC) on the Supercomputer JUQUEEN, JURECA and JUWELS at Jülich Supercomputing Centre (JSC).

I wish to thank Ivonne Gebhard for her great support during the last years as well as my parents Christina Stefanski and Dr. Reiner Stefanski for many years of unrestricted support over my bumpy course of education. Furthermore, Laura Ritterbach and Linda Kerkhoff for their kind office collaboration. Last but not least I want to thank all colleagues for the pleasant working atmosphere during my time in Cologne.

ZUSAMMENFASSUNG

Wässrige geologische Fluide treten in allen Bereichen unseres Planeten und anderen terrestrischen Körpern auf. Sie spielen nicht nur eine wichtige Rolle bei der Entstehung des Lebens, sondern auch bei Prozessen in der Erdkruste und des Erdmantels, z.B. bei der Metasomatose. Die Verbindung von makroskopischen Besonderheiten von Materialien der Erde mit den Eigenschaften auf der molekularen Skala war jeher ein zentrales Anliegen der Mineralogie und Petrologie. Dennoch ist die Beschreibung von strukturellen und thermodynamischen Eigenschaften dieser Fluide bis heute nicht voll erfasst. Experimentelle Studien mittels hydrothermaler Autoklaven, Druckbehälter oder hydrothermaler Diamantstempelzellen in Verbindung mit spektroskopischen und potentiometrischen Untersuchungen sind limitiert in ihrem Temperatur-, Druck- und chemischen Zusammensetzungsbereich. Seit dem Ende des letzten Jahrtausends sind Molekulardynamik Computersimulationen ein fester Bestandteil der Untersuchungen von wässrigen Lösungen auf der molekularen Skala. Mit Beginn dieses Jahrhunderts ist es, dank weitreichender Entwicklungen in der Computertechnologie, sogar möglich, *ab initio* Molekulardynamik Simulationen durchzuführen. Diese liefern neue Einblicke in die Gesteins-Fluid Wechselwirkung und außerdem wichtige Beiträge für das Verständnis von experimentellen Ergebnissen.

In dieser Arbeit wurden drei aquatische geochemische Systeme mittels *ab initio* Molekulardynamik in Verbindung mit neuesten Methoden zur Untersuchung des Konfigurationsraumes studiert. In der ersten Fallstudie wurde die Assoziation von Yttrium, als ein Vertreter der Gruppe der schweren Seltenen-Erdelemente, mit Chlor und Fluor untersucht. Es konnte nicht nur gezeigt werden, dass Yttrium-Fluor Komplexe stabiler sind als Yttrium-Chlor Komplexe. Vielmehr sollten schon geringe Fluoraktivitäten im Fluid ausreichen, um diese zu bilden. Darüber hinaus wurde entdeckt, dass die Protolyse von Wassermolekülen in der Umgebung des Yttrium-Ions unter extremen Druck- und Temperaturbedingungen ansteigt. Diese Beobachtung scheint übertragbar auch auf andere sogenannte „high field strength elements“ zu sein.

In der zweiten Fallstudie wurde das Verhalten von Beryllium in konzentrierten fluorreichen hydrothermalen Fluiden untersucht. Dabei zeigte sich, dass Beryllium zu einer trigonalen Koordination unter hydrothermalen Hochtemperatur-Bedingungen tendiert, im Gegensatz zu der

stabilen tetraedrischen Koordination unter Raumbedingungen. Diese Beobachtung deutet auf eine höhere Mobilität von Beryllium in hydrothermalen Lösungen hin, als bisher angenommen wurde. Des Weiteren konnte eine Inkonsistenz der tabellarisierten thermodynamischen Daten von aquatischen Beryllium-Fluor Komplexen in der weitverbreiteten „slop89.dat“ Datenbank entdeckt werden.

In der letzten Fallstudie dieser Arbeit wurden die Änderungen der Hydratation des Fluorid-Ions und der Flusssäure mit steigender Temperatur und Kompression untersucht. Es ist dies die erste Studie zu den molekularen Eigenschaften von Fluor-Speziationen in wässrigen Fluiden unter Druck- und Temperaturbedingen der Erdkruste und des oberen Erdmantels. Sie liefert damit wichtige Informationen über die Wechselwirkung des Halogens mit dem Lösungsmittel. Darüber hinaus konnte die Säurekonstante von Flusssäure in dem untersuchten Bedingungsbereich bestimmt werden. Die Resultate könnten wichtige Erkenntnisse für die Rolle des Fluor bei der Mobilisierung und dem Transport von Metallionen in hydrothermaler Lösung unter extremen Druck liefern.

Es hat sich aber auch gezeigt, dass noch mehr Erfahrung und neue Konzepte für die Verbindung von klassischen thermodynamischen Datensätzen und atomarer Computersimulation nötig sind.

ABSTRACT

Aqueous geological fluids occur on the surface and in great depth on our planet and other terrestrial bodies. They play an important role in the origin of life, and further in processes of the Earth's crust like the genesis of economically significant ore deposits and metasomatism down to the Earth's mantle. The relations between the molecular scale and macroscopic properties of earth materials is in the focus of mineralogy and petrology. But the development of structural and thermodynamic models of geological fluids are still a great challenge today. Experimental studies at high temperature and high pressure use devices like hydrothermal autoclaves, pressure vessels or heated/hydrothermal diamond anvil cells in combination with spectroscopic or potentiometric measurements that are limited in pressure, temperature and composition range.

Since the end of the last millennium, molecular dynamics have become an important tool to investigate not only molecular structural changes of solvents, but also thermophysical properties of solutes in geological fluid were investigated on a molecular scale. In the current century thanks to computer technology revolutions *ab initio* molecular dynamics simulations provide new insight into rock-fluid interaction processes and support the interpretations of experimental results.

In this thesis, three different aqueous geochemistry systems are investigated using *ab initio* molecular dynamics in conjunction with advanced free energy sampling methods. Firstly, the free energy of yttrium-halide (F fluorine, Cl chlorine) aqueous complexes formation were probed by constrained *ab initio* molecular dynamics. In this case study it was found that yttrium drives the self-ionization in vicinal water molecules. Further stable Y-Cl/F complexes are found and there thermodynamic stabilities can be reported. This results have revealed that yttrium builds more stable complexes with fluorine than with chlorine. Therefore, very low F activity enables the formation of Y-fluorine complexes. Secondly, the behavior of beryllium in fluorine rich hydrothermal fluid was investigated. It was shown that beryllium tends to form a trigonal coordination at high temperature conditions in comparison to tetrahedral coordination at ambient conditions. That change might cause a higher solubility of beryllium in hydrothermal brines as known from its geochemical relative zinc. Furthermore, in this case study

inconsistencies of the widely used thermodynamic database slop98.dat regarding to aqueous beryllium complexes are discovered. In the last case study, new insight into the behavior of fluorine and hydrofluoric acid in aqueous solution with increasing temperature and compression were gained. Moreover, acidity constants of hydrofluoric acid using novel sampling methods were derived. This thermodynamic data might lead to a better understanding of the role of fluorine for the transport of metal ions in geological fluids under very high pressures.

The *ab initio* simulations presented in this thesis do not only provide a detailed insight into the molecular structures of matter, apart from that they enabled the access of thermodynamic properties such as species stability constants or acidity constants. But more experience and new correlation models are necessary to combine results of this simulation with ordinary derived thermodynamic properties of electrolytes and non-electrolytes at elevated temperature and pressure conditions.

TABLE OF CONTENTS

LIST OF ILLUSTRATIONS

LIST OF TABLES

NOMENCLATURE

Acronyms

ab initio	general meaning *from the beginning*, in context of this thesis: all calculation only based on fundamental natural constants
AIMD	*ab initio* molecular dynamics
CV	collective variable
CN	coordination number
DB	Debye-Hückel
FES	free energy surface
HKF	Helgeson-Kirkham-Flowers (model)
IAPWS	International Association for the Properties of Water and Steam
L	ligand
MD	(classic) molecular dynamics
metaD	metadynamics
M	metal ion
ML_n	metal complex with n ligands
MOR	mid-oceanic ridge
MORB	mid-oceanic ridge basalt
PP	pseudopotentials
ps	picosecond
RB	Ryzhenko–Bryzgalin (model)
REE	rare earth elements
TI	thermodynamic integration
UHP	ultra high pressure
USGS	United States Geological Survey
WTmetaD	well-tempered metadynamics
XC	exchange-correlation functional

Fundamental physical constants

k_B	Boltzmann constant ($1.38065 \cdot 10^{-23}$ m^2kg/s^2K)

N_a	Avogardo constant ($6.0221 \cdot 10^{23}$ mol^{-1})
R	ideal gas constant (molar gas constant) (8.31446 $J/K\,mol$)

Superscripts

$^\circ$	refers to the standard or reference state
*	refers to stability constant that involves further transition states

Subscripts

aq	dissolved in aqueous solution
g	gas
H_2O	properties refer to pure water
i	any specified species or component
sat	saturated water pressure
s	solid
r	refers to a reaction

THESIS ORGANIZATION

This thesis is divided into four main parts. The first part includes a general introduction to the topic and the methodology in chapter 1 and 2. It is followed by the main part that is constructed of three case studies of different aqueous geochemistry systems. For every case, the subject of the study is outlined in context of current scientific knowledge, its aim and case specific methods and approaches are described in chapters 3,4 and 5. Moreover, for each study results and possible implications are discussed. In the third part, the reader finds an overall discussion and conclusion with a outlook for further studies building upon this thesis. The last part includes the bibliography and an appendix with computing codes of the thermodynamic modeling that were used and a declaration of originality.

Chapter 1

GENERAL INTRODUCTION

1.1 Geological Aqueous Fluids

Geological aqueous fluids are key agents in many geological processes ranging from the surface to the deep interior of the Earth and other terrestrial plants [Harlov and Aranovich, 2018]. Their interaction with minerals and rocks results in alterations including the dissolution and precipitation of minerals and/or the exchange of chemical elements and isotopes. Fluid-mediated elements and energy transport are important processes, e.g. of deep element cycles in subduction zones (for more detail see Manning [2004], Manning et al. [2013], Keppler [2017]) or during the formation of magmatic-hydrothermal ore deposits (e.g see Hedenquist and Lowenstern [1994], Ridley [2013]). In geochemistry, aqueous phases are commonly distinguished according to their state of matter as liquids or rather aqueous solutions, vapors and supercritical fluids. This distinction does depend on the pressure (P) and temperature (T) of the geological environment where these phases occur [Pokrovski et al., 2013]. These phases are never pure substances, they contain a variety of elements. But the main solvent is H_2O in the Earth's crust, upper-mantle and even in the lower-mantle as recent discoveries by Tschauner et al. [2018] of water in diamond inclusions indicate. Moreover, there are numerous evidences that at least for deep fluids carbon (CO_2) can be a main component or even the dominate solvent [Manning et al., 2013].

Our knowledge about these phases derives from a variety of observations in nature: on the one hand, from direct probing of released solutions [Foustoukos and Seyfried, 2007] in geothermal systems, e.g. in hot springs on the continents or in black and white smokers on the mid-ocean ridge (MOR) and the sea floor. Here, meteoric water and seawater migrates 4-8 km deep and is heated up to temperatures of ~400 °C and returns density driven to the surface [Klein et al., 1977, Bibby et al., 1995, Arnórsson et al., 2007]. On the other site, there are fluid inclusions, primary hosted in ore forming or pegmatitic related rocks [Seward et al., 2014] but also in low and high grade metamorphic rocks [Touret, 1977, Ferrando et al., 2005]. They are fundamental information carriers for geologist and mineralogists. The methodology

to investigate the origin, physical properties and composition of this microscopic inclusions (for an overview see Van den Kerkhof and Hein [2001]) was developed and improved over the last decades, since the first scientific description of a fluid inclusion by Sorby [1858]. Furthermore, experiments like in-situ UV-Vis [Wincott and Vaughan, 2006], X-ray absorption spectroscopy [Sanchez-Valle, 2013] and numerical modeling based on thermodynamic data e.g. [Barnes et al., 1966, Sverjensky, 1987, Shock and Helgeson, 1988, Sverjensky, 2019] are essential tools to study processes and properties of such solutions. But there are still many open questions in terms of the chemistry and transport properties of geological fluids. Besides the lack of thermodynamic and speciation data for complex fluids at high temperature and high pressure, existing thermodynamic models have clear limitations [Dolejš, 2013, Seward et al., 2014]. While further experimental efforts are indispensable for providing missing information, molecular dynamics (MD) and *ab initio* molecular dynamics (AIMD) simulations have become a powerful alternative approach to study the structure and thermodynamics of aqueous fluids [Driesner, 2013, Sherman, 2010] .

Aqueous Fluid in Metasomatic Processes

In subduction zones where oceanic and continental material is transported into the Earth's mantle, a geotherm evolves that is characterized by rapid increase in pressure, but less in temperature in comparison to the oceanic or continental geotherm (see Fig. 1.1 and for more details Winter [2009] chapter 16). During the subduction process, water rich minerals such as amphibole, serpentine, lawsonite, phengite and other hydrous solid phases [Schmidt and Poli, 1998, Ulmer and Trommsdorff, 1995, Crawford and Fyfe, 1965, Domanik and Holloway, 1996, Zheng et al., 2016, Wunder, 1998] become unstable and release water into the system. Furthermore, partial melting of crustal or mantle rocks leads to the release of high density aqueous phases in the subducted slabs [Zheng et al., 2011]. But there are more sources of geological aqueous fluids. As has been pointed out, sea and meteoric surface waters have the ability to serve as H_2 sources in deep crustal hydrothermal systems [Yardley and Bodnar, 2014]. Therefore, they undergo a downward penetration or upward infiltration after being transported as pore fluid into the subduction process. But it is generally accepted that this kind of water source is not the main source for deeper processes in the Eath's crust or mantle due to the decreasing amount of porosity with proceeding diagenesis. It is expected, that only one third

of the initially subducted water reaches the subarc and postarc depths and enters the Earth's mantle [Hacker, 2008].

The knowledge of the composition of subduction zone fluids is primarily derived from chemical analysis of island-arc basalt [Manning, 2004, Métrich and Wallace, 2008] and veins in ultra-high-pressure (UHP) metamorphic rocks (e.g. Svensen et al. [2008], Zhang et al. [2008], John et al. [2011]). Deep aqueous fluids are mixtures of different ingredients: H_2O, gases (mainly CO_2) , salts and host rock oxide components like SiO_2, Al_2O_3 etc. [Manning, 2018]. Field observations of rare halite minerals, fluid inclusions, and high chlorine content of UHP minerals are interpreted as evidence that these fluids are brines [Trommsdorff et al., 1985, Touret, 1977, Newton et al., 1998, Markl and Bucher, 1998]. Because of changes in electrical conductivity with depth in subducted oceanic crust, it is assumed that there is a salinity range between 0.2 and 7.0 wt% [Bucher and Stober, 2010, Sakuma and Ichiki, 2016, Sinmyo and Keppler, 2016] but even higher concentrations are realistic [Métrich and Wallace, 2008, Manning, 2018].

The dissolution of chlorine, fluorine and other anions dramatically increases the solubility potential of minerals at high pressures and high temperatures [Manning and Aranovich, 2014]. The reasons for that are discussed in section 2.1. In general, the presence of a hydrous phase in a metamorphic system has dramatic impact on the mineral formation. Not only that the stability field of UHP minerals changes dramatically as shown in numerous experiments (reviewed by Kawamoto [2006], Ohtani and Litasov [2006], Beran and Libowitzky [2006]), it leads to a fast kinetics of mineral reactions and enables a large-scale mineral replacement on a rather short time scale [Putnis and John, 2010]. Furthermore, a massive increase in the mobility of trace-elements is reported in a variety of field studies [Ayers, 1998, Scambelluri and Philippot, 2001, Kamber et al., 2002, Harlov et al., 2006]. Therefore, a subduction zone fluid can change the geochemical signatures of petrological processes [Winter, 2009, John et al., 2011, Manning, 2004, Keppler, 2017].

Ore deposits are geochemical anomalies, because one or more elements are significantly enriched in comparison to the Earth's crustal average. These sites on our planet are particularly important for humanity, because they are an industrial source of metals as for instance Cu, Au,

Zn, REE, Be etc. for technological application. In hydrothermal ore deposits, ore minerals are precipitated from a high temperature aqueous phase. Those deposits are formed associated with small clusters of magmatic dykes or large intrusion bodies as for example rare earth element deposits [Chakhmouradian and Zaitsev, 2012, Kynicky et al., 2012, Williams-Jones et al., 2000]. In general, those intrusion bodies are formed by melts that segregate from large plutons and migrate upwards in the crust a few kilometers below the surface. The main heat source of these hydrothermal solutions is the magmatic crystallization process [Shmulovich et al., 1995], whereas the water sources of hydrothermal fluids are very diverse. One source is the decomposition of an immiscible aqueous phase from a highly fractionated melt in the late stage of igneous rock formation [Winter, 2009, Philpotts and Ague, 2009]. Here, volatile components (H_2O, CO_2, HCl, CH_4, H_2S, SO_2 etc.) of the silicate or carbonatite melt start to separate due to decreasing solubility in the melt with decreasing pressure. Moreover, groundwater from the aquifer, meteoric or ocean waters migrate to the intrusion body and are heated up [Yardley and Bodnar, 2014]. There are two main sources of elements that are carried by the hydrothermal solution. Firstly, elements that are incompatible in crystalline phases e.g. tin, gold etc. Their concentration depends on the fractionation degree of the melt and the origin of it in respect to the source rocks for the melting proceed as mantle or continental material (e.g. formation of s-type granite). Secondly, the aqueous fluid migrates through the host rock after it is decomposed from the melt and there it can dissolve huge amounts of matter. The dissolution properties of the aqueous fluids will be discussed in the next chapter in more detail. In the next step, the saturation of certain elements or components results in mineral precipitation. This saturation depends on the physical conditions such as temperature or pressure and on the composition of the aqueous phase. Furthermore, the history of exsolution is a controlling factor. Depending on the point in time on the magmatic pathway, where the aqueous fluid is released in the host rock, the water content can change dramatically [Ridley, 2013]. This factor changes depending on the distance in respect to the magmatic center and therefore different mineralization zones can be distinguished in hydrothermal ore deposits.

These ore-forming solutions can be extremely enriched in NaCl, i.e. up to 45 wt% [Banks et al., 1994] or even 80 wt% [Naumov et al., 2011]. As shown in Fig. 1.1 b, they occur under much lower pressure conditions than in a subduction zone setting. The aqueous solutions

in an ore formation process (e.g low and high-sufidation gold and copper deposits [Ridley, 2013] or beryllium deposit [Beus, 1966]) have a higher density above 350 kg/m^3 and below ~1000 kg/m^3 [Pokrovski et al., 2013], whereas volcanic vapors are characterized by a lower density (see Fig. 1.1).

1.2 Basic Properties of Geological Aqueous Fluids

Fig. 1.1 shows a P vs. T diagram of the different water phases with important physical properties. In Fig. 1.1a a distinction is made between fluids, vapors and aqueous solution [Pokrovski et al., 2013]. According to petrology textbooks by Winter [2009] and Philpotts and Ague [2009] the term fluid refers to the supercritical state. This state of matter was discovered by Baron Charles Cagniard de la Tour in 1822. When crossing the critical point of a system (see Fig. 1.1 for H_2O) and leaving the two phase field (vapor and liquid) toward a one phase field, the so-called supercritical fluid appears. Since its discovery, thousands of studies have been carried out and numerous industrial applications have been developed.

The molecular water structure at ambient conditions is characterized by a large network structure. It is build up by hydrogen bonds between the water molecules where one H_2O is coordinated by four other molecules (see e.g. Laasonen et al. [1993], Eisenberg and Kauzmann [2005] for further details). Many of the unique physicochemical properties of pure liquid water [Debenedetti and Klein, 2017] and its density anomaly are constraint to this highly connected network [Errington and Debenedetti, 2001]. But these properties dramatically change under supercritical conditions [Galli and Pan, 2013], as the number of hydrogen bonds decreases and therefore, the network is substantially distorted. It is still a matter of debate, how large the formed clusters are or if they even exist [Sahle et al., 2013, Sun et al., 2014]. Below the critical point, the conditions where hot aqueous solution occurs, are divided in katathermal (350-300 °C), mesothermal (300-200 °C) and epithermal (200-100 °C).

The reason for the classification of aqueous phases (liquid like and vapor) in Fig 1.1a in terms of water density is not only that this parameter varies over several orders of magnitude within the P/T range of terrestrial processes, it is much more important that the solvent properties of aqueous phases are often much better described in terms of density and temperature, rather than pressure and temperature [Dolejš and Manning, 2010, Mesmer et al., 1988]. Therefore,

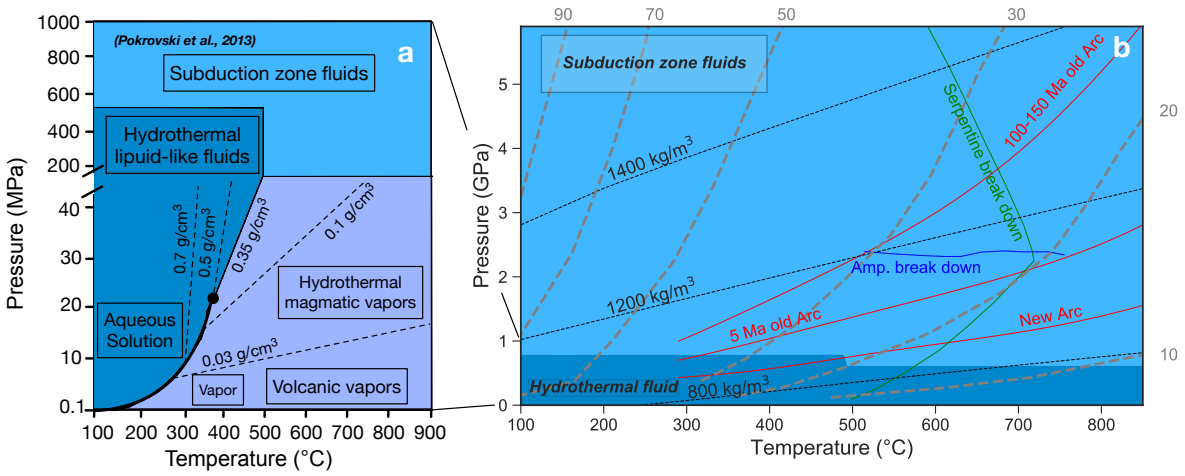

Figure 1.1: (a) a water phase diagram in the range of 100 - 900 °C and 0.1-1000 MPa. The black thick line represents the water vapor pressure curve up to the critical point marked with a black circle. The assignment of the different fields are made according to Pokrovski et al. [2013]. (b) shows the water phase diagram within a geological relevant P-T range. The black dotted shows isochores of pure water calculated using the equation of state report by Zhang and Duan [2005] and the gray dashed line and gray numbers represent the dielectric constant [Sverjensky et al., 2014]. The red lines are geotherms for different arc ages with a subduction rate of 3 cm/yr transcript from [Winter, 2009]. The green line represents the break down of serpentine [Ulmer and Trommsdorff, 1995] and the blue line of amphibole [Schmidt and Poli, 1998] (graph adopted from Keppler [2017]).

the capacity of those phases to carry and fractionate elements or dissolve minerals is quite different. Furthermore, the density difference of the fluid to the host rock is the driving force for the movement of fluids in different geological environments (see Philpotts and Ague [2009] chapter 21 for more details). Nevertheless, temperature and pressure are the physical quantities that are mainly used in the earth science community to constrain changes of physicochemical properties of matter.

It was an important task to develop equations of state of pure water which enable density information at high temperature and high pressure. Numerous experiments were performed in the past to measure the specific volume of H_2O (e.g. Burnham et al. [1969]). In geochemistry and petrology the very precise equation of state by the IAPWS[1] [Wagner and Pruß, 2002] is widely used in its validity range up to 1000°C and 1000 MPa. Furthermore the equation can be extrapolated to higher P/T conditions, with increasing uncertainty. By considering Fig. 1.1 b it is necessary to know the density of water at a much higher pressure than the IAPWS equation is applicable. Therefore, the equation of state provided by Zhang and Duan [2005] obtained

[1] International Association for the Properties of Water and Steam

from a molecular dynamics simulation is frequently used in earth science (e.g. Sverjensky et al. [2014], Keppler [2017]). Additionally, Mantegazzi et al. [2013] derived an equation from in-situ Brillouin spectroscopy of pure H_2O and NaCl+H_2O solution (up to 4.8 molar) for pressure up to 4.5 GPa and temperature up to 800°C. All three equations are compared in Fig. 1.2. At T=100 °C, the equations by Zhang and Duan [2005] and [Mantegazzi et al., 2013] provide too low ρ_{H_2O} values in comparison to experimental results [Bridgman, 1935] (below 100 MPa and 500 MPa) , whereas the IAPWS equation of state is able to reproduce the experimental data quite accurately. Therefore, this equation is much more appropriate for low pressure applications. For 400 °C and 1000 °C, all three equations provide very similar ρ_{H_2O} values.

The most important property of geological aqueous fluids is their capability to dissolve minerals. This is a two-step process, where first the solid phase (s) e.g. MX_s is dissolved and secondly an aqueous species is formed. This process can be outlined by a series of chemical equilibria [Borg and Dienes, 1992, Anderson, 2009, Dolejš and Manning, 2010], e.g. for the hydration of a metal M as $M(H_2O_n^{z+})$:

$$MX_s \rightarrow M^{z+} + X^{z-}$$

$$M^{z+} + n\,H_2O \rightarrow M(H_2O)_n^{z+}$$

where z^+ and z^- are the charges of the dissolved ions and n represents the hydration number. Such an equation can also be applied to ion pairs or neutral complexes. The thermodynamic potential of this dissolution reaction ($\Delta_{sol}G$) is a function of the reaction enthalpy ($\Delta_{sol}H$) and entropy ($\Delta_{sol}S$):

$$\Delta_{sol}G = \Delta_{sol}H - T\Delta_{sol}S \tag{1.1}$$

the enthalpy refers to a heat change due to bond breaking in the solid and the interaction with solvent. The excellent solvent properties of water at ambient conditions depend on its extremely high dielectric constant (ϵ_{H_2O}), and therefore, a strong solute solvent interaction, whereas the entropy increases due the separation of water molecules from the ordered hydrogen bonding network and the reorganization of the water molecules around the solute. But for the majority of solids (e.g. NaCl) the dissolution is driven by the change of $\Delta_{sol}H$ at ambient conditions.

The dielectric constant of aqueous fluids in the Earth's crust increases with pressure but decreases much stronger with temperature as is shown in Fig. 1.1 b. First experiments to investigate the change in ϵ_{H_2O} with increasing temperature and pressure conditions were performed

by Heger et al. [1980] up to 500 MPa and 550 °C followed by Pitzer [1983], Franck et al. [1990] and Fernàndez et al. [1997], who extend the data base up to 1200 MPa and 600 °C. But not until recent years, when starting to use *ab initio* molecular dynamics, it was possible to compute ϵ_{H_2O} up to very high pressure [Pan et al., 2013, Sverjensky et al., 2014].

With declining ϵ_{H_2O}, the driving force of dissolution in the aqueous phase changes substantially, particularly at supercritical conditions. Here, the association of the dissolved solutes become much stronger. Therefore, the chemical potential of the formed aqueous species becomes a controlling parameter for the dissolution of material in aqueous fluids.

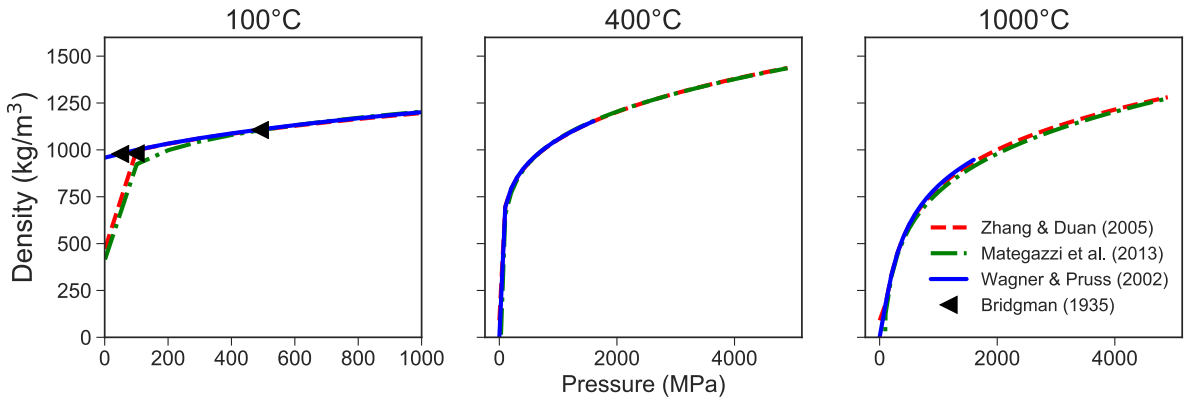

Figure 1.2: Comparison of the equation of state reported by IAPWS [Wagner and Pruß, 2002], Zhang and Duan [2005], Mantegazzi et al. [2013] in a density vs. pressure diagram. Together with experimental data by [Bridgman, 1935].

1.3 Aim of this Theses

The aim of this study is to gain new insight into the physicochemical properties of important solutes in natural aqueous environments at extreme P/T conditions from *ab initio* molecular dynamics simulations. To better understand the transportation and mobilization of this components in hydrothermal and metasomatic systems.

PUBLISHED CONTENT AND CONTRIBUTIONS

Chapter 3 is based on a manuscripts that will be published in the journal *Solid Earth* in 2020:

- J. **Stefanski**, S. Jahn.Yttrium speciation in subduction zone fluids from ab initio molecular dynamics simulations.

Beside the presented case studies that constructed this PhD thesis, I contributed to the following publications during my PhD studies:

- J. **Stefanski**, C. Schmidt, and S. Jahn. Aqueous sodium hydroxide (NaOH) solutions at high pressure and temperature: insights from in situ Raman spectroscopy and ab initio molecular dynamics simulations. *PCCP*, 20(33):21629–21639, 2018.
  contribution: Results based on simulations and experiments I performed in the framework of my master's thesis. This simulations were extended and more deeply analysed.

- C. Sahle J. Niskanen, C. Schmidt, J. **Stefanski**, K. Gilmore, Y. Forov, S. Jahn, M. Wilke, C. Sternemann. Cation hydration in supercritical NaOH and HCl aqueous solutions. *J. Phys. Chem. B*, 121(50):11383-11389, 2017.
  contribution: Performance of *ab initio* simulations on the $NaOH_{aq}$ system that were used to support experimental results.

- C. Prescher, V. B Prakapenka, J. **Stefanski**, S. Jahn, L. B. Skinner, Y. Wang. Beyond sixfold coordinated Si in SiO_2 glass at ultrahigh pressures. *PNAS*, 114(38):10041-10046, 2017.
  contributions: Performance of *ab initio* simulations and analysis of resulting data that supported experimental observations.

- C. Prescher, Yu. D. Fromin, V. B. Prakapenka, J. **Stefanski**, K. Trchenko, V. V. Brazhkin. Experimental evidence of the Frenkel line in supercritical neon. *Phys. Rev. B*, 95(13):134114, 2017.
  contribution: Preparation of the experimental devices and supporting the performance of the experiments.

Chapter 2

METHODS

2.1 Thermodynamic Approaches

Thermodynamics of Aqueous Species

The capacity of a fluid to host a certain element or to dissolve a certain amount of a phase depends on the chemical potential (μ_i) of the relevant solute species (i) [Anderson, 2009]:

$$\mu_i = \left(\frac{\delta G_i}{\delta n_i}\right)_{T,P,n_{j\neq i}} \tag{2.1}$$

where G_i is the Gibbs free energy of i, n_i is the number of moles of i in the system (all components j). For a certain P/T condition the chemical potential can be represented as:

$$\mu_i = G_i^\circ + RT \ln m_i \tag{2.2}$$

where G_i° is the standard Gibbs energy of the solute i and the molality m_i. The standard state for a solute in an aqueous solution is a 1 molal hypothetical solution with the properties of an infinitely diluted solution [IUPAC, 1982][1]. Because aqueous fluids are not infinity diluted and the chemical potential has to be independent of the choice of the standard state and the components interaction [Dolejš, 2013] the relation changes to:

$$G_i = G_i^\circ + RT \ln a_i \tag{2.3}$$

a_i, the activity of the solute depends on the concentration and the activity coefficient γ_i of the species i in the solution.

$$a_i = \gamma_i m_i \tag{2.4}$$

The activity coefficient γ_i is needed to take into account the interaction forces of ions in higher concentrated solutions. Especially the Coulombic force is mainly operating on the solutes and leads to a clustered distribution of the dissolved ions. As a result, the entropy of the system decreases in comparison to a random ion distribution in an ideal solution. Therefore, γ_i

[1] International Union of Pure and Applied Chemistry

determine the energetic consequence of a departure from the ideal behavior. This interaction parameter is the major challenge to high-P/T studies of aqueous natural systems. In the past, numerous approaches were developed by different authors, e.g. the ion hydration approach [Stokes and Robinson, 1948] or the Pitzer equations [Pitzer, 1981, 1987, 1991] to estimate the activity coefficient of different solutes. But the most frequently used technique to calculate γ_i in high temperature and high pressure aqueous geochemistry is the Debye-Hückel theory. It was introduced by Peter Debye and Erich Hückel in 1923 [Hückel and Debye, 1923]. They assumed that ions in a solution behave as spheres and their charge is a point in the center of this sphere. Furthermore, they assumed that the ions only interact with each other because of Coulombic forces. As a result, anions are more likely to be found near cations in solution, and vice versa. But all aqueous solutions are dielectric materials, therefore, thermal motions lead to more random distribution of the solutes. Accounting these counteracting effects, the authors developed the so-called Debye-Hückel equation which can be used to calculate the activity coefficient of solutes in aqueous solution, or rather, the deviation from an ideal behavior:

$$\log \gamma_i = -\frac{z_i^2 \, A_{DH} \sqrt{I}}{1 + \mathring{a}_i \, B_{DH} \sqrt{I}} \tag{2.5}$$

where z is the charge of the ion, $\mathring{a}$ the mean distance of the closest approach between the ions and I the ionic strength:

$$I = 0.5 \sum_{i=1}^{n} m_i z_i^2 \tag{2.6}$$

A_{DH} ($\sqrt{\mathrm{kg/mol}}$) and B_{DH} ($\sqrt{\mathrm{kg/mol\,cm}}$) are the empirical Debye-Hückel (DH) parameters:

$$A_{\mathrm{DH}} = \frac{1.8248 \cdot 10^6 \sqrt{\rho_{H_2O}}}{(T \epsilon_{\mathrm{H2O}})^{\frac{3}{2}}} \tag{2.7}$$

$$B_{\mathrm{DH}} = \frac{50.292 \sqrt{\rho_{\mathrm{H_2O}}}}{\sqrt{T \epsilon_{\mathrm{H2O}}}} \tag{2.8}$$

They depend on temperature, density and the dielectric constant of water (solvent). The first improvement of this equation was made in 1938 by C. W. Davies [Davies, 1962] and resulted in the so-called Davies equation. It enabled the equation for higher concentrated solutions by adding a linear empirical term of e.g $+0.2\sqrt{I}z^2$. Debye-Hückel type of equations were developed for hydrothermal systems [Helgeson, 1969, Helgeson et al., 1981] by implementing the B-dot model. That includes a "true" ionic strength by the correction term $\mathring{B}$ for ion-pairing and

complexing. Unfortunately, this model is only parametrized to highly concentrated NaCl+H_2O solutions within a temperature range of T=25-1000°C and up to P=500 MPa. There are only extrapolated $\mathring{B}$ values available for high pressure environments [Manning et al., 2013].

The formation of monomeric complexes in an aqueous solution develops step by step through the addition of certain ligands L to the cation M. Therefore, the formation of an ML_n complex can be written as a sequence of stepwise reactions:

$$\begin{aligned} \mathrm{M} + \mathrm{L} &= \mathrm{ML} \\ \mathrm{ML} + \mathrm{L} &= \mathrm{ML}_2 \\ &\vdots \\ \mathrm{ML}_{n-1} + \mathrm{L} &= \mathrm{ML}_n \end{aligned} \tag{2.9}$$

with the respective logarithmic reaction constants

$$\log\ K_i = -\frac{\Delta_r G_i^\circ}{2.303\,RT} \tag{2.10}$$

Having determined the reaction constants for all relevant reactions in 2.9, the stability constant (also referred as cumulative stability constants or overall stability constant) β_n of species ML_n is defined as

$$\beta_n = \log\ K_1 + \log\ K_2 + \log\ K_3 \cdots \log\ K_n \tag{2.11}$$

Combining equation 2.3 and 2.4, the standard Gibbs energy of reaction ($\Delta_r G^\circ$) depends on the reaction Gibbs energy ($\Delta_r G$), the temperature T, the gas constant R, the molality m and the activity coefficient of every solute:

$$\Delta_r G_i^\circ = \Delta_r G_i - RT\ \ln \frac{m_{ML_i}\gamma_{ML_i}}{m_{ML_{i-1}}\gamma_{ML_{i-1}} \cdot m_L \gamma_L} \tag{2.12}$$

Thermodynamic Equation of States (EOS)

Over a period of about ~50 years, the stability of major metal aqueous species was studied, and numerous thermodynamic models have been developed to predict solute formation and mineral solubility under high P/T conditions [Barnes, 1979, Lindsay, 1980, Mesmer et al., 1988, Shock et al., 1989, Sverjensky et al., 1997, Akinfiev and Diamond, 2003, Oelkers et al., 2009, Dolejš,

2013, Seward et al., 2014, Sverjensky, 2019]. In this study, three different approaches to represent the pressure and temperature dependency of aqueous complex formation are used:

The *Ryzhenko-Bryzgalin model* [Ryzhenko et al., 1985, M. V Borisov and Shvarov, 1992, Shvarov and Bastrakov, 1999] is based on a common assumption [Gurney, 1953] that the Gibbs free energy of a reaction for monomeric species is a sum of two terms:

$$\Delta_r G^\circ(T,P) = \Delta_r G^\circ_{nonel} + \Delta_r G^\circ_{electr}(T,P) \tag{2.13}$$

one P and T independent nonelectrostatic term $\Delta_r G^\circ_{nonel}$ and $\Delta_r G^\circ_{electr}(T,P)$ a Coulomb (electrostatic) contribution of P and T. This P/T-term of a dissociation reaction is given by:

$$\Delta_r G^\circ_{electr}(T,P) = -|z_a z_c|_{eff} \frac{e^2 N_a}{a \epsilon_{T,P}} \tag{2.14}$$

$-|z_c z_a|_{eff}$ is the effective charge depending on the formal charges of the anion and cation, the geometry of the complex and number of ligands. e is the elementary charge, N_a the Avogadro constant and a is the sum of radii of the central ions and ligands [Plyasunov and Grenthe, 1994].

To apply this model and to explore steps of dissociation by the interpolation or extrapolation of e.g. experimental results, a linear relationship between the logarithmic reaction constants and the self-dissociation constant of water was introduced by Shvarov and Bastrakov [1999]:

$$\log K_{T,P} = \log K_{298\,\mathrm{K},\,0.1\,\mathrm{MPa}} \frac{298\,\mathrm{K}}{T} + \overline{B}_{T,P}\,(zz/a) \tag{2.15}$$

and implemented in the analysis software package HCh and OptimC [Shvarov, 2008, 2015]. Within the packages, the parameter A and the optional parameter B are fitted in terms of:

$$(zz/a) = A + \frac{B}{T} \tag{2.16}$$

The function $\overline{B}_{T,P}$ is independent of the species. It depends only on the self-dissociation constant of water:

$$\overline{B}_{T,P} = \frac{pK^{water}_{T,P} - pK^{water}_{298.15\,K,1\,bar} \frac{298.15}{T}}{(zz/a)_{water}} \tag{2.17}$$

The $(zz/a)_{water}$ parameter results in a best fit value of 1.0104 [Shvarov, 2015]. The dissociation constant of water is a function of P and T conditions. The model of Marshall and Franck [1981] provides the self-dissociation constant of water for a broad condition range (T=25-1000°C and P=0.1-1000 MPa). The big advantage of this model is the reduced number of input parameters.

Therefore, it was used in numerous studies to fit experimental data of aqueous complex of major and trace elements (e.g Tagirov and Seward [2010] and for an overview of available species parameter see Ryzhenko [2008]).

The *Helgeson-Kirkham-Flowers EOS* [Helgeson and Kirkham, 1974, 1976, Helgeson et al., 1981, Shock et al., 1992] is the most widely used model for thermodynamic modeling of aqueous systems in aqueous geochemistry. Therefore, it is implemented in numerous thermodynamic codes (e.g. SUPCRT92 [Johnson et al., 1992], SUPCRTBL[2] [Zimmer et al., 2016], Deep Earth Water Model[3] [Sverjensky et al., 2014]). This model was developed by Harold C. Helgeson and co-workers and started in the 1970s. It is a semiempirical EOS and uses a number of empirical parameters. It is based on the assumption that the change of standard Gibbs free energy when a solute is placed in a solution can be written as [Manning, 2013, Tremaine and Arcis, 2013]:

$$\Delta G^\circ = \Delta G^\circ_{intrinsic} + \Delta G^\circ_{breakdown} + \Delta G^\circ_{solvation} \tag{2.18}$$

where $\Delta G^\circ_{intrinsic}$ is constrained by intrinsic properties of the solute (partial molar volume $\overline{V}^\circ$, partial molar heat capacity $\overline{C_p}^\circ$), $\Delta G^\circ_{breakdown}$ refers to the contribution of structural change of the solvent and $\Delta G^\circ_{solvation}$ to the electrostatic interaction between solute and solvent. The first two terms are not distinguishable on an experimental scale, therefore, they sum up to non-solvation effects. They are species-specific and P/T independent in the EOS, whereas the solvation effect is treated within the Born theory. Here, the change of the Gibbs free energy is a function of the dielectric constant and the Born-parameter ω (species specific):

$$\Delta G^\circ_{solvation} = \omega \left(\frac{1}{\epsilon_{\mathrm{H_2O}}} - 1 \right) \tag{2.19}$$

The standard Gibbs free energy of a species as function of P and T is given by Shock et al.

[2] www.indiana.edu/ hydrogeo/supcrtbl.html
[3] http://www.dewcommunity.org/

[1992], Shvarov [2015]:

$$\begin{aligned} G(T,P) = G^\circ - S^\circ(T-T^\circ) + a_1(P-P^\circ) + a_2 \ln\frac{\zeta+P}{\zeta+P^\circ} \\ + \frac{1}{T-\Theta}\left[a_3(P-P^\circ) + a_4 \ln\frac{\zeta+P}{\zeta+P^\circ}\right] \\ - c_1\left[T\ln\frac{T}{T^\circ} - T + T^\circ\right] \\ - c_2\left[\frac{\Theta-T}{\Theta}\left(\frac{1}{T-\Theta} - \frac{1}{T^\circ-\Theta}\right) - \frac{T}{\Theta}\ln\frac{T^\circ(T-\theta)}{T(T^\circ-\Theta)}\right] \\ + \omega^\circ(Z+1) + \omega^\circ Y^\circ(T-T^\circ) - \omega(Z+1) \end{aligned} \tag{2.20}$$

where the index $^\circ$ refers to a reference state commonly at T°=298.15 K and P°=0.1 MPa. a_1, a_2, a_3, a_4, c_1 and c_2 are constants of a certain species i, ζ and Θ are model parameters and Z, Y are nonlinear P/T functions depending on ϵ_{H_2O}.

The *density model* [Marshall and Franck, 1981, Mesmer et al., 1988, Anderson et al., 1991] is based on an important observation in aqueous solutions under high temperature and high pressure, namely that the isothermal changes in the logarithmic dissociation constant of water and many other aqueous species correlate linearly with the logarithmic water density ($\log \rho_{H_2O}$) [Mosebach, 1955, Franck, 1961, 1956, Marshall and Franck, 1981] down to ρ_{H_2O}= 350 kg/m^3 [Tremaine et al., 2004]. This model was further developed by [Mesmer et al., 1988, Anderson et al., 1991] to permit estimations of several thermodynamic parameters at elevated pressure and temperature based on the equilibrium constant of the aqueous reactions, the enthalpy and the heat capacity at reference state (25°C,0.1 MPa). Dolejš and Manning [2010] used a density correlation model to represent the dissolution of minerals in high pressure and high temperature aqueous fluids.

Its most simplified form can be used to extrapolated equilibrium constants of aqueous dissociation reactions in P/T space:

$$\log K = m + n\log(\rho_{H_2O}) \tag{2.21}$$

m and n are polynomial fit parameters with T (K) dependency (see Anderson et al. [1991] for

more details):

$$m = m_0 + m_1 T^{-1} + m_2 T^{-2} + m_3 T^{-3} \tag{2.22}$$

$$n = n_0 + n_1 T^{-1} + n_2 T^{-2} \tag{2.23}$$

The benefit of a density model in comparison to the commonly used Helgeson-Kirkham-Flowers model is the reduced number of input parameters. Here, only the reaction equilibrium constant and the precisely known water density up to very high P/T conditions [Wagner and Pruß, 2002, Zhang and Duan, 2005] is necessary.

2.2 *Ab Initio* Molecular Dynamics

In the late 1970s and 1980s, computer systems became sufficiently fast, initialized by the evolution of semiconductor technology, that made atomistic simulations of earth materials possible. First studies were performed to investigate physical properties of minerals by using empirical or *ab initio* derived interaction potential functions (e.g., Catlow et al. [1982], Bukowinski [1985]). Huge improvements were made by computation studies focusing on the molecular structure of liquid water carried out shortly after by Berendsen et al. [1987] inducing a simple point charge (SPC) model. Important milestones were achieved by A. A. Chialvo and co-workers [Chialvo et al., 1998a,b, Chialvo and Cummings, 1999] at the end of the last millennium by correlating the local distortion of the aqueous solvent structure around solutes with macroscopic thermophysical properties. In the same time period, Cui and Harris [1995] predicted the solubility of NaCl in supercritical water with surprising accuracy using the Kirkwood coupling parameter integration supplemented by Widom's test particle method [Widom, 1963]. The investigation of the dissolution of more complex components as e.g. baryte ($BaSO_4$), was investigated more recently by Stack et al. [2012] using metadynamics [Laio and Parrinello, 2002] and umbrella sampling [Kumar et al., 1995] with significant discrepancy to experimental values. But the fast evolution of high performance computers and the access to highly scalable[4] codes such as CPMD[5] or CP2K[6] [CPMD, 1990, Marx and Hutter, 2000, Hutter et al., 2014] nowadays makes it possible to simulate aqueous solutions using *ab initio* molecular dynamics including up to a few hundred atoms. Here, great progress has been made in the last 10-15 years by investigating the molecular structure and chemical-physical properties of aqueous geological fluids (reviewed by Sherman [2010], Brugger et al. [2016]). Especially, substantial progress has been achieved in developing structure models of such fluids, in relating them to experimental observations via theoretical spectroscopy and in deriving species-related thermodynamic properties (e.g. van Sijl et al. [2010], Jahn and Schmidt [2010], Mei et al. [2013, 2016], Tagirov et al. [2019b,a]).

Theoretical Framework

Molecular dynamics is a finite difference method to solve Newton's equations of motion of a system of atoms numerically based on an atomic interaction model. The combination of *ab*

[4] in terms of calculation per CPU
[5] www.cpmd.org
[6] www.cp2k.org

initio electronic structure calculations with the molecular dynamics method (AIMD) allows to sample at the same time the structure of a condensed phase and its energy [Marx and Hutter, 2012]. The basis of molecular dynamics simulation is to compute the kinetic K and potential energy U of a system such as a fluid or a melt. The sum of these two terms provides the total energy E and can be used to describe the overall state of an atomic system (see Sholl and Steckel [2009]). E is the lowest-energy solution of the Schrödinger equation [Schrödinger, 1926] using the quantum mechanic approach:

$$\hat{H}\Psi = (\hat{K} + \hat{U})\Psi = E\Psi \tag{2.24}$$

here, Ψ is the wave function representing a set of solutions, or eigenstates, of the Hamiltonian ($\hat{H}$) of the system. The $\hat{}$ indicates an operator that represents a physical quantity of a system. The Hamiltonian, following equation 2.24 is the total energy of a system and can be further comprised in [Koch and Holthausen, 2001]:

$$\hat{H} = \hat{K}_e + \hat{K}_n + \hat{U}_{en} + \hat{U}_{ee} + E_{nn} \tag{2.25}$$

Here, the first two terms $\hat{K}_e$ and $\hat{K}_n$ refer to the kinetic energy of the electrons and the atomic nuclei. $\hat{U}_{en}$ describes the potential part of the attractive electrostatic interaction that exists between the electrons and the atomic nuclei. The repulsive potential between the electrons is accounted in $\hat{U}_{ee}$ and E_{nn} refers to the atomic nucleus-nucleus interactions (see Marx and Hutter [2012], Jahn and Kowalski [2014], Koch and Holthausen [2001] for more details).

Since Erwin Schrodinger published his famous equation to represent the atomic structure in the year 1926, it is known that it can only be solved exact for a system of one hydrogen atom because of the many-body problem (see Constantinescu and Magyari [2013]). But in the 19th century, numerous solution were proposed to overcome this problem for a system with more than one electron. One approach is so-called density functional theory (DFT) it based on a mathematical theory proposed by the authors Hohenberg and Kohn [1964].

The basic theorem behind this theory is that the ground-state energy of equation 2.24 is a unique functional of the electronic charge density $\rho_e(\mathbf{r})$ of a system. Where $\mathbf{r}$ is a particular position in space. Therefore, this function reduce the number of dimensions of the problem solving the Schrödinger equation for a multi electron system to three. For a single-electron

wave function, where $\rho_e(\mathbf{r}) = \sum_i |\Psi_i(\mathbf{r})|^2$) it can be expressed as:

$$E[\Psi_i] = E_{known}[\rho_e(\mathbf{r})] + E_{XC}[\rho_e(\mathbf{r})] \tag{2.26}$$

$E_{known}[\rho_e(\mathbf{r})]$ includes four contributions: the Coulomb interactions between the electrons and the atomic nuclei, the Coulomb interactions between pairs of electrons, the Coulomb interactions between pairs of atomic nuclei and the electron kinetic energies. All these contributions are "known", that means they can be exactly determined. Whereas, E_{XC} the exchange-correlation functional carries by definition all quantum mechanical effects. That means, by finding the right dependency of the exchange-functional on the electronic charge density ρ_i provides the total energy of the system ground state. This task was solved by authors Kohn and Sham [1965] by using a set of equations where each of the equation only involve one electron [Perdew and Ruzsinszky, 2010]. This are the Kohn-Sham equations and they can be expressed in form of plane wave functions (Kohn–Sham orbitals) [Marx and Hutter, 2012]. This approach is implemented as plane-wave calculations in the most used quantum chemistry computing cods: CPMD, VASP[7], CP2K, ABINIT[8], Quantum ESPRESSO[9].

Over the last decades several concept were developed to approximate the exchange–correlation functional. The most common one for the electronic structure in atomic systems of condensed phases such as fluid is based on the generalized gradient approximation (GGA). In geoscience, frequently used exchange-functionals (XC) are PBE [Perdew et al., 1996], PW91 [Perdew and Wang, 1992] and BLYP [Becke, 1988, Lee et al., 1988]. In this study, the BLYP functional was used for all simulation regarding to aqueous solution. Firstly, it was shown in a variety of studies that BLYP is capable to reproduce structural and dynamic properties of pure H_2O with sufficient accuracy [Sprik et al., 1996, Tuckerman et al., 1996, VandeVondele et al., 2004, Kuo et al., 2004]. Secondly, as shown by Schultz et al. [2005], this functional is well suited to compute dissociation energies of metal-ligand bonds. But at the same time, non-local interaction like van-der-Waals forces are neglected and that can lead to over bonding of the solvent structure especially at lower temperatures if no correction terms are included [Jonchiere et al., 2011].

[7] www.vasp.at
[8] www.abinit.org
[9] www.quantum-espresso.org

Car–Parrinello Molecular Dynamics

Within a AIMD, the evaluation of the forces between atoms, as described, is based on a quantum mechanical approach, but the movement of the much slower atomic nuclei is computed by classical mechanics equations. There are two major types of AIMD simulations. The first one is the Born-Oppenheimer MD (BOMD): here, in every MD time step, the electronic energy of the whole system is minimized. This leads to higher computation cost in comparison to a second type, the Car-Parrinello molecular dynamics (CPMD) [Car and Parrinello, 1985] that is primarily applied in this study. CPMD uses a fictitious dynamics to represent the electrons as quasi-particles with a fictitious mass and fictitious temperature respectively a fictitious kinetic energy [Marx and Hutter, 2012]. Both parameters have to be chosen for each case study in that way that no energy is transferred from the atomic nuclei system to the electrons. When this constraint is satisfied, the dynamics follows the ground-state of the Born-Oppenheimer energy surface. Both methods (BOMD and CPMD) usually employ periodic boundary conditions which are useful to approximate the behavior of macro-scale systems.

Due to the limited number of atoms in classical MD and AIMD simulation in comparison to condensed matter (1 mol = $6.022 \cdot 10^{23}$ atoms) surface effects are generally strong [Allen and Tildesley, 1987], because the number of atoms close to the surface is much higher than that of the atoms that are not effected by cell boundaries. Fig 2.1 shows a two dimensional illustration of the concept of periodic boundary conditions. Here, the brown square represents the simulation cell and is replicated in two directions to form an infinite lattice. In a AIMD run, as a molecule or ion moves in the central cell, its image moves exactly the same way in all the neighboring cells. If one atom leave the central cell, one of its images will enter from the opposite site. Therefore, no surface effects occur and the number density in the central cell is conserved. In the majority of the DFT based quantum chemistry compute code, the three-dimensional periodicity of long-range Coulombic interaction between the atoms in adjacent cells is taken into account by the Ewald summation technique [Marx and Hutter, 2012].

All simulations presented in this thesis were performed in the canonical ensemble , i.e. at constant number of atoms N, volume V and temperature. The average temperature was controlled using a Nosé type thermostat [Nosé, 1984, Hoover, 1985] for the ions and for the fictitious temperature of the electrons. The concept of this integral thermostat method is to

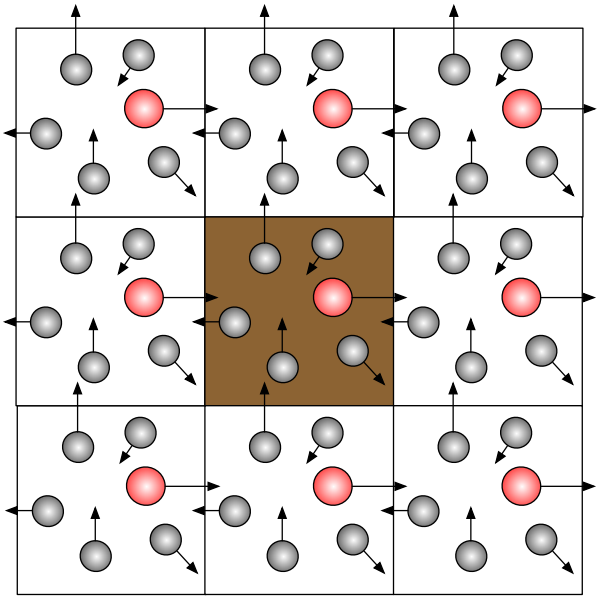

Figure 2.1: Illustration of periodic boundary conditions in two dimensions applied in *ab initio* molecular dynamics. The brown central cell is the original simulation cell, all the other cells are periodic images of the central cell.

---

connect the physical system with a thermal reservoir whose temperature remains effectively constant. The target temperature is set by the simulation temperature of the reservoir and it is coupled via a vibrational frequencies to the physical system. A higher frequency leads to a fast adjustment of the temperature, whereas a slow frequency keeps the average temperature only over a long runtime. It should be chosen in the range of characteristic vibrational frequencies of the system. Furthermore, it has to be considered, that the fluctuation of the system temperature is scaling with the number of atoms. All simulations present are carried out with an ion thermostat frequency of 2500 cm^{-1}, this is in the range of the O-H vibrations. This value gives a good compromise between the height of the fluctuations and a stable temperature evolution during the run. Very important for the CPMD simulation is the decoupling of the ion and electron thermostat [Tuckerman and Parrinello, 1994], which has been achieved by a much higher frequency of 10000-12000 cm^{-1} for the electronic system.

Pseudopotentials

Not all electrons of the atoms are included in the *ab initio* calculation. Pseudopotentials (PP) are applied to reduce the computational cost of a plan-wave DFT based simulation, especially

for periodic systems. Due to the fact that only the outer electrons or valence electrons are participating in chemical bonds, the electrons (orbitals) close to the atomic core are approximated by smooth potential functions and traded together with the nuclei. Moreover, many relativistic effects [Marx and Hutter, 2012] as for instance the contraction of the 6s shell in heavy atoms (e.g gold) [Pyykko and Desclaux, 1979] are strongly connected to the core electrons and can be incorporated in those functions. An important characteristics of PP is their transferability between different chemical environments. In the context of plane-wave calculations, norm-conserving PP [Hamann et al., 1979] are primarily used. Here, the valance electrons are represented by simplified pseudo-wavefunctions. By definition, the pseudo-wavefunctions should be identical with the all-electron wavefunction in the region where they overlap with other atom. In order to satisfy this requirement, the energies and charge densities outside a defined energetic cutoff radius have to be the same for the pseudo- and the all-electron valence states for an atomic reference state. An plane-wave energy cutoff of 80 Rydberg was a good compromise between efficiency and accuracy of the resulting molecular structure in the presented studies.

Designing proper PP is a very challenging task and only few working groups worldwide are capable to provide accurate and efficient potentials. Some of the semi-commercial e.g. VASP and open source codes e.g. CP2K include their own libraries. In this study, exclusively Goedecker-type PP[10] [Goedecker et al., 1996, Hartwigsen et al., 1998, Krack, 2005] are used. This kind of PP was widely used to compute precisely bonding and dynamic proprieties of pure water or aqueous solution at ambient conditions (e.g Pestana et al. [2017], Shi et al. [2018], Ruiz Pestana et al. [2018]) and in the critical state (e.g. Sahle et al. [2013], Stefanski et al. [2018], Jonchiere et al. [2011]).

2.3 Analysis of Interaction Distances and Coordination Numbers

The average atomic structure of a fluid is commonly described in terms of partial radial distribution functions $g_{ij}(r)$. These functions describe the probability for finding a pair of atoms of elements i and j at a distance r, normalized to the atom number density ρ_N of the fluid:

$$g_{ij}(r) = \frac{1}{c_i c_j 4\pi r^2 \rho_N N} \sum_{a=1}^{N_i} \sum_{b=1}^{N_j} \delta(r - |\vec{R}_a - \vec{R}_b|) \tag{2.27}$$

[10] www.cp2k.org/static/potentials/

where c_i (= N_i/N) and c_j are the concentrations of elements i and j, N is the number of atoms in the simulation cell, $\delta(x)$ the Dirac delta function, and $\vec{R}_a$ and $\vec{R}_b$ are the position vectors of the atoms a and b. The positions of the first maxima of $g_{ij}(r)$ represent the distances within the highest density of atomic pairs, which are commonly interpreted as the nearest neighbor distances (or bond distances) between elements i and j. Fig. 2.2 is a simplified representation of this formalism and expresses the numerical implementation of Eq. 2.27 in the molecular structure analysis. Shown is the distribution of atom B and C around the observed central atom A. It is striking that the density of the atoms B is higher around the atom A than anywhere else in this part of the system. This arrangement of atoms is called coordination shell. The radial distribution function $g_{\mathrm{AB}}(r)$ is computed by counting all B within a distance r and r+dr away from A. This list of distances is normalized in respect to the number of atoms and the volume of the cell. As a results, the green line ($g_{\mathrm{AB}}(r)$) in Fig 2.2, which now represents the distribution of B around A can be drawn.

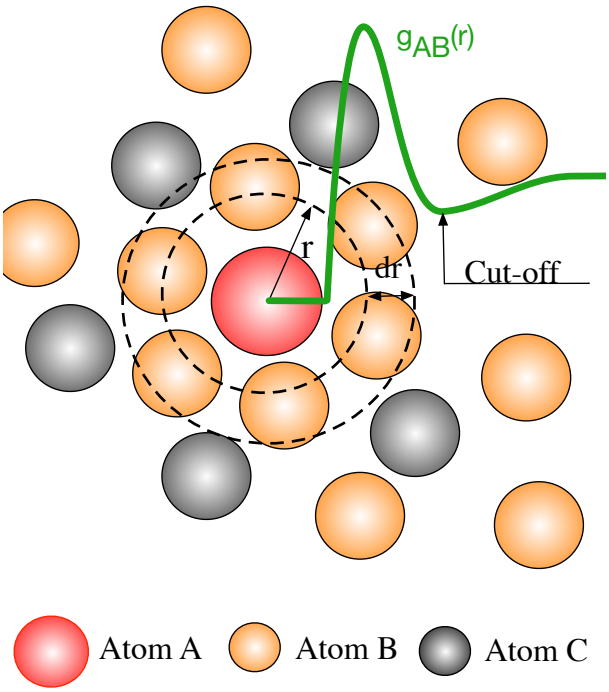

Figure 2.2: Illustration of the radial distribution function in two dimensions. See text for further explanation.

The average coordination number or hydration number[11] of certain elements is computed by simply counting the number of neighbors within a given cutoff distance respecting periodic boundary conditions and averaging overall particles of the same kind and over the AIMD time. Considering Fig 2.2 to determine the average number of B in the first coordination shell around A, the cutoff distances for the counting is taken from the first minimum of $g_{AB}(r)$.

2.4 Free Energy Sampling Methods

Classical and especially *ab initio* molecular dynamics simulations are faced with a serious problem, namely that the timescale that can be reached is severely limited as well as the system size. But dynamical processes of interest such as chemical reactions in molecular system evolve in a nano- to millisecond or even longer timescale, due to the formation of metastable states and the separation of stable states by high energies barriers. Therefore, the transition of a system within the simulation time of at most hundreds of picoseconds from one state to another becomes a "rare event" in AIMD simulations. This problem becomes more obvious if considering that in order to investigate an event like a dissociation reaction in a solution, it has to be repeated many times to gain meaningful statistics. To overcome this problem, different computational approaches have been developed over time. The most important ones are weighted histogram techniques [Kumar et al., 1995, Roux, 1995], Jarzynski's identity based methods [Jarzynski, 1997], adaptive force bias [Darve et al., 2008], thermodynamic integration [Carter et al., 1989, Sprik and Ciccotti, 1998] and metadynamics [Laio and Parrinello, 2002]. In this thesis, the thermodynamic integration in conjunction with constraint AIMD and the metadynamics are used to probe the free energies of aqueous reactions and will discussed in detail in the next sections.

For example, constrained AIMD and thermodynamic integration were used in the past to compute dissociation constant of organic [Ivanov et al., 2006] and inorganic complexes at ambient conditions [Bühl and Golubnychiy, 2007, Bühl and Grenthe, 2011] up to hydrothermal and even Earth's upper mantle P/T conditions [Mei et al., 2015, 2016, 2018]. Moreover, it was demonstrated by using the metadynamics approach that acidity constants of different acids can be computed with desirable accuracy [Tummanapelli and Vasudevan, 2014, 2015a,b, Pérez de

[11] The number of water molecules with its hydrogen respectively oxygen pointing towards the center within the first coordination shell surrounding a ion species.

Alba Ortíz et al., 2018, Sakti et al., 2018]. Furthermore, Schreiner et al. [2008] use the same approach to investigate reaction pathways of peptide synthesis under hydrothermal conditions, whereas, van Sijl et al. [2010] were able to derive hydration energies under subduction zone conditions of Ti^{4+} that correlate with recent experimental observation [Mysen, 2018].

Thermodynamic Integration

From a thermodynamic point of view, a AIMD simulation typically yields the internal energy (U) of a system, that is a potential that depends on temperature, volume (V) and entropy (S). As we are interested in processes at constant P and/or T , the Helmholtz free energy (A) and the Gibbs free energy (G) provide much more appropriate potentials for thermodynamic modeling. At a fixed number of atoms, volume and temperature the Helmholtz free energy is defined as:

$$A \equiv U - TS \tag{2.28}$$

and for a system of a specific number of atoms, at constant temperature and pressure the Gibbs free energy is defined as:

$$G \equiv A + PV \tag{2.29}$$

Thus, in equilibrium, thermal quantities are at a minimum. But the free energy or entropy as well as related quantities can not directly be measured form AIMD/MD simulation (for more detail, see Frenkel and Smit [1996] chapter 3.).

Thermodynamic integration (TI) is a well established method to quantify the free energy difference involving thermodynamic variables such as volume and temperature as integration variables of a atomic systems [Frenkel and Smit, 1996]. Further developments combine TI with constraint dynamics coupled with a certain reaction coordinate ξ [Carter et al., 1989, Resat and Mezei, 1993, Sprik and Ciccotti, 1998, Ciccotti et al., 2005]. Within the CPMD code, that was used in all presented case studies, this constraint is achieved by using the standard *SHAKE* algorithm [Ryckaert et al., 1977].

Using this method to investigate chemical dissociation reaction in aqueous solution ξ is defined as the bond distance between the central atoms and its ligand. The change in Helmholtz free energy ($\Delta_r A$) during a reaction is obtained by integrating the average force $\langle F \rangle$ between the ions from the equilibrium bond distance ξ_1 of the associated state to a bond distance ξ_2 of the

dissociated state, so that $\langle F \rangle$ vanishes at ξ_1 and ξ_2. At each ξ along the integration path, $\langle F \rangle$ is derived from a constrained AIMD simulation with a constant bond distance between the ions:

$$\Delta_r A_{\xi_1 \longrightarrow \xi_2} = -\int_{\xi_1}^{\xi 2} \langle F(\xi) \rangle d\xi \tag{2.30}$$

Formally, Gibbs and Helmholtz free energy changes are related by $\Delta_r G = \Delta_r A + \Delta_r (PV)$ according to equation 2.29. As the volume change during the dissociation reaction is assumed to be negligible in AIMD simulations at constant V, $\Delta_r G = \Delta_r A$ can be set. This assumption is made in all three case studies.

Metadynamics

Using the metadynamics (MetaD) approach, it is possible to probe the free energy surface of a reaction pathway [Barducci et al., 2011]. The MetaD enables the system to overcome local minima and to explore new regions in the configuration space within the AIMD time. Here, an external history-dependent bias potential $\tilde{V}(t, s)$ modeled by Gaussian functions is added to the Hamiltonian of the system:

$$\tilde{H}(q, p, t) = H(q, p) + \tilde{V}(t, s) \tag{2.31}$$

where the Hamiltonian of the system depends on the q momentum and p position of all atoms in the system. The bias potential is constructed by the accumulation of Gaussian functions (called "hills") in the space of selected degrees of freedom $s(p)$ called collective variables (CVs):

$$\tilde{V}(t, s) = \sum_{\tau=1}^{\tau<t} W \exp\left(- \sum_{i=1}^{d} \frac{(s_i(p) - s_i(p(\tau)))^2}{2\sigma_i^2} \right) \tag{2.32}$$

During the MetaD run, $\tilde{V}(t, s)$ is updated by adding a new hill d with a deposition stride τ, with the height W and width σ_i over the time t. There is a variety of collective variables (e.g. bonding angles, bond lengths, coordination numbers etc.), which can be implemented in the MetaD (see $PLUMED$1.3.0 manual[12]).

The reconstruction of the free energy surface in ordinary MetaD simulation can be very challenging due to insufficient criteria of the accurate convergence of the free energy profile. The main approach is to evaluate the convergence by monitoring the evolution of the collective

[12]http://www.plumed.org/documentation

variable and the free energy difference with time to distinguish between the reactive and the diffusive region of the CV (see e.g. Ensing et al. [2005, 2006]). But the bias potential can overfill or only partly fill the underlying free energy profile when the simulation is not stopped exactly at the right time. This leads to a significant increase of the error in the free energy [Barducci et al., 2011]. Therefore, Barducci et al. [2008] suggest a method called well-tempered metadynamics (WTMetaD), where a weight factor of the Gaussian is constantly re-scaled to achieve a theoretical convergence of the metadynamics:

$$W(\tau) = W_0 \exp\left(-\frac{\tilde{V}(s(q(\tau)), \tau)}{\kappa_B \Delta T}\right) \tag{2.33}$$

here, W_0 represents the initial Gaussian height, ΔT is a characteristic energy with the dimension of temperature and κ_B the Boltzmann constant. In the limit of infinite simulation time, the bias potential converges to a fraction of the exact free energy as a function of the collective variable [Barducci et al., 2008]:

$$A(s, t \to \infty) = -\frac{\Delta T + T}{\Delta T} V(t, s) - C \tag{2.34}$$

where $(\Delta T + T/\Delta T)$ is the so-called "bias factor" and characterizes the sample temperature of the collective variable (for further details see Barducci et al. [2011], Valsson et al. [2016]) and C is an immaterial constant.

Chapter 3

CASE STUDY I: YTTRIUM SPECIATION IN SUBDUCTION ZONE FLUIDS

Subduction zones have been the most important sites for exchange of matter and energy between the Earth's crust and mantle for billions of years until now [Tang et al., 2016]. Magnetotelluric anomalies (e.g. Worzewski et al. [2011], McGary et al. [2014]) suggest the occurrence of a high proportion of melts and water rich fluids in the subducted slabs. It is known that REE patterns of subducted rocks are affected by the chemical composition of the metamorphic fluid (e.g. John et al. [2008], Zhang et al. [2008]) due to their chemical complexation with dissolved anions, e.g. F^-, SO_4^{2-}, CO_3^{2-} and Cl^- [Tsay et al., 2014, 2017, Alt et al., 1993, Scambelluri and Philippot, 2001, Newton and Manning, 2010]. The distribution of these elements between minerals and fluids or melts is used as petrogenetic indicator for fractionation processes in igneous and metasomatic petrology [Winter, 2009].

The speciation of REE at moderate P (up to few 100 MPa) and high temperatures (250-300 °C) was studied experimentally using *in-situ* UV-vis, X-ray absorption spectroscopy (XAS) and solubility experiments (see recent review by Migdisov et al. [2016]) to understand physicochemical properties of hydrothermal fluids related to REE ore deposition focusing on chloride and fluoride complexes. Due to the high stability of fluoride complexes [Wood, 1990, Haas et al., 1995] it is a widely shared notion that fluoride complexes are most important for REE(III) transport in hydrothermal fluids but Migdisov and Williams-Jones [2014] suggested that REE(III)-fluoride complexes are not the major carrier of REEs due to the low solubility of REE(III) fluoride minerals such as bastnaesite, (Ce,La,Nd,Y)[FCO_3], and due to the low fluoride activity in low pH environments. According to Migdisov and Williams-Jones [2014], REE chloride and sulfate complexes appear to be the main species for REE transport in hydrothermal systems. However, this interpretation is questioned by other authors [Xing et al., 2018].

So far, the number of *in-situ* studies which address the complexation or thermodynamic properties of REE aqueous species at pressure and temperature of subduction zones is very limited due to the challenging experimental setups [Sanchez-Valle, 2013]. Besides from field

observations (e.g. fluid inclusion analysis), our main understanding of the behavior of REE under high P/T conditions is derived from fluid/mineral partition and solubility experiments (e.g. Bali et al. [2012], Keppler [1996], Tsay et al. [2014], Keppler [2017]) and from numerical simulations. In a case study, van Sijl et al. [2009] modeled the hydration shell of REEs in solution by static energy calculations of an explicit first hydration shell and an implicit solvent model. Temperature effects were introduced by considering changes of the dielectric constant of the solvent and by calculations of the entropy. In this study it is concluded that the hydration energies of all lanthanides become more similar at high P/T conditions and that the availability of ligands becomes a controlling factor for the fractionation of light REE (LREE) and heavy REE (HREE) by subduction zone fluids. Further experiments confirm that LREEs (e.g. La) are more mobile than HREE in chloride-rich solutions. Whereas the presence of fluoride in the system enable the mobility of HREE more than chlorine and leads to fractionation processes [Tropper et al., 2013, Tsay et al., 2014].

Speciation of Yttrium (Y) in Aqueous Geological Fluids

From a geochemical perspective, yttrium is considered as a HREE[1] and as such it is very common to use yttrium as a representative of the whole group of HREEs because of their similar chemical properties. Furthermore, comparable behavior of Y and the majority of the HREE in high-grade metasomatism processes [Ague, 2017] support this assumption. The hydration shell of Y^{3+} in aqueous solutions and possible complexation of Y^{3+} with chlorine has been subject to a number of studies at room temperature (e.g. Johansson and Wakita [1985], Petrović et al. [2016]). Molecular simulations in conjunction with advanced sampling methods indicate that in the absence of other ligands Y^{3+} is coordinated by eight nearest neighbor oxygen atoms and in Cl^- bearing as well in acidic solutions [Ikeda et al., 2005a,b], which to a large extent are hydration water molecules or at high pH OH^- groups [Liu et al., 2012]. The reported Y oxygen distance of 2.38 Å [Ikeda et al., 2005b] agrees with EXAFS and XANES measurements [Näslund et al., 2000, Lindqvist-Reis et al., 2000].

The complexation of Y^{3+} with Cl^- was studied by Vala Ragnarsdottir et al. [1998] at hydrothermal conditions up to 250 °C using *in-situ* EXAFS spectroscopy. The authors claim that yttrium is coordinated by 8-9 neighbors at hydrothermal conditions and does not associate

[1] International Union of Pure and Applied Chemistry: Nomenclature of Inorganic Recommendations 2005

with chloride but rather forms polyatomic yttrium species. In another study by Mayanovic et al. [2002], a strong association of Y with chloride up to YCl_4^- at 500 °C and a linear reduction of the total number of coordinating atoms from eight to four towards high temperatures are reported. The results of that study indicate that yttrium behaves like 3d transition metal ions rather than a HREE under hydrothermal conditions at high chloride activity. Solubility experiments up to 1 GPa and 800 °C in a hydrothermal piston-cylinder apparatus performed by Tropper et al. [2011, 2013] indicate that yttrium is transported as $[YClOH_2]_{aq}$ complexes in NaCl brines and that YF_2^+ is the major complex in a fluorine-rich environment.

While the stability and distribution of Y-(Cl,F) species in aqueous solutions at ambient conditions has been subject to a number of studies (e.g. Luo and Byrne [2001, 2000, 2007], Finney et al. [2019]) the knowledge of thermodynamic properties of yttrium species in hydrothermal fluids is limited to theoretical predictions [Haas et al., 1995, Wood, 1990] and one experimental study by Loges et al. [2013]. Stability constants of Y-(F,Cl) complexes at sub-crustal high P/T conditions have been barely investigated.

Aim of this Case Study

For a better understanding of the mobility of Y (as a representative of the HREE group) in subduction zone fluids at high P/T conditions, knowledge of the relation between the concentration of the molecular species in aqueous fluids and their thermodynamic properties are required. Yttrium in general is one of the most immobile REE [Ague, 2017, Schmidt et al., 2007b] in high grade metasomatism environments. But the high mobility in certain locations not only associated with hydrothermal ore deposits [McPhie et al., 2011, Graupner et al., 1999] but also in metamorphic or diagenesis context [Hole et al., 1992, Moore et al., 2013, Harlov et al., 2006] indicates that the dissolution or transport of Y is constrained to a very narrow fluid composition. Therefore, yttrium could be a potential indicator for the geological fluid composition.

It has to be underlined that uncertainty in the dielectric constant strongly impact the computed dissocation constants in electrolyte and nonelectrolyte solutions [Chialvo and Cummings, 1999] but *ab-initio MD* is able to reproduce the dielectric constant of water very precisely up to extreme conditions [Laasonen et al., 1993, Pan et al., 2013]. Therefore, *ab-initio* molecular dynamics simulations are used in this case study to investigate the molecular-scale structure and probe the

free energy of different Y-Cl-F complexes in the P/T range of a subducted slab.

3.1 Computation and Thermodynamic Approach

To separate the electronic and nuclear motion of the Car-Parrinello molecular dynamics a fictive electron mass of 600 a.u. with fictitious kinetic energy of 0.24 a.u. was used. All results presented here are based on simulations performed with a constant number of atoms, at constant volume and a temperature of 800 °C and with a time step of 0.1 fs.

For this case study two different pressure conditions of 1.3 GPa and 4.5 GPa were chosen. The volumes of the simulation cell were estimated from the correlation function provided by Mantegazzi et al. [2013] assuming a 2 molal NaCl solution for all cells (see Tab. 3.1). Due to this approximation the given pressures in Tab. 3.1 have to be considered as estimates.

The initial atomic configurations were derived from AIMD simulations of pure NaCl solutions (200 H_2O and 10 NaCl). This configuration had been equilibrated for a few tens of picoseconds (ps) at 1000 K and a simulation box size of 13.74 Å,. The original NaCl solutions were generated in classical molecular dynamics simulations using MCY potentials [Matsuoka et al., 1976]. By substitution of one of the sodium atoms by yttrium and decreasing the number of water molecules, chlorine as well sodium ions stepwise the configuration A1 in Tab. 3.1 was reached. Fig. 3.1 shows a snapshot of the simulation cell A1 with a $[YCl_3(H_2O)_4]_{aq}$ complex. The chloride ion not initially bonded to the yttrium ion are constraint to remain at larger distance (6-7Å) from the yttrium atom. All other simulation boxes (see Tab. 3.1) were generated from this initial one and equilibrated for several picoseconds.

For the fluoride-bearing cells different cell compositions due to the strong association of hydrogen and fluoride at low pressures were used. Only initially bonded F^- ions were included to avoid the formation of hydrofluoric acid by the reaction $H_2O + F^- \rightleftharpoons OH^- + HF$.

To look into the formation of mixed Y chloride fluoride species in equilibrium reactions one of the ligands is removed from Y^{3+} cation in multiple integration steps by constraining the Y-(Cl/F) distance. Fig. 3.2 illustrates an example of the dissociation reaction in the simulation box at 1.3 GPa and 800 °C:

$$[YCl_3(H_2O)_4]_{aq} + H_2O \rightarrow [YCl_2(H_2O)_5]^+ + Cl^-$$

During the integration the Y-Cl/F distance of the Cl^- or F^- that are not initially bonded to the

Table 3.1: Number of atoms in the different simulation cells together with the size of the simulation cells. The A and B refer to the system density $^{\top}$ of 1072 kg/m^3 (≡1.3 GPa) and 1447 kg/m^3 (≡4.5 GPa).

Cell	H_2O	Y^{3+}	Cl^-	F^-	Na^+	No. Atoms	$a^{\dagger}$
A1	84	1	6	0	3	262	14.29
A2	84	1	5	1	3	262	14.25
A3	84	1	4	2	3	262	14.21
A4	84	1	3	3	3	262	14.16
B1	84	1	6	0	3	262	12.93
B2	84	1	3	3	3	262	12.82

$\top$ volume estimated using the empirical equation of state from Mantegazzi et al. [2013] for 2 molal NaCl solution, † edge length (in Å) of the simulation cell

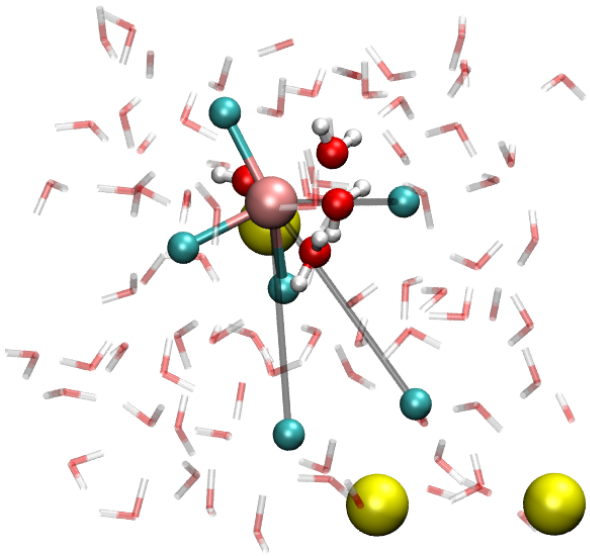

Figure 3.1: Snapshot of the simulation cell A1 with a $[YCl_3(H_2O)_4]_{aq}$ complex. The water molecules are indicated by red-white bond sticks, sodium yellow balls and chlorine in cyan. The H_2O in first hydration shell of yttrium (copper colored) are presented as balls. The constraints between the yttrium ion and the constraint Cl^- are colored in gray

yttrium ion is fixed at 7.0 Å to avoid disruptions during the integration.

The integration starts at the first distance (Fig. 3.2 (A)), which corresponds approximately to the equilibrium distance of the Y-Cl contact ion pair. This interatomic distance (A) is estimated as the intercept with the zero force line from a linear interpolation between the first and the second integration step starting from ~2.6 Å for Y chloride or 2.0 Å Y fluoride. With increasing displacement of the chloride ion, the constraint force is attractive (Fig. 3.2 (B)) until a water

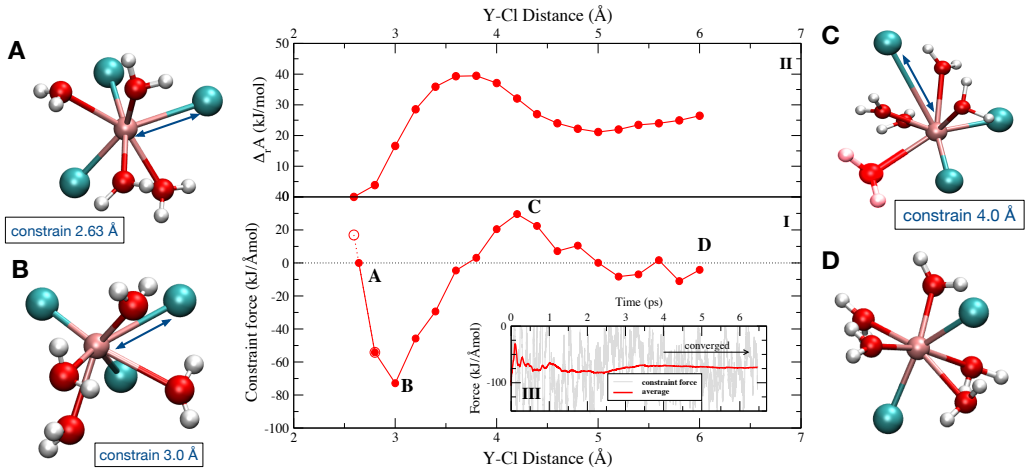

Figure 3.2: (I) potential of mean force of the dissociation reaction of YCl_3 to YCl_2^+ at 1.3 GPa and 800 °C over a distance between 2.63 Å and 6.0 Å. The evolution of the Helmholtz free energy is shown in (II). (A-D) indicate the different stages of the dissociation of the initial complex (see text for details). (III) shows exemplary the progress of the constraint force with simulation time for stage B for a Y-Cl distance of 3.0 Å.

---

molecule takes the place of the ion in the first coordination shell around the Y^{3+} (Fig. 3.2 (C)). At this point the force becomes repulsive. By integration over the potential of mean force (PMF) (Fig. 3.2 (I)) the Helmholtz free energy ($\Delta_r A$) difference between the initial complex and the product of the reaction is derived (Fig. 3.2 (II)). For the Y chloride complexes, a ligand in a distance of 6.0 Å is assumed to be dissolved and for Y fluoride this distance reduces to 5.0 Å. To estimated the convergency of the constraint force the standard deviation of the average force is computed. As criteria of convergency a value 5 kJ/mol over the last 2 ps is taken. This value is also considered as the approximate error of the computed reaction energies. To satisfy this criterion the constraint AIMD simulations are performed over 4.5-40 ps.

The standard Gibbs free energy ($\Delta_r G°$) depends on the reaction Gibbs free energy ($\Delta_r G$) derived from the MD simulation according to equation 2.12. The concentration of the solutes in the simulation volume (see Tab. 3.1) is quite different from this standard state. Therefore, the activity coefficient of every solute using the B-dot model was computed. The ϵ is calculated using the equation provided by Pan et al. [2013], Sverjensky et al. [2014] for pure H_2O assuming a fluid density of the simulation. The value of $\dot{B}$ is calculated by the CHNOSZ software package [Dick, 2008] applying the extrapolation suggested by Manning et al. [2013]. The $å$ parameter for the different complexes and ions (for all Y-Cl/F complexes a constant value of 4.5 Å is applied)

are taken from Kielland [1937a] and Eq. 2.5 was solved iterative in a Python implementation of the EQBRM program [Anderson and Crerar, 1993] (see Appendix).

Note that in the simulations a dissociation reaction is performed but to be in line with the modern nomenclature of aqueous geochemistry all the derived thermodynamic data presented below correspond to the formation reaction. In this study, two kinds of reactions are investigated:

$$Y^{3+} + nCl^{-} \rightarrow YCl_n^{3-n} \qquad n=1–3 \tag{3.1}$$

$$Y^{3+} + nF^{-} \rightarrow YF_n^{3-n} \qquad n=1–3 \tag{3.2}$$

In the following all results referring to one of those reaction are indexed by TI-n. Furthermore, for reasons of clarity the number of hydration water molecules in the formula of the aqueous complexes in some of the presented figures and tables are not included.

To distinguish pure OH^- from two H_2O sharing one hydrogen (transition state) the cutoff between the oxygen and the hydrogen is set to 1.3 Å. Additionally, the distance of the hydrogen within this cutoff distance to the next oxygen is taken as distinguishing criterion. Only if the oxygen of the next water molecule is located in a distance of >1.6 Å the OH^- is accounted as hydroxide. This value represent approximately the hydrogen bond distance between OH^- and H_2O [Stefanski et al., 2018]. To evaluate the formation of a certain species during a simulation run only complexes with a constant coordination of chloride and fluoride over at least 3 ps are considered. The average halogen ion hydration number is computed by counting the number of hydrogen oriented towards the ion of the vicinal water molecules.

3.2 Results

Yttrium Coordination in High Density Aqueous Fluid

AIMD simulations were performed for the hydrated Y^{3+} and for eleven different yttrium-halogen complexes: five Y-chloride (YCl_n^{3-n}, $n = 1-5$), three Y fluoride (YF_n^{3-n}, $n = 1, 2, 3$) and three mixed chloride fluoride complexes. Simulation conditions and obtained structural data are compiled in Tab. 3.2. Moreover, the formed aqueous species are listed in Tab. 3.3. Note

that the composition of the simulation cells varies slightly as cells A1-A4, B1 and B2 contain different amounts of fluoride and chloride .

Table 3.2: The listed atomic distances and coordination numbers are averaged over the whole AIMD time for all unbiased runs. Furthermore, the lifetime of the initial configuration regarding the chloride and fluoride coordination.

	Simulation parameters			Distances (Å)				Coordination numbers					
Run ID	Density (kg/m^3)	Time (ps)	Cell	Y-O	Y-O (2nd)	Y-Cl	Y-F	Y-O	Y-OH$^-$	Y-Cl	Y-F	∅ Y	Lifetime (ps)
#1	1072	25	A1	2.35	4.7	2.58	-	5.9	0.6	1.0	-	6.9	25
#2	1072	23	A1	2.36	4.8	2.59	-	4.8	0.3	2.0	-	6.8	23
#3	1072	24	A1	2.37	5.0	2.60	-	3.6	0.0	3.0	-	6.6	24
#4	1072	26	A1	2.35	5.1	2.58	-	2.9	0.0	3.4	-	6.3	14
#5	1072	26	A1	2.41	5.2	2.63	-	1.2	0.0	4.8	-	6.0	22
#6	1072	25	A2	2.37	4.5	-	2.08	5.6	1.0	-	1.0	6.6	25
#7	1072	29	A3	2.39	4.4	-	2.08	4.8	0.0	-	2.0	6.8	29
#8	1072	29	A4	2.43	4.5	-	2.11	3.5	0.0	-	3.0	6.5	29
#9	1072	29	A2	2.39	4.4	2.63	2.08	4.8	0.1	1.0	1.0	6.7	29
#10	1072	29	A2	2.39	4.5	2.62	2.10	3.9	0.1	1.6	1.0	6.5	17
#11	1072	27	A3	2.40	4.5	2.62	2.07	4.3	0.0	0.4	2.0	6.8	12
#12	1072	29	A1	2.35	4.6	-	-	7.2	0.5	-	-	7.2	29
#13	1447	27	B1	2.36	4.5	2.64	-	7.4	0.4	0.5	-	7.8	13
#14	1447	27	B1	2.34	4.5	2.65	-	5.9	0.1	2.0	-	7.9	27
#15	1447	27	B1	2.36	4.4	2.61	-	7.4	0.4	0.5	-	7.9	0
#16	1447	24	B2	2.34	4.5	-	2.06	6.7	0.2	-	1.0	7.7	24
#17	1447	27	B2	2.38	4.6	-	2.08	5.5	0.2	-	2.0	7.5	27
#18	1447	25	B2	2.39	4.3	-	2.15	5.6	0.1	-	2.6	8.1	14
#19	1447	25	B2	2.36	4.5	2.70	2.10	6.5	0.1	0.4	1.0	8.0	10
#20	1447	25	B2	2.36	4.4	2.71	2.11	5.9	0.1	0.8	1.0	7.6	3
#21	1447	27	B2	2.34	4.5	2.78	2.13	5.2	0.0	0.4	2.0	7.6	9
#22	1447	27	B1	2.36	4.4	-	-	7.8	0.8	-	-	7.8	27

Table 3.3: List of the simulation runs with their initial coordination complexes and complexes observed for at least 3 ps during the simulation. For runs where multiple complexes appear the observed complexes are listed in order of decreasing abundance.

	Simulation parameter			Complexes	
Run ID	Density (kg/m^3)	Time (ps)	Cell	Initial	Formed
#1	1072	25	A1	$[YCl(H_2O)_5]^{2+}$	$[YClOH(H_2O)_5]^{+}$, $[YCl(H_2O)_6]^{2+}$
#2	1072	23	A1	$[YCl_2(H_2O)_4]^{+}$	$[YCl_2(H_2O)_5]^{+} \cdot Na^{+}$, $[YCl_2(H_2O)_5]^{+}$, $[YCl_2OH(H_2O)_4]_{aq}$
#3	1072	24	A1	$[YCl_3(H_2O)_3]_{aq}$	$[YCl_3(H_2O)_4]_{aq}$, $[YCl_3(H_2O)_4]_{aq} \cdot Na^{+}$
#4	1072	26	A1	$[YCl_4(H_2O)_2]^{-}$	$[YCl_4(H_2O)_2]^{-} \cdot Na^{+}$, $[YCl_4(H_2O)_2]^{-}$, $[YCl_3(H_2O)_3]_{aq} \cdot Na^{+}$, $[YCl(H_2O)_6]^{2+} \cdot Na^{+}$
#5	1072	26	A1	$[YCl_5(H_2O)]^{2-}$	$[YCl_5(H_2O)]^{2-} \cdot Na^{+}$, $[YCl_5(H_2O)]^{2-}$, $[YCl_4(H_2O)_2]^{-} \cdot Na^{+}$
#6	1072	25	A2	$[YF(OH)(H_2O)_5]^{+}$	$[YFOH(H_2O)_5]^{+}$
#7	1072	29	A3	$[YF_2(H_2O)_5]^{+}$,	$[YF_2(H_2O)_5]^{+}$
#8	1072	29	A4	$[YF_3(H_2O)_4]_{aq}$	$[YF_3(H_2O)_4]_{aq}$
#9	1072	29	A2	$[YClF(H_2O)_5]^{+}$	$[YClF(H_2O)_5]^{+}$,$[YClF(H_2O)_5]^{+} \cdot Na^{+}$
#10	1072	29	A2	$[YCl_2F(H_2O)_4]_{aq}$	$[YCl_2F(H_2O)_4]_{aq} \cdot Na^{+}$, $[YClF(H_2O)_5]^{+}$, $[YClFOH(H_2O)_4]_{aq} \cdot Na^{+}$
#11	1072	27	A3	$[YClF_2(H_2O)_4]_{aq}$	$[YF_2(H_2O)_5]^{+} \cdot Na^{+}$, $[YClF_2(H_2O)_4]_{aq}$, $[YClF_2(H_2O)_4]_{aq} \cdot Na^{+}$
#12	1072	29	A1	$[Y(H_2O)_7]^{3+}$	$[YOH(H_2O)_6]^{2+}$, $[Y(H_2O)_7]^{3+}$
#13	1447	27	B1	$[YCl(H_2O)_6]^{2+}$	$[YCl(H_2O)_7]^{2+}$, $[YOH(H_2O)_7]^{2+}$
#14	1447	27	B1	$[YCl_2(H_2O)_5]^{+}$	$[YCl_2(H_2O)_6]^{+}$, $[YCl_2(H_2O)_6]^{+} \cdot Na^{+}$
#15	1447	27	B1	$[YCl_3(H_2O)_4]_{aq}$	$[YCl(H_2O)_7]^{2+}$, $[YOH(H_2O)_7]^{2+}$, $[YCl_2(H_2O)_6]^{+}$
#16	1447	24	B2	$[YF(H_2O)_7]^{2+}$	$[YF(H_2O)_7]^{2+}$,$[YFOH(H_2O)_6]^{+}$
#17	1447	27	B2	$[YF_2(H_2O)_5]^{+}$	$[YF_2(H_2O)_6]^{+}$, $[YF_2OH(H_2O)_5]_{aq}$
#18	1447	25	B2	$[YF_3(H_2O)_4]_{aq}$	$[YF_3(H_2O)_5]_{aq} \cdot Na^{+}$, $[YF_2(H_2O)_6]^{+} \cdot Na^{+}$, $[YF_2OH(H_2O)_5]_{aq} \cdot Na^{+}$
#19	1447	25	B2	$[YClF(H_2O)_5]^{+}$	$[YF(H_2O)_7]^{2+}$, $[YClF(H_2O)_6]^{+} \cdot Na^{+}$,
#20	1447	25	B2	$[YCl_2F(H_2O)_5]_{aq}$	$[YFCl(H_2O)_6]^{+}$, $[YFCl(H_2O)_6]^{+} \cdot Na^{+}$, $[YFOH(H_2O)_6]^{+}$
#21	1447	27	B2	$[YClF_2(H_2O)_5]_{aq}$	$[YF_2(H_2O)_6]^{+} \cdot Na^{+}$, $[YClF_2(H_2O)_5]_{aq} \cdot Na^{+}$, $[YF_2(H_2O)_5]^{+}$
#22	1447	27	B1	$[Y(H_2O)_8]^{3+}$	$[Y(H_2O)_8]^{3+}$, $[YOH(H_2O)_7]^{2+}$

Different partial radial distribution functions for Y-(Cl^-,F^-,OH^- ,OH_2) are shown in Fig. 3.3. To facilitate the comparison of the first peaks the $g_{ij}(r)$ are scaled to equal maximum intensity. The observed sequence of atomic distances between the central metal ion and its ligands holds for all the complexes. The shortest distance is found between Y^{3+} and F^- followed by Y–OH^- and Y–OH_2. The largest distance is observed for Y-Cl pairs. Further, in g_{Y-O}(r) a second maximum is observed. It corresponds to the 2nd hydration shell, which is formed around all complexes at all studied P/T conditions. For all fluids compositions, association of $NaCl_n$ (n=1-3) and of Na^+ with the yttrium complex is observed.

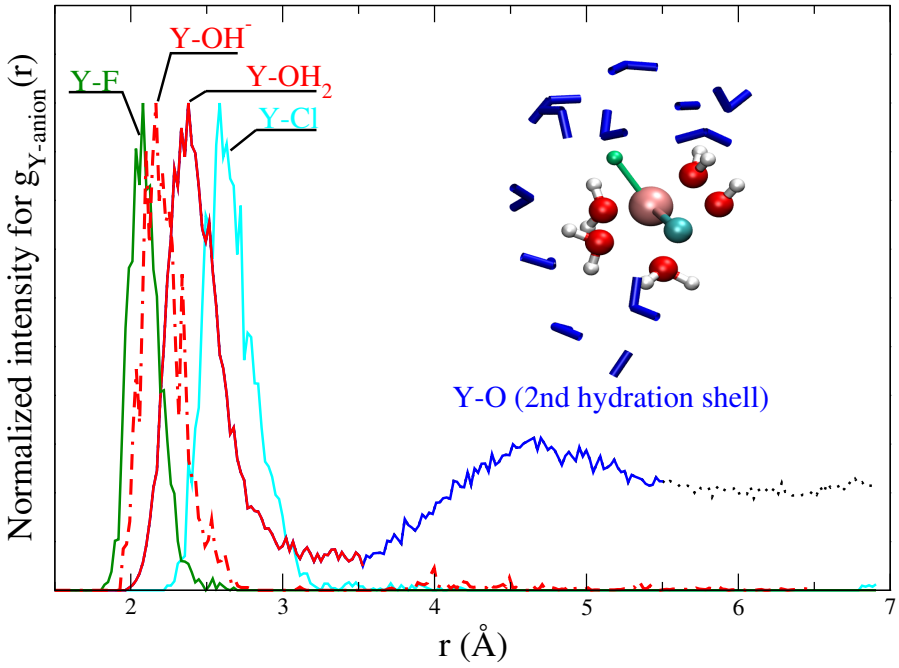

Figure 3.3: Radial distribution functions of Y-(Cl,O,F) scaled to the maximum of the $g_{ij}(r)$ from runs #9 and #12 together with a snapshot of a $[YClF(H_2O)_5]^+$ complex. In the snapshot (from a run at 1.3 GPa and 800°C) the central yttrium atom is surrounded by chlorine (cyan), fluorine (green) and hydroxyl groups and water molecules (red–O and white–H balls). Water molecules of the 2nd shell are shown as blue sticks. This visualization is meant to illustrate the relation between $g_{ij}(r)$ and the atomic structure of the aqueous species. The colors of the ligands in the snapshot are equivalent to those in the $g_{ij}(r)$ functions.

At 1.3 GPa, the average Y coordination by O, Cl and/or F is about seven (see Fig. 3.4) with two exceptions run #4 and #5, even if the initial coordination is lower as e.g. in runs #1 and #2. In runs #1-3, the initial Y chloride coordination is retained over the whole AIMD run time, whereas for #4 and #5 the fourfold and fivefold Cl-coordination do not persist and the

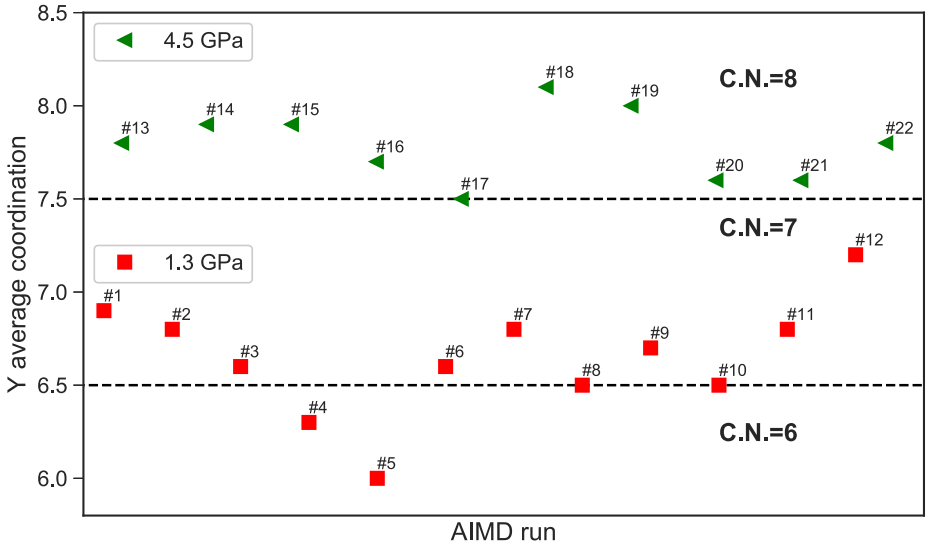

Figure 3.4: Average yttrium coordination by chloride, fluoride and oxygen for runs #1-22

time average yttrium coordination is below seven. Frequently, the formation of OH^- in first hydration shell of yttrium can be observed. The major hydroxide formation mechanism will be discussed below.

Fig. 3.5 provides an overview over appearance and disappearance of selected structural units in the course of the simulations, i.e. the stability of the initial complexes, Y hydroxide association and bonding of the coordinating halogen to sodium. All five chloride complexes associate with sodium. The strongest association is observed in #2,#3, #4 and #5 where the sodium is connected to one or two chloride ligands of the Y complex. This association increases with the number of halogen ions in this complexes. Furthermore, in #4 and #5 this association initiates the dissociation of $[YCl_4(H_2O)_2]^-$ and $[YCl_5(H_2O)]^{2-}$. Even larger clusters of sodium, constraint chlorides and the Y chloride complex appear over time scales of less than 3 ps. Moreover, from #1 to #5 the average Y coordination decreases constantly with initially bonded chlorides (Fig. 3.4). The Y-O distances do not change significantly with an increasing number of chloride ligands from #1 to #4. Only in run #5 a significantly higher Y-O distance of 2.41Å occurs. In #1, the highest amount of hydroxide is formed and $[YClOH(H_2O)_5]^+$ is the major species. The Y chloride distances range from 2.58 Å in #1 to 2.63 Å in #5.

For pure Y fluoride complexes at the same conditions (#6-8) a slight increase of the Y-O distance with increasing number of fluoride ligands from 2.37 Å in $[YF(H_2O)_6]^{2+}$ to 2.43 Å

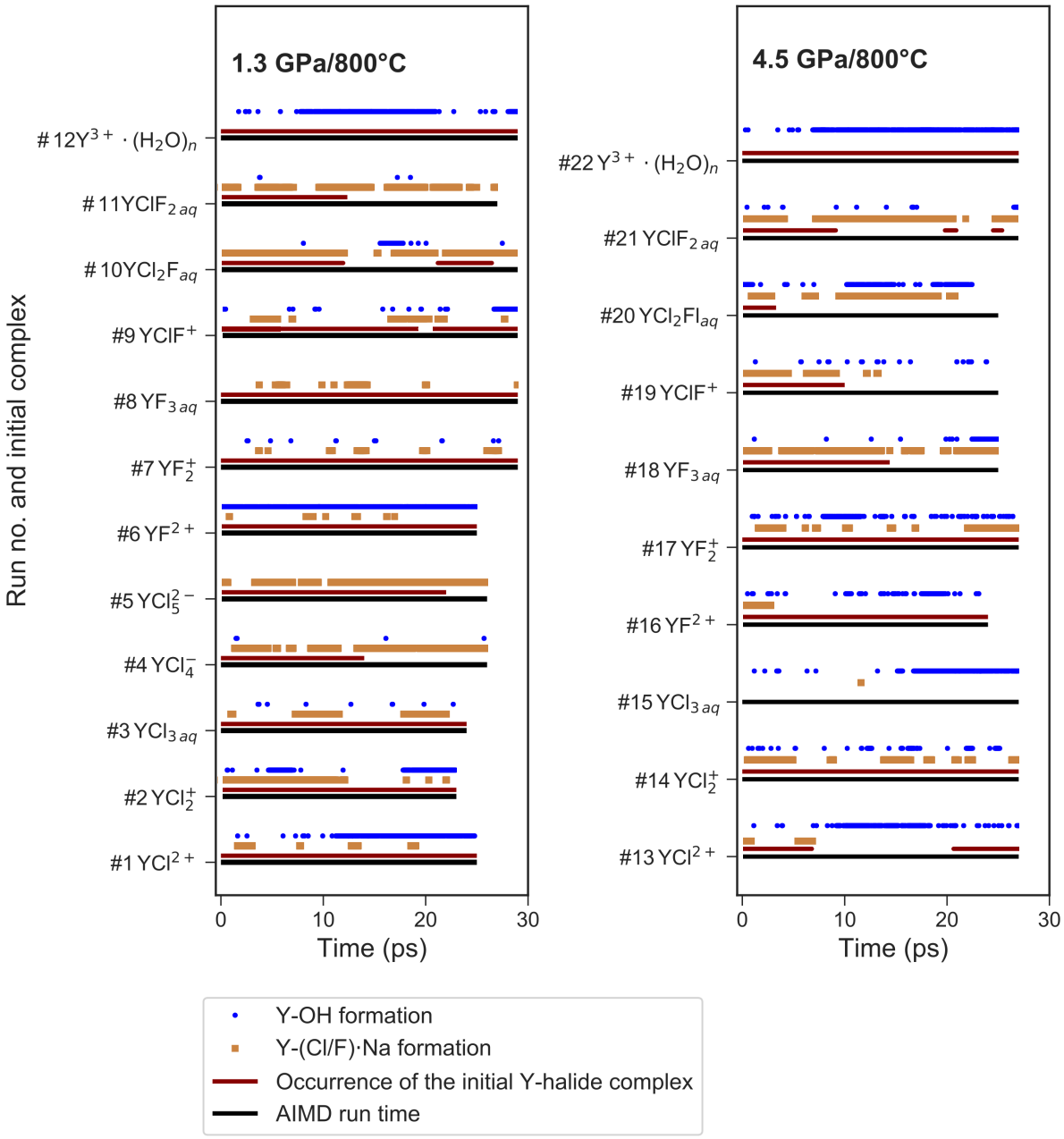

Figure 3.5: Appearance of selected ion pairs or complexes during the different AIMD simulations. This includes the formation of OH^- within the first hydration shell of yttrium, the association of sodium with the coordinating halogens and the stability of the initial complexes over AIMD time in respect to the yttrium-halide association.

---

in $[YF_3(H_2O)_4]_{aq}$ is observed. In all three runs the initial complex persists over the whole simulation time. As in case of Y chloride, an association of fluoride with sodium is observed but less pronounced. In #6, where only one fluoride is initially bonded to the central ion, OH^- is formed within the first hydration shell of yttrium. The Y-F distances of the complexes are

approximately 0.5 Å shorter than those of Y chlorides.

For the Y fluoride chloride mixed complexes (runs #9-11) only the run starting initially from $[YClF(H_2O)_5]^+$ does not show the formation of multiple complexes over time. Here, only short separations of the Cl^- over ~1 ps from the complex occur. In #10 $[YCl_2F(H_2O)_4]_{aq}$ dissociates to $[YClF(H_2O)_6]^+$ after 11.5 ps. This complex is present over approximate 10 ps in conjunction with the formation of $[YClFOH(H_2O)_4]_{aq}$ followed by the re-association of the initial complex. In #11 starting from $[YClF_2(H_2O)_4]_{aq}$ the initially bonded chloride is released after ~12 ps and $[YF_2(H_2O)_5]^+$ is formed. The Y-(F,Cl) distances of the mixed complexes are comparable to those of the pure ones.

In run #12 starting from $[Y(H_2O)_7]^{3+}$ hydroxide is formed within the first 8 ps (see Fig. 3.5), which results in the formation of $[YOH(H_2O)_6]^{2+}$ that is present over 14 ps of the AIMD time followed by a reassociation and dissociation of the hydroxide with the oxonium ion (H_3O^+).

In the high pressure runs at 4.5 GPa (#13-22) an average Y coordination of about eight can be found (see Fig. 3.4). In case of the Y chloride complexes, the dissociation of the onefold and threefold coordinated complexes is observed in runs #13 and #14 (see Fig 3.5). The higher coordinated Y-Cl complexes break apart within the equilibration run and the results are not further analyzed. This breakdown is partly driven by the association of the coordinating chloride with sodium. For instance, in run #13 one sodium chloride unit associates with the Y complex before the chloride dissociates from the Y and $[NaCl_3]^{2-}$ is formed (Fig. 3.6). The resulting $[Y(H_2O)_8]^{3+}$ associates with OH^- shortly there after. In all runs, the formation of OH^- by the self-dissociation of H_2O close to the yttrium ion can be seen as in the low P runs. Only in run #14 the initial Y chloride complex ($[YCl_2(H_2O)_5]^+$) persists over the whole 27 ps trajectory.

Fig. 3.6 illustrates the OH^- formation mechanism as it evolves for Y chloride and Y fluoride complexes at low and high pressure conditions for the example in run #13. After the initial complex dissociates within the first 7 ps into $[Y(H_2O)_8]^{3+}$ a proton is transferred between one H_2O in the first hydration shell and a water molecule of the second shell after additional 2-3 ps. The formed $[YOH(H_2O)_7]_{aq}$ is present over 14 ps followed by reassociation with chloride. The formed $[YClOH(H_2O)_6]_{aq}$ persist during the remaining simulation time with short interruptions due to the proton transfer between HO^- and H_3O.

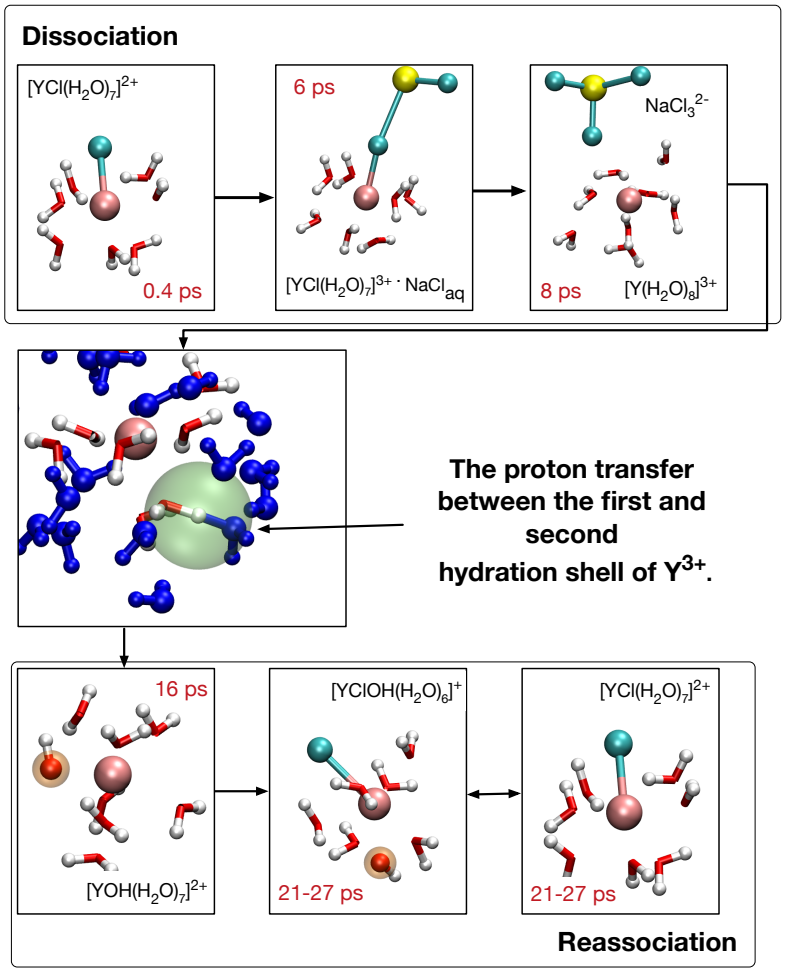

Figure 3.6: Formation of $[YOH(H_2O)_7]^{2+}$ and reassociation of initial complex $[YCl(H_2O)_7]^{2+}$ in run #13. The blue colored water molecules are located in the 2nd hydration shell, red-white H_2O and OH^- are bonded in the first coordination shell and sodium is colored yellow. Chloride ions are in cyan and the Y^{3+} ion is copper colored. The red numbers indicate the time progress in the AIMD simulation. In center the proton transfer state is highlighted with a green sphere.

For the Y fluoride complexes at the high pressure conditions the onefold and twofold coordination persists over the whole simulation run (#16,#17). All complexes show association with one or two sodium ions over several picoseconds but this interaction does no lead to a dissociation of a fluoride from Y. In #18, the initially threefold coordinated complex dissociates after 14.5 ps and $[YF_2(H_2O)_6]^+$ is formed. None of the mixed Y-Cl-F complexes at 4.5 GPa is stable on the entire simulation run. In all runs chloride ions are dissociated from the yttrium after at most ~10 ps and pure Y fluoride or Y fluoride hydroxide complexes remain. As in the low pressure run for the pure hydrated Y^{3+} a hydroxide ion is found in the first hydration shell

during a significant amount of simulation time.

Concerning changes of the atomic bonding distances (Y-(O,Cl,F) between both pressure condition those lie in the range of 0.01-0.03 Å for the stable complexes. A closer look at the distance between 2nd hydration shell and the central ion (see Tab.3.2) shows some changes between the P condition. For the Y chloride complexes a continuously increase of the Y-O(^{2nd}) is observed at low pressure conditions with increasing Y-Cl coordination. For YCl_2^+, YF^{2+} and Y^{3+} this distance decrease by 0.2-0.3 Å between both *P* conditions.

Comparing the average H_2O coordination of the halogens purely hydrated or bonded to the metal ion a change under low and high pressure conditions is observed. For chloride the number of hydrating water molecules increases from ~2 to ~4 between the YCl_2^+, $YCl_{3\,aq.}$ and $YClF^+$ in comparison to the free Cl^-, whereas for the mixed complexes $YClF_{2\,aq}$ the chloride hydration number increase to three. For YCl^{2+}, YCl_4^- and YCl_5^{2-} that number lies between two and three. While the fluoride is coordinated by one water molecule in the Y fluoride and mixed complexes. At 4.5 GPa F^- is hydrated by four H_2O and by two when associated with the metal ion, whereas the Cl^- coordination increase to five solvent molecules. Within the Y chloride complexes, existing at least over 10 ps of the AIMD run, it is coordinated by three water molecules.

To conclude this section, the main findings from the AIMD simulations are summarized. Firstly, the pure Y chloride complexes YCl^{2+}, YCl_2^+ and $YCl_{3\,aq}$ do not dissociate within the course of the simulation of at least 23 ps at a pressure of 1.3 GPa ($\equiv$ 1072 kg/m^3) but they do with increasing pressure (4.5 GPa $\equiv$ 1447 kg/m^3) except for YCl_2^+, sometimes accompanied by the formation of Na-Cl cluster. Furthermore, YCl_4^- and YCl_5^{2-} do not persist in the unbiased AIMD simulations. Secondly, the pure Y fluoride complexes are stable at 1.3 GPa. But it is important to state that the formation of hydrofluoric acid is very strong when the fluoride is not bonded to the metal ion at low P conditions. At 4.5 GPa the neutral complex $[YF_3(H_2O)_5]_{aq}$ dissociates and a lower coordinated species persists. Thirdly, OH^- is formed in the first hydration shell of Y chloride and Y fluoride complexes driven by the self-dissociation of water and its abundance increases with decreasing number halogen ligands. Furthermore, chloride as well fluoride form mixed complexes with yttrium and hydroxide at both P/T conditions, whereas Y fluoride chloride mixed complexes are rather unstable. The overall coordination of yttrium changes

from ~7 to ~8 in the investigated P/T range.

Free Energy Exploration

Although several complexes are observed in some of the runs described above, it is not feasible to derive the corresponding formation constants of the aqueous species directly from the AIMD simulations. This would require much longer simulation times to ensure the statistical significance of the relative species abundance. On the tens of picoseconds timescale, a complete exchange of the halogen ligands of the Y chloride or Y fluoride complexes is not observed except for runs #15 and #13. To overcome this problem the thermodynamic integration (TI) approach within a constraint AIMD simulation is applied to compute the reaction free energies of aqueous complex dissociation. As described in the previous section the mixed fluoride chloride complexes have a tendency to dissociate already during the conventional AIMD runs, which indicates their low stability. Therefore no TI runs are performed for those complexes. Furthermore, during the TI of YCl_4 and YCl_5, even when multiple Cl are removed, further Y-Cl dissociation appears in the remaining complex and no reaction free energy can be reported here. To ensure that the formation of OH^-, HCl and HF does not artificially evolve due to the change of the constraint Y-Cl distance between the integration steps we repeat several steps in all TI runs from different starting configurations. Thus, we confirm that all results are reproducible within a series of simulations. The derived Helmholtz free energies ($\Delta_r A$) of the reactions 3.1 and 3.2 are listed in Tab. 3.4.

Table 3.4: List of the formation Gibbs free energies (kJ/mol) derived from *ab initio* thermodynamic integration. The error of the free energies is estimated with 5 kJ/mol.

Nr	Reaction	Cell	Temperature (°C)	Pressure (GPa)	Y-(Cl,F) (Å)	$\Delta_r G$	$\Delta_r G^\circ$	log K
TI-1	$[YOH]^{2+} + Cl^- = [YClOH]^+$	A1	800	1.3	2.57	-36.1	-57.4	2.79
TI-2	$[YClOH]^+ + Cl^- + H_3O^+ = [YCl_2]^+ + 2H_2O$	A1	800	1.3	2.57	-38.8	-57.6	2.80
TI-3	$[YCl_2]^+ + Cl^- = [YCl_3]_{aq}$	A1	800	1.3	2.64	-26.4	-41.8	2.03
TI-4	$[YOH]^{2+} + Cl^- = [YClOH]^+$	B1	800	4.5	2.62	-29.6	-57.4	2.79
TI-5	$[YClOH]^+ + Cl^- + H_3O^+ = [YCl_2]^+ + 2H_2O$	B1	800	4.5	2.64	-8.5	-34.4	1.68
TI-6	$[YOH]^{2+} + F^- + H_3O = [YFOH]^+ + HF_{aq} + H_2O$	B5	800	4.5	2.12	-45.9	-85.6	4.17
TI-7	$[YF]^{2+} + F^- = [YF_2]^+$	B5	800	4.5	2.13	-38.5	-74.7	3.64
TI-8	$[YF_2]^+ + F^- = [YF_3]_{aq}$	B5	800	4.5	2.14	-36.3	-72.5	3.53

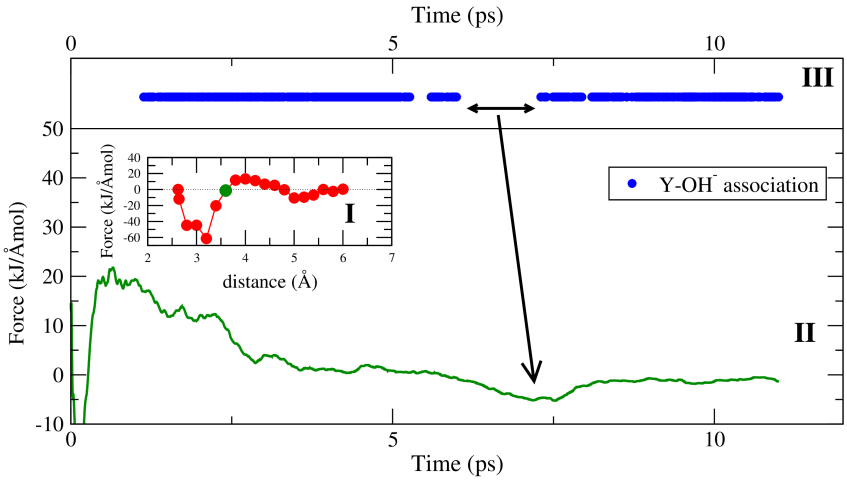

Figure 3.7: (I) Potential of mean force of TI-4. The green circle indicates the constraint distance of 3.6 Å for which the cumulative mean force is shown in (II). Dots in (III) indicate the presence of Y-OH$^-$ bonds during the simulation run.

At 1.3 GPa, in TI-1 starting from $[YCl(H_2O)_6]^{2+}$ in nearly all TI steps close to the yttrium OH^- formed by the hydrolysis of water molecules within the first 2-4 ps. Therefore, the constraint dynamics that leads to a dissociation energy of 36.1 kJ/mol does not distinguish between $[YCl(H_2O)_6]^{2+}$ and $[YOHCl(H_2O)_5]^{+}$ complexes. For TI-2, a similar dissociation energy of 38.8 kJ/mol is observed but much less hydroxide ions are formed such that in average over all integration steps Y-OH^- appears in only 14 % of the total simulation time. The lowest dissociation energy of the Y chloride complexes at 1.3 GPa occurs in TI-3 with 26.4 kJ/mol. In TI-3 only little amounts of OH^- are formed. While the integration proceeds the yttrium-oxygen coordination changes (including OH^- and H_2O) for all complexes at a constraint Y-Cl distance between 3.6-4.0 Å. The removed chloride associates with sodium throughout the dissociation process over few picoseconds as well the remaining Y chloride complex. From the evolution of the constraint force $F(r)$ between Y and Cl the impact of the Cl-Na bonding on the species stability cannot be derived. To apply the same constraints to the Y fluoride complexes was not possible at 1.3 GPa due to strong association of H^+ and F^-. The formation of hydrofluoric acid prevents the required long constraint Y fluoride bond distances for the integration of the PMF.

For the 4.5 GPa runs, the dissociation energies of the Y chloride complexes significantly decrease. As in the lower pressure runs, the integration does not distinguish between complexes in which OH^- is present or absent. In TI-4, starting from $[YClOH(H_2O)_6]^{+}$ and forming $[YOH(H_2O)_7]^{2+}$ a free energy difference of 29.6 kJ/mol is obtained. As illustrated in Fig. 3.7

the reassociation of OH^- with an excess proton leads to a higher constraint force due to the decreasing attraction of the metal cation to the constraint chloride ligand. The most frequent Y-OH^- association is observed at constraint Y-Cl distances between about 3.0 and 4.5 Å, which is largely in the repulsive regime of the PMF (Fig. 3.7I).

TI-5 yields the lowest dissociation energy of 8.5 kJ/mol where in several of the integration steps the second chloride ligand also dissociates and $[YOH(H_2O)_7]^{2+}$ is formed. The Y-Cl dissociation is preceded by an Y-OH^- association and results in the formation of $[YOH_{0-1}(H_2O)_{6-7}]^{3-2+}$. In those cases, the initial complex was reset and the integration step was restarted. For $[YCl_3(H_2O)_5]_{aq}$ it was not possible to derive a dissociation energy because the initial complex dissociated at short Y-Cl constraint distances within the first picosecond of each simulation.

In TI-6 to TI-8 the dissociation energies of Y fluoride complexes following the reaction 3.2 are investigated. The equilibrium distance between the yttrium ion and its fluoride ligands is smaller than the Y chloride bond distance. Due to this shorter distance the integration range to reach the dissociated state can be reduced to 5.0 Å. In each run of this simulation series the formation of hydrofluoric acid by the protolysis of an H_2O or the proton transfer of H_3O^+ to the removing F^- at a constraint distance of ~2.6 Å was observed. In TI-7 and TI-8 smaller amounts of HF units are formed compared to TI-6 and the proceeding of the TI is less affected. However, dissociation energies (Fig. 3.8) are quite similar between the Y fluoride complexes. During the integration, the Y complexes as well the removing fluoride ions interact with sodium. During the integration no self-dissociation of the complexes is observed except for $[YF_3(H_2O)_5]_{aq}$. In the latter case at a constant distance of 2.6 Å one of none constraint fluorides separates from the initial complex. However, this behavior is not reproducible.

During all integration runs at both pressures, the Y-O coordination number increases in average by one during the transformation from the associated to the dissociated state. For the Y chloride complexes the increase in hydration happens at a Y-Cl distance between 3.6-4.1 Å, which is assigned to the repulsive part of the PMF. For the dissociation of Y fluoride complexes this distance decreases to 3.4-3.6 Å. A significant influence of the 2nd hydration shell on the constraint force of the reaction coordinate can not be found. All complexes and the removing halogen interact with sodium. This interaction cannot be quantified by the PMF. But the

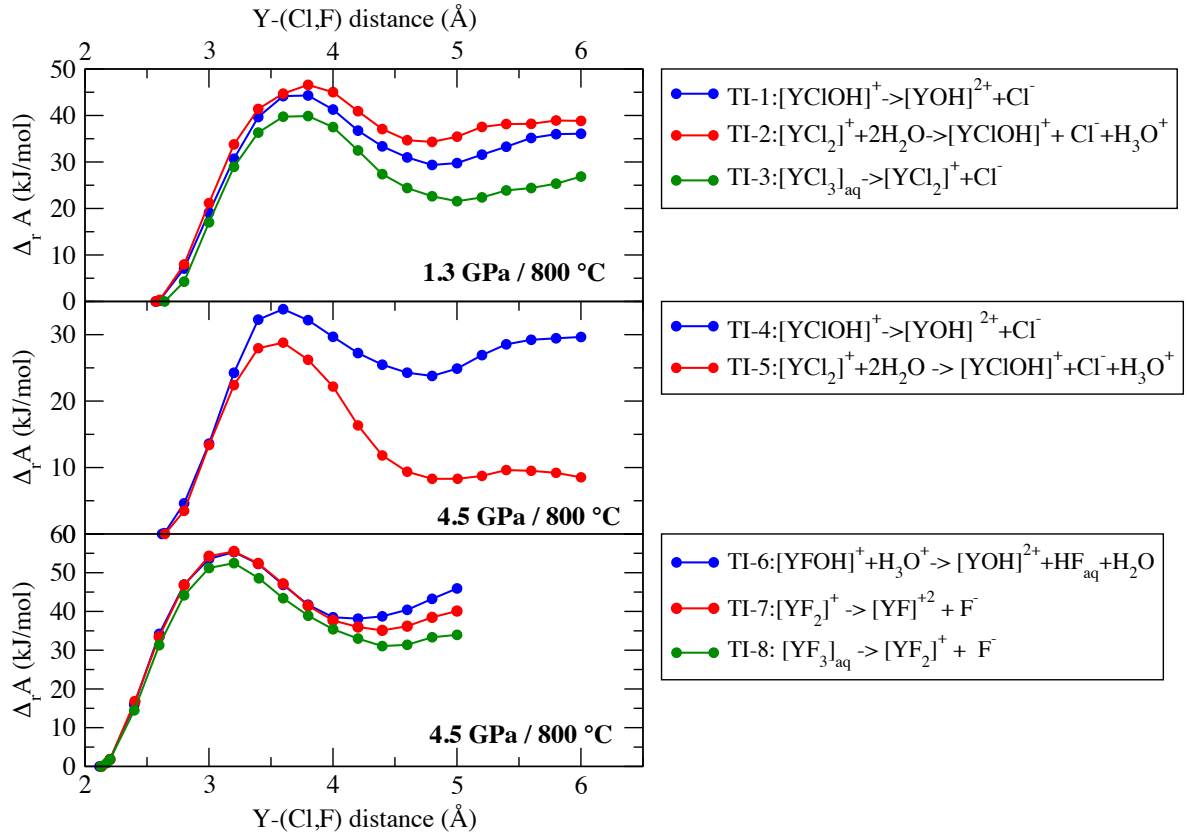

Figure 3.8: Evolution of the Helmholtz free energy derived from thermodynamic integration for Y-Cl/F complexes at 800°C and 1.3/4.5 GPa.

association of the yttrium complex with sodium decreases with the number of halogen ligands.

Thermodynamic Data

Finally, the reaction free energies derived from thermodynamic integration are transformed into standard state properties by applying the activity corrections described in the methods section above. The standard state correction yields $\Delta_r G^\circ$ that are significantly smaller compared to $\Delta_r G$ (see Tab. 3.4). This treatment does not consider explicitly the formation of HCl and HF as well the association of yttrium with hydroxide because their formation during TI is not systematic and it is not possible to quantify their contributions to the reaction free energies. As these contributions seem not to be negligible as shown in Fig. 3.7 the logarithmic stability constants include not only the reactions listed in Tab. 3.5 and are therefore indicated with a star ($\log \beta^*$). Fig.3.9 shows the $\Delta_r G^\circ$ and $\log \beta^*$ for the different species. While pressure

does not affect the formation reaction of YCl^{2+}, the stability of YCl_2^+ decreases substantially with increasing pressure. This finding is in sharp contrast to the observations in unconstrained AIMD simulation in run #13 and #14. Comparing the stability constants of chloride and fluoride species at 4.5 GPa, the fluoride species are more stable by 1.4 ($\log \beta_1^{\circ *}$) to 3.3 ($\log \beta_2^{\circ *}$) log units.

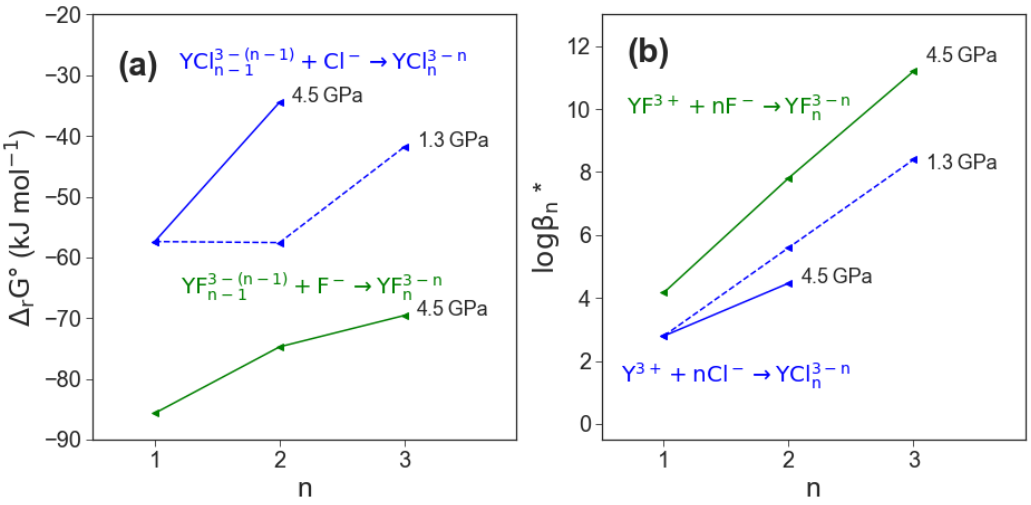

Figure 3.9: (a) reaction Gibbs free energy $\Delta_r G°$ of the different formation reactions, (b) change of the logarithmic stability $\log \beta^*$ (for the meaning of * see text) constant of the different Y-(F,Cl) complexes.

Table 3.5: List of the logarithmic stability constants $\log \beta^*$ derived from *ab initio* thermodynamic integration in comparison to theoretical prediction based on HKF regression.

Density (kg/m^3)	P (GPa)$^\top$	Reaction	$\log \beta^*$	$\log \beta^\dagger$
1072	1.3	$Y^{3+} + Cl^- = YCl^{2+}$	2.8	3.4^M
1072	1.3	$Y^{3+} + 2Cl^- = YCl_2^+$	5.6	4.6^M
1072	1.3	$Y^{3+} + 3Cl^- = YCl_{3\,aq}$	8.4	-
1447	4.5	$Y^{3+} + Cl^- = YCl^{2+}$	2.8	-1.7^M
1447	4.5	$Y^{3+} + 2Cl^- = YCl_2^+$	4.5	0.04^M
1447	4.5	$Y^{3+} + F^- = YF^{2+}$	4.2	3.4^L
1447	4.5	$Y^{3+} + 2F^- = YF_2^+$	7.8	10.9^L
1447	4.5	$Y^{3+} + 3F^- = YF_{3\,aq}$	11.2	-

* indicate that listed values involves further transitions states that not represent by the chemical equation. $^\top$ pressures estimates assuming a 2 molal NaCl solution using empirical equation of state by [Mantegazzi et al., 2013]. † Values computed from HKF parameter using the DEW model [Sverjensky et al., 2014] reported from Loges et al. [2013]^L and Migdisov et al. [2009]^M for holmium (Ho) complexes.

3.3 Discussion

Molecular Structure of the Aqueous Complexes

As mentioned in the introduction the number of studies focusing on the hydration environment of yttrium or other HREE in aqueous fluids at high T and P conditions is very limited. The average coordination of seven nearest neighbors that is observed in the simulations at 1.3 GPa fits in the range of experimental results. Vala Ragnarsdottir et al. [1998] observed 8-9 nearest neighbors at lower T of 250 °C and vapour pressures in highly concentrated chloride solution. But they did not notice an association of Y chloride, whereas Mayanovic et al. [2002] do observe strong association with an average coordination of four at 500 °C. YCl_4^- is not stable in the presented simulation at both pressure conditions. The reason for this could be the lower average Y coordination in this complex as well as in YCl_5^{2-}. Here, the average coordination of seven as present in all the stable Y chloride complexes can not be achieved due to the arrangement of the chlorides around the central ion. While the Y oxygen distance derived from EXAFS spectra by Vala Ragnarsdottir et al. [1998] (the conference abstract by Mayanovic et al. [2002] do not comprise quantitative data) in the range of 2.36-2.39 Å are in good agreement with the atomic distances from the presented simulations. Nevertheless, the simulations are carried out at higher T (800 °C) than the experiments by Vala Ragnarsdottir et al. [1998] or Mayanovic et al. [2002] and are only partially comparable.

The formation of stable Y chloride complexes at both pressure conditions confirmed observations by e.g. Tropper et al. [2011] and Schmidt et al. [2007b] that the mobility of yttrium increases with increasing availability of Cl^- in aqueous systems. These Y chloride complexes become less stable with increasing P. The destabilization of metal-halide species with rising pressure is known from a variety of systems (see overview by [Manning, 2018]). It is commonly explained by the increase of the dielectric constant with increasing density at constant T. The change of ϵ ($\epsilon_{1072\,kg/m^3}$=17.1,ϵ_{1447kg/m^3}=26.2) according to Sverjensky et al. [2014]) leads to a stronger hydration of the metal ion by H_2O and charged species are more favored. Therefore, $YCl_{3\,aq.}$ is not stable at 4.5 GPa (≡ 1447 kg/m^3). The direct competition of both ligands in the mixed complexes shows a clear preference of yttrium to form stable bonds with F^- rather than with Cl^-. Moreover, the lower reaction Gibbs free energies of the Y fluoride species in Fig. 3.9a strongly support this observation.

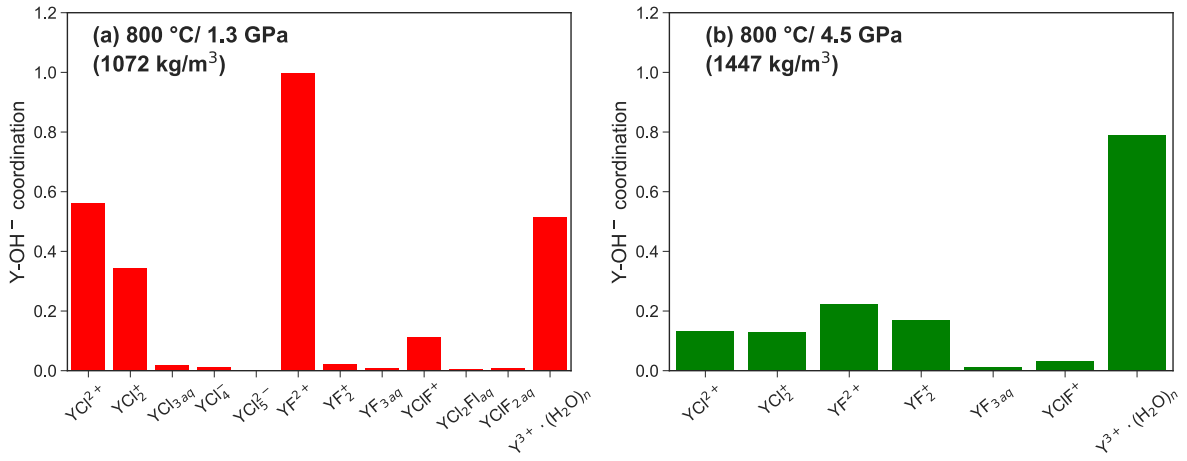

Figure 3.10: (a,b) Comparison of the average Y-OH$^-$ coordination number between the different complexes that exist at least over 10 ps in the unconstrained AIMD.

Fig. 3.10 a,b compares the Y-OH$^-$ formation between both pressure conditions in those aqueous complexes that are stable over at least 10 ps in the unconstrained simulations. A higher abundance of hydroxide groups at lower P for Y-(Cl/F) complexes is observed. Furthermore, the amount of formed OH$^-$ decreases with increasing number of ligands and is particularly higher for the purely hydrated Y^{3+} under both P conditions. Those dependencies cannot be explained by the increased self-dissociation of water, which increases with pressure (see e.g. Rozsa et al. [2018], Goncharov et al. [2005]), according to Marshall and Franck [1981] the OH$^-$ molality range in the order of 10^{-6} to 10^{-5} under the investigated P/T conditions. Therefore, the hydroxide formation is driven by the charge compensation in the absence of ligands around the yttrium. The low abundance of Y-OH$^-$ in the neutral species (e.g $YF_{3\,aq}$) emphasizes this interpretation. It has to be stressed out that the initial simulation cells do not contain excess hydroxide ions. Therefore, the Y-OH$^-$ association is expected to be much higher if the OH$^-$ concentration increases. But it has to be underlined that the values in Fig.3.10 are rather imprecise because no equilibrium distribution of Y hydroxide bonds can be reached in the rather short simulation time. Therefore, the slight increase of OH$^-$ within YF_2^+ and the purely hydrated yttrium ion, at 4.5 GPa, refers to the statistic error.

The association of yttrium with hydroxide as observed in the simulations was also noticed in high P/T solubility experiments by Tropper et al. [2011] in NaCl brines but not in the H_2O–NaF system [Tropper et al., 2013]. The authors explained the association by a geometrical effect.

The smaller HREE (in comparison to a LREE) have less attraction to a large chloride ion due to the so called "steric hindrance" as discussed by Mayanovic et al. [2009]. But in case of the Y fluoride complexes especially for YF^{2+} the OH^- formation is also controlled by the protolysis of H_2O close to the metal ion. Fluoride is much smaller than chloride but shows the same behavior. Therefore, the geometrical explanation does not hold to explain the Y hydroxide bonding. That this process was not detected in the experiments by Tropper et al. [2013] might be caused by the high NaF_s content in the experiments. The majority of YF_2^+ in the experiments underline this conclusion. That the formation of Y-(F/OH) species was not detected in solubility experiments by Loges et al. [2013] up to 250 °C indicates that the protolysis of vicinal water by yttrium is a process at very high temperature. Furthermore, the same observation was reported by van Sijl et al. [2010] for Ti^{4+} and might be a general property of high-field-strength elements.

That the association of yttrium with hydroxide directly drives the dissociation of Y chloride is inconclusive. But it appears that yttrium forms stable halide-hydroxide aqueous complexes. However, a competition of sodium and yttrium for chloride in brines seems to be a controlling factor for the Y chloride speciation.

An additional driving force for the ion association in aqueous fluids with increasing temperature has been discussed by Sherman [2010], Mei et al. [2014] based on AIMD simulations, that is not fully accounted in the main theory of high temperature aqueous geochemistry [Anderson, 2009, Sverjensky, 2019]. Namely, the entropy ($T\Delta S°$) drives the ion association due to changes in the local solvent structure near the critical point and above. Here primarily the translational entropy through hydration changes of the ions during the aqueous reaction. Such a concept was already discussed by Mesmer et al. [1988], that the change in the electrostriction volume of the solvent controls the association of aqueous species e.g. $NH_{3\,aq}$, HCl_{aq} and $NaCl_{aq}$. Furthermore, the authors propose that this effect decreases with increasing density at constant temperature ($\geq$ 200 °C). Regarding the presented case study a relation of the change of hydration of the different halogen ions and the stability of certain complexes is observed under lower pressure conditions. For example the formation of YCl_2^+ and $YCl_{3\,aq}$ releases of two inner-sphere waters molecules because the hydration of Cl^- decrease from 4 to 2. That might explain the slightly higher reaction Gibbs free energy of 38.8 kJ/mol in TI-2 in comparison to TI-1 (36.1 kJ/mol)

where only one H_2O is released, beside the effect of OH^- formation. The same applies to the unstable mixed complexes YCl_2F_{aq} and $YClF_{2\,aq}$. Due to the strong attraction between fluoride and hydrogen when it is freely hydrated by H_2O in the low P run the F^--H_2O coordination can not directly be derived from the presented simulations. Therefore, this value is derived from a simulation at 727 °C and a solution density of 1080 kg/m^3 in case study III in chapter 5 where the fluoride is surrounded by 4 H_2O in average. Therefore, a loss of three inner-sphere solvation H_2O for the yttrium and fluoride association is gained and this might be an additional stabilization of the Y-F bond formation. At high pressure of 4.5 GPa (≡ 1447 kg/m^3) the difference in H_2O exchange between F^- and Cl^- vanished during the aqueous reactions. These observations support the assumptions by Mesmer et al. [1988], Sherman [2010], Mei et al. [2015], that this entropic contribution decreases with increasing solvent density. But this rather qualitative evolution of hydration changes can not provide a general conclusion for the impact of translational (and configuration) entropy changes on ion association under high temperatures. Therefore, a direct sampling of the change of entropy and enthalpy of the solvent, during the aqueous species formation, is necessary. A comparable approach was used by Piaggi et al. [2017] to investigate the different contributions of these thermodynamic potentials to the crystallization of sodium and aluminum.

Comparison of the Thermodynamic Data with HKF Regression

In situ high *P* and high *T* thermodynamic properties of Y chloride and fluoride species are not available to compare and evaluate the present simulation results. Therefore, the Deep Earth Water (DEW) model [Sverjensky et al., 2014] is used to compute stability constants of YF^{2+} and YF_2^+ derived from solubility experiments up to 250 °C by Loges et al. [2013] using a HKF regression to 800 °C and a fluid density equal to that of the simulations. There are no stability data of Y chloride complexes available but due to the similarities of yttrium and holmium (Ho) chloride complexes at room temperature [Luo and Byrne, 2001] the behavior of Y chloride complexes is assumed to be similar to Ho chloride complexes [Migdisov et al., 2019]. The Ho chloride HKF parameters are taken from Haas et al. [1995], Migdisov et al. [2009]. In addition, Y/Ho-OH^- stabilities are derived from data of Shock et al. [1997], Haas et al. [1995]. The results are shown in Fig 3.11a-d.

Comparing the results in Fig. 3.11a it can be observed that the stability of YCl^{2+} and YCl_2^+

correlates with that of the Ho chloride species within approximately one logarithmic unit. For β_3^{Cl*} and β_3^{Cl}, Y and Ho show opposite behavior. In this case an increase in the stability for the AIMD data can be seen, whereas the Ho β_3^{Cl} decreases [Haas et al., 1995]. Migdisov et al. [2009] do not report any β_3^{Cl} values. For Y and Ho hydroxide species the stabilities are in the range of YCl^{2+}. At high density conditions in Fig. 3.11b the HKF model does not yield stable Ho/Y chloride species whereas the AIMD does for YCl^{2+} and YCl_2^+. But the formation of Y-OH^- in the AIMD runs suggests that there is an Y hydroxide association in high density brines.

Due to the lack of AIMD $\log \beta^F$ data Fig. 3.11c only shows values derived from the HKF parameters. Here, the Y fluoride species [Loges et al., 2013] have the highest stability in comparison to Ho-fluoride [Migdisov et al., 2009, Haas et al., 1995], Y hydroxide [Shock et al., 1997] and Ho-hydroxide [Haas et al., 1995] species. It should be mentioned here that the model from [Haas et al., 1995] is suspected to overestimate the HREE-F stability [Migdisov and Williams-Jones, 2014]. In Fig. 3.11d it is shown that for a higher fluid density the β_1^{F*} values from the simulations are consistent with regression based on experimental data [Loges et al., 2013] within one log unit. The formation constant of YF_2^- from Loges et al. [2013] is larger compared to the AIMD results. On the other hand, the Ho-fluoride [Migdisov et al., 2009] complexes and the Y/Ho-hydroxide complexes have a much lower stability. The differences in Y-F formation indicates a different behavior of the geochemical twins Y and Ho in fluoride-rich environments, which could explain a fractionation of these elements even at higher pressure of ≈1.3 GPa (T=800 °C) conditions as it was observed e.g. in low P hydrothermal systems [Bau and Dulski, 1995] and discussed by Loges et al. [2013]. Furthermore, the comparable stability of both Y chloride and Ho chloride complexes confirms the comparable geochemical behavior of the ions in chloride-rich solutions as assumed by Migdisov et al. [2019] at lower pressures. At high fluid density, the presented data as well indicate a fractionation of Y/Ho by Cl-rich brines.

The strong divergence for the neutral complexes might be explained by the origin of the HKF parameter. The data from Haas et al. [1995] are derived from thermodynamic predictions based on measurements at 25 °C and 1 bar where only a very small amount of a neutral species is formed and therefore the uncertainties of the prediction increase. This interpretation is

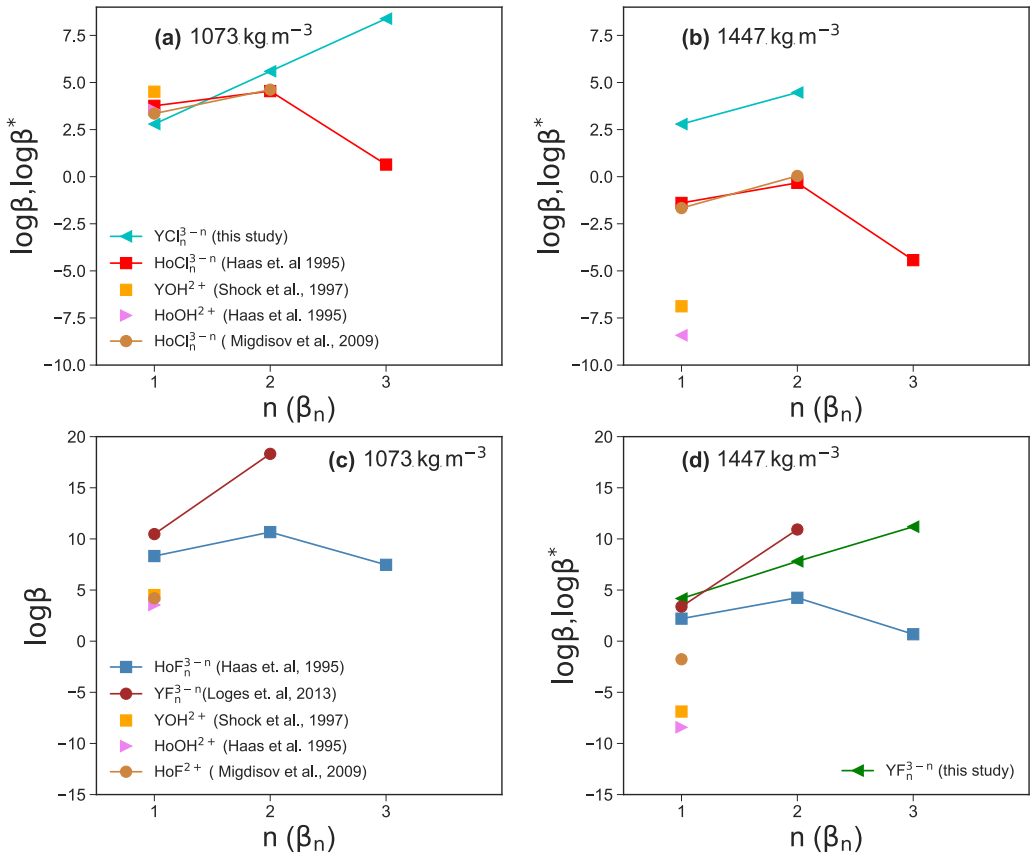

Figure 3.11: (a-d) Comparison of the aqueous species stability derived from the AIMD simulation and HKF regression using the DEW model [Sverjensky et al., 2014] at 800°C and a fluid density of 1072 kg/m^3 and 1447 kg/m^3.

supported by reported experiments of Migdisov et al. [2009] and Loges et al. [2013] who do not observe the formation of neutral complexes up to 250 °C. Only *in situ* measurements by [Mayanovic et al., 2002] show higher Cl coordination of yttrium but at T>250 °C, whereas for Ho no data is available.

The Role of Chloride and Fluoride for the Mobilization of Y^{3+}

Stable Y chloride and Y fluoride complexes are found over the investigated P/T range. The fluoride-bearing species are more stable than the chloride species. This outcome is consistent with a variety of studies from the field (see e.g. Newton et al. [1998]) as well as from

experiments [Hetherington et al., 2010, Tsay et al., 2014, Tropper et al., 2013]. Fig. 3.12a-c shows the distribution of the Y fluoride and chloride complexes as a function of the dissolved salt concentration. In Fig. 3.12d the speciation change as function of the F^- concentration is shown. Beside the presented thermodynamic data from this study competing aqueous reactions as the formation of HCl_{aq}, $NaCl_{aq}$, NaF_{aq}, HF_{aq}, $NaOH_{aq}$, as expected in high grade metamorphic fluids [Aranovich and Safonov, 2018, Galvez et al., 2016, Manning, 2018]) and observed in the simulations, are included. But possible complexation with silica components due to the lack of thermodynamic data as well as mineral reactions are not included. The neutral pH/pOH is fixed by the ion product of water [Marshall and Franck, 1981]. The thermodynamic properties of the competing aqueous species at high P/T condition are computed using the HKF model parameter reported by Mei et al. [2018], Shock and Helgeson [1988], Shock et al. [1997] and Shock et al. [1989] using the DEW model [Sverjensky et al., 2014]. In this simple model a Y concentration of 23 ppm in solution is assumed. This amount corresponds to measurements in subducted material such as mid-ocean-ridge basalt [Sun and McDonough, 1989] and is in the range of Y solubility in Cl^--bearing brines reported by Tropper et al. [2011, 2013], Schmidt et al. [2007a].

Comparing the Y chloride speciation in Fig. 3.12 a,b it can be noted that yttrium is mainly associated with Cl^- at a NaCl concentration of ~0.005 molal in the lower density fluid, whereas at the higher density conditions this state is reached at ~0.01 molal NaCl in solution. For a fluid density of 1072 kg/m^3 YCl_3 is the main species above an NaCl concentration of ~0.01 molal. At high density conditions YCl_2^+ is the major species at a higher NaCl concentration of 0.14 molal. This shows that rather small amounts of dissolved NaCl are needed to form stable Y chloride species at subduction zone P/T conditions if the yttrium is in solution. The required amounts of chloride presumably occurs in subduction fluids as demonstrated in a variety of studies [Barnes et al., 2018, Aranovich and Safonov, 2018]. However, it has been discussed by Tropper et al. [2013] that fluoride aqueous complexes are much more capable to mobilize significant amounts of yttrium. As shown in Fig. 3.12 c for a fluid bearing Y+NaF (in the absence of other ligands) at an NaF concentration of about 0.0014 molal, Y fluoride complexes are the majority species. Deep aqueous fluids in the Earth crust are presumed to be mixtures of H_2O+salt (mainly NaCl, $CaCl_2$, KCl) [Manning, 2018]. Therefore, in Fig. 3.12 d the speciation in a 1 molal NaCl brine

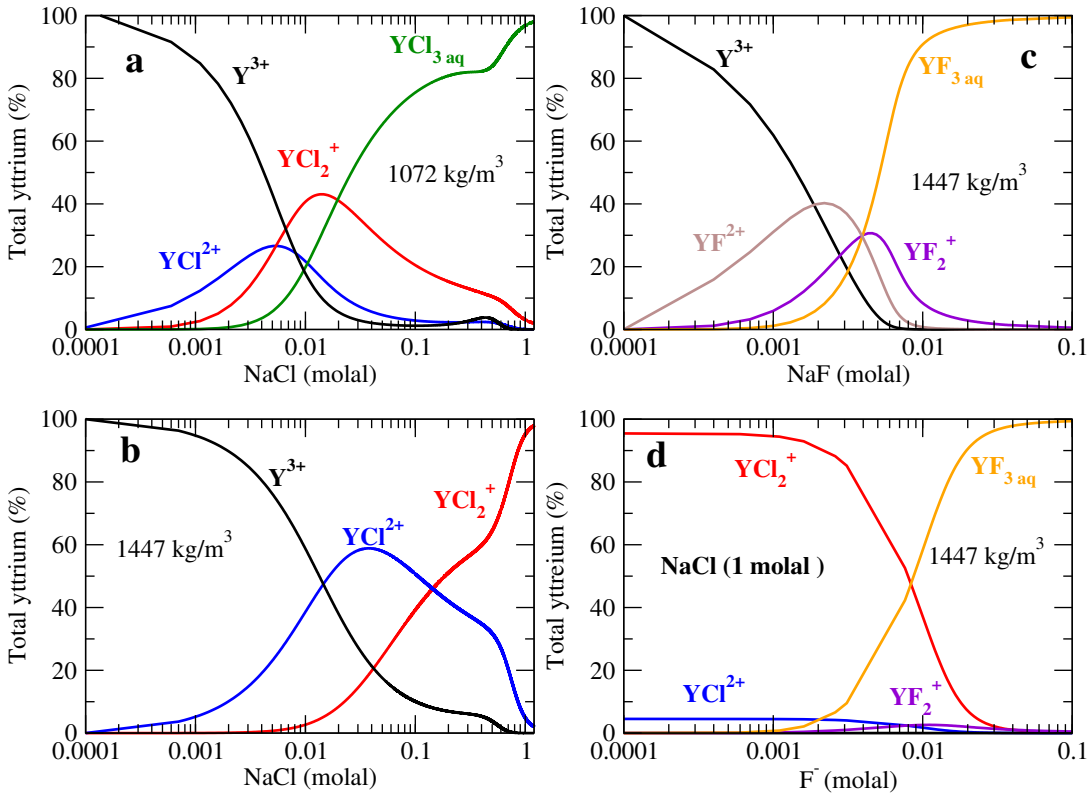

Figure 3.12: Y chloride and fluoride species distribution computed from the AIMD data assuming 23 ppm dissolved yttrium in aqueous solution at 800°C. (a,b) Y chloride species distribution versus the logarithmic sodium chloride concentration in low and high density fluid, (c) Y fluoride species versus the amount of dissolved NaF and (d) Y-Cl/F species in a 1 molal NaCl solution with increasing F^- concentration. The *pH* of the solutions is changing in a range of ±1.7 over the concentration ranges.

with increasing amount of fluoride in the solution at a density of 1447 kg/m^3 is computed. Here, YCl_2^+ and YF_{3aq} are the dominant species. Below a F^- concentration of approximately 0.01 molal, Y chloride complexes are formed and above this concentration Y fluoride becomes more important, at least in high density brines. At lower densities the formation of Y fluoride evolves at lower fluoride concentration due to the strong increase of complex stability as shown in Fig 3.11c.

Estimates of the fluoride content in aqueous phases evolving in subducting slabs are given in the range of ~0.003-0.18 molal derived from analysis of melt inclusions and metamorphic rocks [Portnyagin et al., 2007, Hughes et al., 2018, Aranovich and Safonov, 2018], thermodynamic modeling [Zhu and Sverjensky, 1991] and $f\mathrm{HF}/f\mathrm{H_2O}$ ratio based on partition between mineral and fluid [Sallet, 2000, Yardley, 1985]. The simple model outlined above shows that only a low fluoride concentration in the metamorphic aqueous fluids is needed to change the yttrium

speciation and therefore its mobility. This outcome is in line with recent thermodynamic modeling by Xing et al. [2018] that shows that a small amount of dissolved F^- (tens of ppm) in ore forming solution in equilibrium with a granite assemblage is able to mobilize significant amount of REE. But the high immobility of yttrium in crustal as well subduction zone metasomatism [Ague, 2017] might reflect a low fluorine activity in the majority of metasomatic fluids due to formation of fluoride species, e.g. HF_{aq}, HF_2^-, SiF_6^{2-} or $Si(OH)_2F_{2(aq)}$. Therefore the included thermodynamic properties of HF from Shock et al. [1989] might underestimate its stability. A very low solubility of yttrium-bearing minerals as suggested by Migdisov et al. [2016] and the retrograde solubility of REE phosphates [Schmidt et al., 2007a, Cetiner et al., 2005] could play an important role in the fixation of yttrium and other HREE.

At high densities, the stability of Y hydroxide complexes might be higher than the HKF regression indicates. As shown by Liu et al. [2012], at room temperature the Y-OH^- complexation is sensitive to *pH* changes and could evolve under more alkaline conditions as presumed for deep metasomatism [Galvez et al., 2016]. But with the applied methods in this study no further statement can be made due to the limitations of the PMF thermodynamic integration approach to extract reaction free energies for all relevant individual reactions including different intermediate states and dynamic changes such as proton transfer. To overcome this problem multiple constraints could be applied as suggested by Ivanov et al. [2006] but this would lead to even longer simulation times and might require more than the available computation resources for reaching sufficient convergence of structures and energies [Mark et al., 1994]. Therefore, other free energies sampling methods could be promising alternatives, e.g. the metadynamics approach [Laio and Parrinello, 2002]. This method has been successfully applied to compute acid constant in combination with quantum mechanical molecular dynamics (e.g. Sakti et al. [2018], Tummanapelli and Vasudevan [2015a]) and to find new reaction pathways (see Pérez de Alba Ortíz et al. [2018], Pietrucci et al. [2018]). To probe aqueous systems or mineral-fluid interactions of more realistic size and composition classical molecular dynamics simulations in combination with force field interaction potentials or/and machine learning potentials [Behler and Parrinello, 2007, Cheng et al., 2019] certainly have potential to provide significant progress in this field.

3.4 Summary and Conclusion

The results of the *ab initio* molecular dynamics simulations provide new insight into the Y-Cl, -F and -OH^- complexation in highly saline solutions as they occur in geological settings, e.g. of subduction zones. Firstly, Y chloride aqueous complexes are observed at 800 °C and 1.3 or 4.5 GPa where YCl_3 and YCl_2^+ are the major species. Moreover, the destabilization of YCl_4 and YCl_5 indicate that there are no other Y chloride species that have to be considered at least in high grade metamorphic processes.

The extracted thermodynamic properties of Y chloride species presented in this study are the first published data set to my knowledge. The stabilities correlated with thermodynamic calculation based on HKF regression of Ho chloride complexes [Migdisov et al., 2009] at a solution density of 1073 kg/m^3. That observation suggests, that Y and Ho behave very similar in Cl^- rich solutions but with increasing solution density Y chloride complexes are more favorable than Ho chloride complexes. A much stronger Y fluoride association compared to Ho, which could explain their different behavior in F-rich aqueous environments is found. A different association behavior of this elements with respect to OH^- would have an even higher impact on the Y/Ho fractionation because mineral solubilities and mineral surface adsorption are much more controlled by the pH/pOH value than the halide content of the aqueous fluid.

The formation of Y fluoride complexes in high density aqueous fluids happens even at very low F^- concentrations and should lead to a high mobility of Y (HREE) as observed in natural samples. Only in very fluorine-rich environments (e.g Pan and Fleet [1996], Harlov et al. [2006]) significant amounts of HREE are mobilized. As discussed by Ague [2017] is the HREE mass change by fluid-rock interaction much more correlated with the mineral assemblages and phosphate mobility and therefore the halide content of the fluid phase might not be the only controlling factor for the HREE mobility. Nevertheless, the thermodynamic data reported here correlate with the results of the HKF regression [Loges et al., 2013]. Furthermore, the stability constants are effected by the formation of hydroxide mixed complexes and HCl/HF formation during the thermodynamic integration. Therefore, the presented thermodynamic quantities can only be considered as semi-quantitative. Furthermore, it must be emphasized that the applied activity correction could be a source of huge uncertainty. As demonstrated by Hünenberger and McCammon [1999] does the Ewald summation, that is used to build up the periodic

boundary condition within the simulation, disrupt the solvation free energy of highly charged ions. But this kind of perturbation is not accounted in the Debye–Hückel approach. Therefore, more systematical evaluation of the impact of artificial periodic electrostatics and neutralizing background charge on the computed thermodynamic properties derived from AIMD simulations especially at high temperatures are necessary.

Chapter 4

CASE STUDY II: BERYLLIUM-FLUORIDE COMPLEXATION IN HYDROTHERMAL AND LATE MAGMATIC FLUIDS FROM FIRST PRINCIPLES MOLECULAR DYNAMICS

Beryllium (Be) is a rare element on Earth. Its average concentration in the continental crust amounts merely to 1.8 ppm [Wedepohl, 1995]. Nevertheless, Be is a main component in nearly 90 minerals [Grew, 2002a] in a wide range of geological environments such as pegmatites [Černý, 2002], metamorphic rocks [Grew, 2002b] and beryllium deposits [Jaskula, 2013]. Knowledge of the transport mechanisms of Be^{2+} in nature provides a key to understand this accumulation in more detail. Fluids play an important role for the mobilization of beryllium in geological processes. Moreover, the formation and breakdown of Be minerals such as beryl or bertrandite in magmatic and metamorphic systems require the presence of a fluid phase [Franz and Morteani, 2002, Markl and Schumacher, 1996].

From an economic point of view, beryllium is a strategic element (see USGS report 2016 [1]) with a wide range of applications. For instance, it is used as a neutron moderator material [Grew, 2002a] due to its low absorption cross-section for thermal neutrons. Further, Be is an important light component in metallic glasses, ceramic products or copper- and nickel-based alloys [Jaskula, 2013]. Economic Be deposits are primarily volcanogenic followed by carbonate-hosted epithermal and pegmatite-related deposits [Foley et al., 2012], which are all formed by the interaction of rocks or melts with hydrothermal fluids. The frequent association of beryllium minerals with fluorite and topaz in such deposits [Beus, 1966, Bulnaev, 1996, Foley et al., 2012] lead to the conclusion that fluorine is involved in the transport of Be^{2+} in natural systems.

From a geochemistry perspective, low atomic mass elements such as beryllium, lithium or boron are used as tracers for different processes, e.g. deep melting in subducted oceanic slabs. The strong fractionation of boron (B) and Be [Morris et al., 1990] is commonly explained by a fluid-mediated mobilization of the light elements [Bebout et al., 1993]. To improve mobility

[1] U.S. Geological Survey, Mineral commodity summaries 2016

models for light elements (e.g. Marschall et al. [2007]) the physico-chemical properties of aqueous fluids in high temperature and high pressure environments need to be known.

Beryllium is especially difficult to study experimentally as it is toxic and virtually invisible to X-rays. Due to these challenges, very limited data of properties of Be^{2+} species in geological fluids at high P/T conditions is available. The geochemical behavior of beryllium in epithermal and mesothermal aqueous fluids was studied in great detail by Wood [1992] using thermodynamic modeling. In his study, the author used the isocoulombic method [Lindsay, 1980, Ruaya, 1988] and a three terms (stability constant, enthalpy and entropy) based thermodynamic model [Helgeson, 1967, 1969] to extrapolate the stabilities of different aqueous Be species (with OH^--Cl^--F-CO_3^{2-} ligands) up to 300°C at saturated vapor pressure. Wood [1992] concluded that the highest Be concentration, reaching up to 1,000 ppm at 200 °C in epithermal fluids, can be achieved by forming beryllium-fluoride complexes BeF_3^- and BeF_4^{2-} at high F^- activity (up to 0.3 molal) in a very narrow range of conditions, i.e. near neutral pH, high potassium activity and low calcium activity. It has been suggested that such conditions prevailed during the formation of some Be deposits (e.g. Reyf [2011], Damdinova and Reyf [2008]).

In experimental studies it was shown that the beryllium concentration in silicate melts increases with fluorine content (see e.g. Evensen et al. [1999]). The high beryllium content in fluorine-rich rhyolitic melts as known from field observations [Dailey et al., 2018] indicates that fluorine could play a more important role for the transport of beryllium in natural systems than predicted by existing thermodynamic models [Wood, 1992]. Evidence for the high mobility of beryllium was reported for B-, P-, and F-rich pegmatitic systems from the analysis of melt inclusions with Be concentrations up to 10,000 ppm (or even 38,000 ppm in the Muiane hambergite-bearing inclusion [Thomas and Davidson, 2010]) and fluid inclusions with 2,300 up to 4,500 ppm Be [Reyf and Ishkov, 1999, Thomas et al., 2010] . These very high Be concentrations and the apparent high mobility of Be in late magmatic processes involving aqueous fluids and melts demonstrates the deficiency of present geochemical models of beryllium [Thomas et al., 2011] at crustal T and P conditions.

In contrast to zinc, which is assumed to have a similar geochemical behavior as beryllium [Beus, 1966, Taylor et al., 2003], the association with chlorine does not seem to play a significant role in the transport of Be in aqueous hydrothermal environments, even if Cl is the most abundant

halogen in geological fluids. The stability constants of Be-Cl complexes are very low (see e.g. Hardy et al. [1961]) and solubility experiments in NaCl brines for beryl and phenakite by Syromyatnikov et al. [1972] up to 100 MPa and 800 °C shows no significant impact of the chlorine content on the stability of these minerals. Based on the current knowledge, beryllium fluoride complexes seem to be the most important components for Be transport in aqueous fluids. However, besides the thermodynamic modeling based on potentiometrical measurements at room temperature by Wood [1992], Sverjensky et al. [1997] only one *in situ* data set for on Be-F complexes at high temperatures and saturated vapor pressure is available so far [Koz'menko et al., 1985, 1987].

Aim of this Case Study

Here, the molecular structure of Be^{2+} in fluorine-rich aqueous fluids is investigated to make predictions of the complexation of Be^{2+} with fluoride in geological aqueous fluids from ambient conditions up to 700 °C and 600 MPa using *ab initio* molecular dynamics. In this study, monomeric complexes are highlighted because higher polymeric aqueous complexes of beryllium are only important for temperatures below 60 °C [Brown and Ekberg, 2016] and therefore they should not be significant for geological fluids.

4.1 Computation and Thermodynamic Approach

All present simulation were performed using the CPMD code [CPMD, 1990, Marx and Hutter, 2000]. Within the simulation, to separate the electronic and nuclear motion, a fictive mass of 600 a.u, a fictive kinetic energy of 0.12 a.u. and a simulation time step of 0.1 fs were chosen. All simulations were performed in the NVT ensemble, i.e. at constant number of atoms N, volume V and temperature T. The initial structure was derived from a previous study of aqueous strontium-(Sr) chloride solutions [Borchert et al., 2014]. By substitution of Sr and chloride by beryllium and fluoride a structure of 61 H_2O molecules, four F and one Be atoms was constructed. To avoid fuhrer ion-ion interaction as in case study I in chapter 3 no further cation was added for charge compensation. Therefore, a neutralizing background charge was added to simulation box [Marx and Hutter, 2012]. The concentration in the simulation box corresponds to an aqueous solution of 3.6 molal fluoride and 0.9 molal beryllium. After the substitution of the ions the model solution was equilibrated for several tens of picoseconds at

727 °C and a fluid density of 782 kg/m^3. This density is close to that observed in fluid inclusions carrying a significant amount of beryllium (e.g. ρ =820 kg/m^3 in Reyf [2004]). To approximate the fluid pressure in the simulation volume at a certain temperature, the equation of state for pure water from Wagner and Pruß [2002] (IAPWS) was applied. Subsequently, the temperature in the simulation cell was reduced in two steps to 427 °C and 260 °C at the same density. A simulation box at room temperature and a fluid density of 998 kg/m^3, which resembles the density used by Marx et al. [1997] for purely hydrated Be^{2+} at atmospheric pressure was set up. The three new systems were equilibrated for several picoseconds. The conditions of the four different simulations are summarized in Table 4.1.

Table 4.1: Simulation parameters for the simulation cells with 61 H_2O molecules, 1 Be and 4 F atoms (and a charge compensating background).

Index	Density (kg/m^3)	Temperature (°C)	Pressure (MPa)	a (Å)
a	998	25	0.1	12.54
b	782	260	5^{sat}	13.53
c	782	427	220	13.53
d	782	727	600	13.53

^{sat} saturated vapor pressure, $a-$ simulation cell edge length

Thermodynamic integration along a certain integration variable is a suitable method to derive free energy differences between different states from AIMD simulations. In this case study, four different dissociation reactions were investigated of the form:

$$BeF_n^{2-n} \rightarrow BeF^{3-n}_{n-1} + F^- \quad (n = 1 - 4) \tag{4.1}$$

In the following sections the reactions are named by the index #n and letters $a - d$ to indicate the four different P/T conditions (see Table 4.1).

To study the stability of monomeric beryllium-fluoride species, BeF_n^{2-n}, I started with a BeF_4^{2-} complex and subsequently removed one F^- ligand from the Be^{2+} cation in 16 integration steps by constraining the respective Be-F distance. It is well known that the convergence of thermodynamic integration is highly dependent on the simulation time [Mark et al., 1994]. Moreover, at low temperatures hysteresis can be an issue, which has to be considered very carefully. The AIMD simulation of every integration step includes an equilibration run of more than 0.3 ps followed by a production run of at least 6 ps. This simulation time proved to be

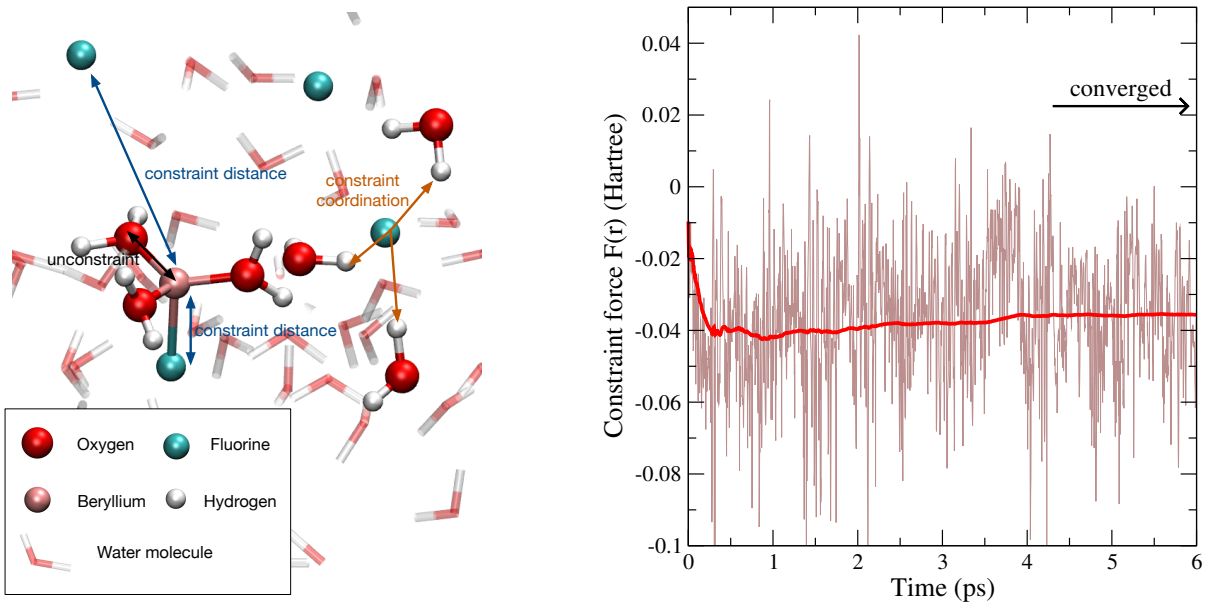

Figure 4.1: Left: Snapshot from the simulation of the reaction $[BeF(H_2O)_3]^+$ to $[Be(H_2O)_4]^{2+}$. The distance between the beryllium and the dissociating fluoride is constrained to 2.1 Å. All remaining fluoride ions are constrained at a Be-F distance of 6.0 Å. To avoid the formation of OH^- and HF the F^- coordination is constrained as well. Right: Evolution of the constraint force $F(r = 2.1\,\text{Å})$ during the 6 ps AIMD simulation in light brown and the moving average in red.

a suitable compromise between convergence of the free energies and computational cost. An example is shown in Fig. 4.1 where the constraint force is converged after 4 ps.

Fig. 4.1 also shows a snapshot from one integration step of the dissociation reaction (including the hydration water molecules):

$$[BeF(H_2O)_3]^+ + H_2O \rightarrow [Be(H_2O)_4]^{2+} + F^- \tag{4.2}$$

The distance of the dissociating fluoride is constrained to 2.1 Å and the distances of the already dissociated fluoride ions are fixed at 6.0 Å. The evolution of the constraint force between both ions along the 6 ps simulation is also illustrated in Fig. 4.1. Already at room temperature but much more frequently at higher temperatures, the water molecules start to hydrolyze and hydrofluoric acid is formed. To avoid the formation of hydrofluoric acid in the reactions the hydrogen coordination of the dissociated fluorides in all simulations is also constrained to zero within an intramolecular HF distance of 1.4 Å.

As shown in previous case studies in high temperature aqueous geochemistry it is generally accepted to estimate the activity coefficients of at least all charged solutes with the modified Debye–Hückel equation developed (see e.g. Tagirov and Seward [2010]) to correct the reaction

Gibbs energy $\Delta_r G$ for the standard state. This method was used, e.g., in the study by Mei et al. [2016] for data sets from AIMD simulations. However, the cation-cation interaction in a periodic system with only one cation per simulation box will not be the same as in real solutions [Hünenberger and McCammon, 1999]. Here, $\Delta_r G^\circ$ is calculated by neglecting the interactions between molecules in adjacent cells and also the anion-anion interactions to achieve the standard state ($\Delta_r G$=$\Delta_r G^\circ$). It is necessary to clarify that all given thermodynamic data including reference studies refers to 1 molal solution. To extrapolate or interpolate the thermodynamic data of the standard state derived from the simulation started with a modified Ryzhenko-Bryzgalin model [Ryzhenko et al., 1985, M. V Borisov and Shvarov, 1992, Shvarov and Bastrakov, 1999] for each species in P/T space is applied.

4.2 Results and Discussion

Aqueous Be-F Complexes

All conventional AIMD runs were performed for at least 20 ps. In none of the AIMD runs an exchange of coordinating fluorides (see Table 4.2) is observed. This observation agrees with *in situ* NMR measurements, which show very slow exchange rates within the time scale of μs to ms [Schmidbaur, 2001]. Furthermore, this indicates a high stability of Be-F bond. But a dynamic exchange of water molecules in the first hydration shell of the beryllium ion can be found. This exchange becomes more frequent with increasing T.

All aqueous species investigated by AIMD simulation are illustrated in Fig. 4.2. They include the fluoride species $[BeF_4]^{2-}$, $[BeF_3(H_2O)]^-$, $[BeF_2(H_2O)_2]_{aq}$ and $[BeF(H_2O)_3]^+$ that were reported in an NMR spectroscopy study of Liu et al. [2014]. Moreover, simulations were made for the fully hydrated $[Be(H_2O)_4]^{2+}$ species that was observed by X-ray diffraction [Yamaguchi et al., 1986] and Raman spectroscopy [Rudolph et al., 2009]. At room temperature all complexes are tetrahedrally coordinated by water and/or fluoride over the whole AIMD simulation run (see Fig. 4.3). Even if the initial configuration is trigonal, for example starting from $[BeF_3]^-$, after 0.12 ps $[BeF_3(H_2O)]^-$ is formed. Furthermore, in a fluoride free environment $[Be(H_2O)_4]^{2+}$ is formed in agreement with experimental results by Mesmer and Baes [1969] and first principles simulations by Marx et al. [1997]. Moreover, reported Be-O distances by Marx et al. [1997] of 1.65 Å for purely hydrated beryllium in aqueous solutions are an agreement with observations

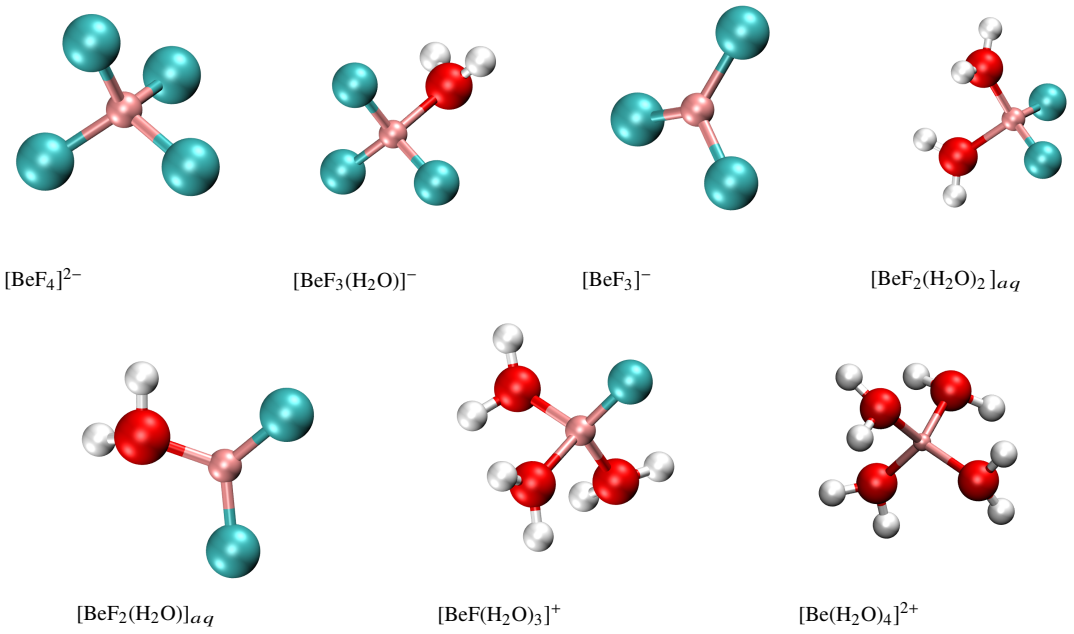

Figure 4.2: Beryllium-fluoride complexes sampled in the AIMD simulation run.

---

in this study of 1.64 Å. This distance increases linearly with F coordination to 1.70 Å in $[BeF_3(H_2O)]^-$. The change of the second hydration shell between the Be-F complex is not substantial at room temperature (see Table 4.2). For the average Be-F distances we also observe only small variations between the complexes. $[BeF_4]^{2-}$ and $[BeF_3(H_2O)]^-$ have the same bond distance of 1.58 Å whereas the mean Be-F distances in $[BeF_2(H_2O)_2]_{aq}$ and $[BeF(H_2O)_3]^+$ are 1.56 Å.

Table 4.2: Geometrical properties of the investigated aqueous Be-F complexes. The superscript for the Be-O distance correspond to the first ([1]) and second ([2]) hydration shells, CN is the coordination number.

			Conditions		Distances (Å)			Coordination numbers		
Initial complex	Dominant complex	Geometry	T (K)	P (MPa)	Be-F	Be-O^1	Be-O^2	CN_{Be-F}	CN_{Be-O}	CN_{sum}
BeF_4^{2-}	BeF_4^{2-}	tetrahedral	25	0.1	1.58		3.80	4.0		4.0
BeF_3^-	$BeF_3(H_2O)^-$	tetrahedral	25	0.1	1.58	1.70	3.75	3.0	0.9	3.9
$BeF_2(H_2O)_{(aq)}$	$BeF_2(H_2O)_{2\,aq}$	tetrahedral	25	0.1	1.56	1.68	3.75	2.0	2.0	4.0
$BeF(H_2O)_3^+$	$BeF(H_2O)_3^+$	tetrahedral	25	0.1	1.56	1.66	3.80	1.0	3.0	4.0
$Be(H_2O)_4^{2+}$	$Be(H_2O)_4^{2+}$	tetrahedral	25	0.1		1.64	3.76		4.0	4.0
BeF_4^{2-}	BeF_4^{2-}	tetrahedral	260	5	1.57		3.75	4.0		4.0
BeF_3^-	$BeF_3(H_2O)^-$	tetrahedral	260	5	1.57	1.84	3.94	3.0	0.9	3.9
$BeF_2(H_2O)_{aq}$	$BeF_2(H_2O)_{2\,aq}$	tetrahedral	260	5	1.54	1.73	3.90	2.0	2.0	4.0
$BeF(H_2O)_3^+$	$BeF(H_2O)_3^+$	tetrahedral	260	5	1.52	1.66	3.86	1.0	3.0	4.0
$Be(H_2O)_4^{2+}$	$Be(H_2O)_4^{2+}$	tetrahedral	260	5		1.63	3.79		4.0	4.0
BeF_4^{2-}	BeF_4^{2-}	tetrahedral	427	220	1.59		3.82	4.0		4.0
BeF_3^-	BeF_3^-	trigonal	427	220	1.52	1.84	3.96	3.0	0.3	3.3
$BeF_2(H_2O)_{(aq)}$	$BeF_2(H_2O)_{2\,aq}$	tetrahedral	427	220	1.52	1.70	4.04	2.0	1.8	3.8
$BeF(H_2O)_3^+$	$BeF(H_2O)_3^+$	tetrahedral	427	220	1.50	1.67	3.86	1.0	3.0	4.0
$Be(H_2O)_4^{2+}$	$Be(H_2O)_4^{2+}$	tetrahedral	427	220		1.63	3.83		4.0	4.0
BeF_4^{2-}	BeF_4^{2-}	tetrahedral	727	600	1.57		3.98	3.9		3.9
BeF_3^-	BeF_3^-	trigonal	727	600	1.52	1.86	4.01	3.0	0.3	3.3
$BeF_2(H_2O)_{aq}$	$BeF_2(H_2O)_{aq}$	trigonal	727	600	1.50	1.63	4.01	2.0	1.4	3.4
$BeF(H_2O)_2^+$	$BeF(H_2O)_3^+$	tetrahedral	727	600	1.50	1.66	3.91	1.0	2.9	3.9
$Be(H_2O)_4^{2+}$	$Be(H_2O)_4^{2+}$	tetrahedral	727	600		1.61	3.89		3.6	3.6

At 260 °C and saturated vapor-pressure all species are tetrahedrally coordinated by H_2O and F^- (see Fig. 4.3) but compared to ambient conditions the difference in the Be-F and Be-O distance becomes more significant (see Table 4.2). $[BeF_4]^{2-}$ and $[BeF_3(H_2O)]^-$ show the largest Be-F bond distances with 1.57 Å and $[BeF(H_2O)_3]^+$ the shortest with 1.52 Å.

At 427 °C and 220 MPa, a new species without hydration water, $[BeF_3]^-$, seems to become stable. To verify this observation the simulation is initially started from a $[BeF_3(H_2O)]^-$ complex and after 0.08 ps it dissociates into $[BeF_3]^-$ and H_2O. This non-hydrated complex is stable over more than 10 ps followed by two short re-associations to $[BeF_3(H_2O)]^-$ for nearly 2 ps. The reduction in coordination is associated with change in Be–F distance from 1.57 Å at 260 °C to 1.52 Å at 427 °C. Fluctuations are also observed in the hydration of $[BeF_2(H_2O)_2]_{aq}$ where after 0.3 ps $[BeF_2(H_2O)]_{aq}$ is formed but $[BeF_2(H_2O)_2]_{aq}$ is still the dominant species over the whole simulation run.

At 727 °C and 600 MPa, the Be-F distances in $[BeF_3]^-$ and $[BeF(H_2O)_3]^+$ are the same as at 427 °C. For $[BeF_2(H_2O)_{1-2}]_{aq}$ we observe a shortening to 1.50 Å, probably due to the reduced number of hydration water molecules (see Fig. 4.3), whereas for $[BeF_4]^{2-}$ the Be-F distance does not vary significantly between the different P/T conditions.

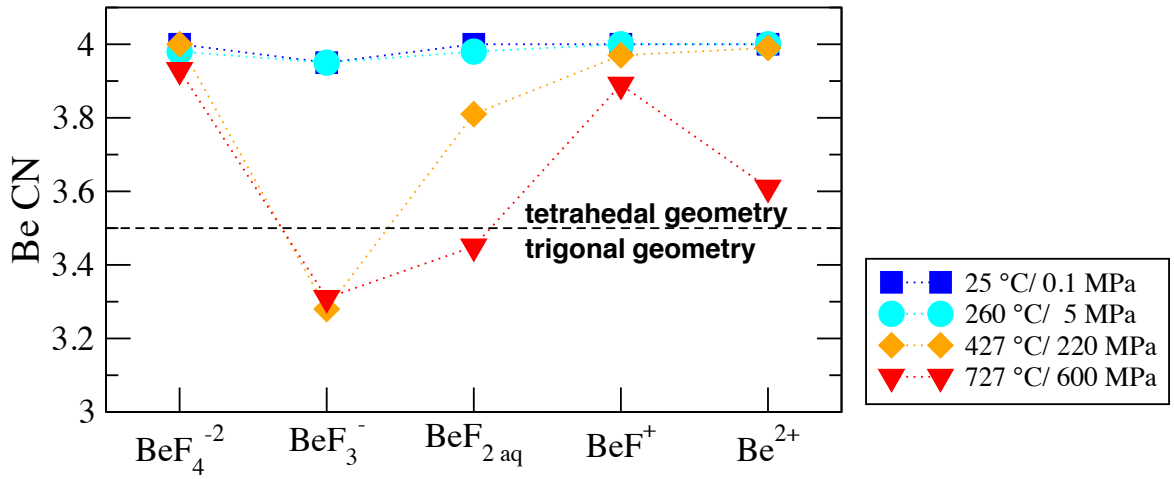

Figure 4.3: Coordination number of beryllium in respect to oxygen and fluoride in the first hydration shell.

As a general trend, the Be-F bond distance decreases with a decreasing number of fluoride ligands and with increasing T. A decrease in the Be-O distance with a decreasing number of fluoride ligands (see Table 4.2) and for $[Be(H_2O)_4]^{2+}$ with increasing temperatures can be

found. On the contrary, raising the temperature results in an increase of the Be-O distance in $[BeF_3(H_2O)_{0-1}]^-$ from 1.70 Å at ambient conditions to a maximum of 1.86 Å at 727 °C, 600 MPa (see Table 4.2). This correlates with a decrease in the Be-F distances and the tendency to form $[BeF_3]^-$ species at high temperatures. In $[BeF_2(H_2O)_{1-2}]_{aq}$, the Be-O distance increases from 1.68 Å at 25 °C to 1.73 Å at 260 °C but then decreases again significantly to 1.63 Å at the highest temperature. This behavior is explained by the reduction of the number of hydration water molecules by transformation from $[BeF_2(H_2O)_2]_{aq}$ to $[BeF_2(H_2O)]_{aq}$, which leads to shorter bond lengths.

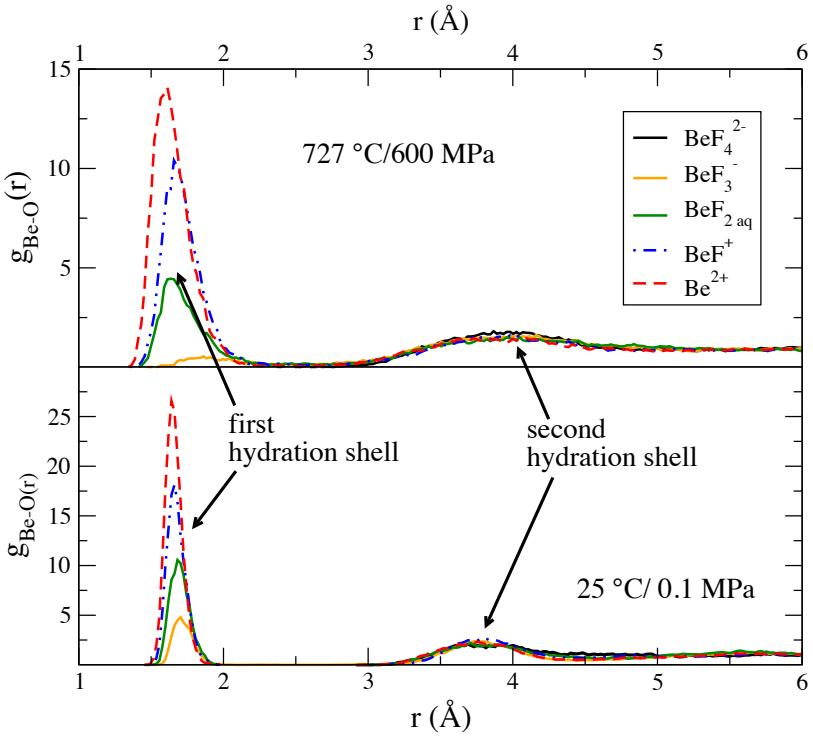

Figure 4.4: Radial distribution function $g_{BeO}(r)$ at room temperature and at 727 °C.

Beside the first hydration shell, which can be found within the first 2.5 Å around the Be^{2+} ion, a second hydration shell persists at a distance between ~3-5 Å up to the highest P/T conditions of this study (see second peak of $g_{Be-O}(r)$ in Fig. 4.4). The distance between the second hydration shell and the Be^{2+} ion changes within the investigated range of conditions. With increasing P/T an increase of the Be–H_2O distance in the second hydration shell for all complexes can be notice. Furthermore, a variation between the species depending on their charge is observed. The charged species build up a closer second hydration shell than the

uncharged species. For instance, for the $[BeF_4]^{2-}$ complex at 427 °C the maximum of $g_{Be-O}(r)$ representing the second hydration shell is found at 3.8 Å, whereas for the unchanged complex $[BeF_2(H_2O)_{1-2}]_{aq}$ the maximum is shifted to a larger distance of 4.1 Å. This variation is driven by the decreasing ability of water to shield the charges of the solute [Seward and Driesner, 2004] at high temperature due to the decreased dielectric constant [Sverjensky et al., 2014].

The main change between low and high P/T conditions is the tendency of beryllium to build up a planar trigonal coordination environment with increasing temperature, which is mainly driven by a decrease in hydration of the beryllium ion. Such a transformation of the hydration environment at high P and high T conditions is also known from other alkaline earth ions such as Sr^{2+} [Harris et al., 2003b].

Free Energy Exploration

As an example the potential of mean force for the dissociation reaction #1b is shown in Fig. 4.5 II. Here, the initial complex $[BeF(H_2O)_3]^+$ is transformed to $[Be(H_2O)_4]^{2+}$ at 260 °C and saturated water pressure. The integration starts at a distance of 1.52 Å, which corresponds approximately to the equilibrium distance of the Be–F contact ion pair from the unconstrained AIMD simulation. Hence, the mean force at this distance is close to zero (Fig. 4.5 A). With increasing displacement of the ligand, the constraint force is attractive (Fig. 4.5 B) until a water molecule takes the place of the fluoride in the first coordination shell of the beryllium (Fig. 4.5 C) and a so called solvent shared ion pair is formed. At this point the force becomes repulsive. By integration over the potential of mean force the Helmholtz free energy difference $\Delta_r A$ between the initial complex and the product of the reaction is derived (Fig. 4.5 II). For the Be-F complexes, we assume a ligand in a distance of about 5 Å from the Be ion as dissociated. The error of the free energy difference is estimated by the standard deviation of the constraint force between 5.2 Å and 5.5 Å. In the following, we present data obtained from the integration up to a cutoff distance of 5.5 Å.

The $\Delta_r A$ values of the four different dissociation reactions at four different P/T conditions are transformed into $\Delta_r G$ of formation reactions ($\Delta_r G = -\Delta_r A$) and the obtained $\Delta_r G$ are compiled in Table 4.3. As already described, the progress of the dissociation reaction is reflected in the change of the constraint force $F(r)$ with increasing Be-F distance. Fig. 4.6 shows the evolution of the cumulative integration representing the change in the Helmholtz free energy $\Delta_r A$ for the

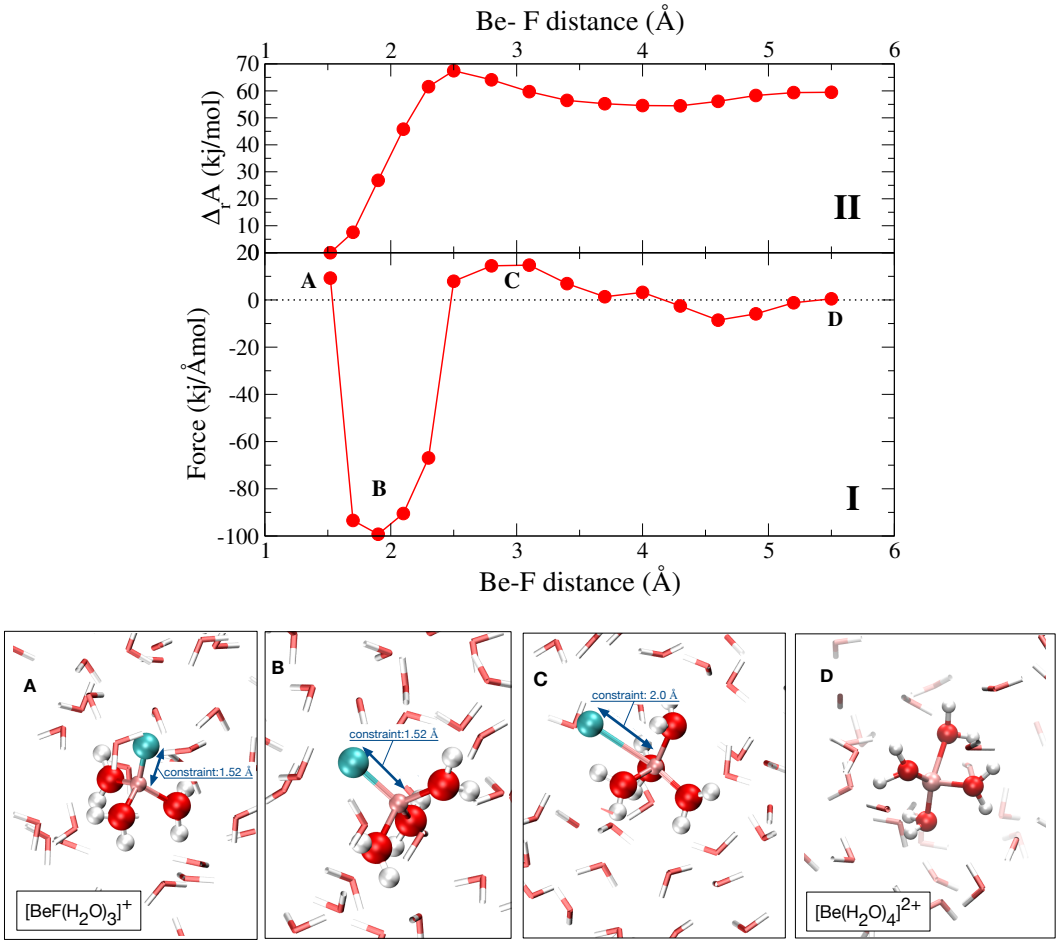

Figure 4.5: (I) Potential of mean force between Be and F during the dissociation of a $[BeF(H_2O)_3]^+$ complex. (II) Cumulative integration of the potential of mean force to determine the change in Helmholtz free energy $\Delta_r A$. (A-D) Snapshots from four exemplary integration steps with different constrained Be-F distances.

---

different dissociation reactions. The convergence of all free energy integrations at elevated P/T appears to be achieved. Only reaction #2a at ambient conditions does not reach equilibrium within in the constraint distance. Such a behavior has also been observed in previous constraint AIMD simulations at room temperature (e.g. Mei et al. [2013]).

At room temperature, reactions #1a (54.8 (2.4) kJ/mol) and #2a (45.8 (5.3) kJ/mol) yield effectively equal $\Delta_r A$. It is exceptional that the formation of a neutral aqueous complex gains a $\Delta_r A$ comparable to that of a charged complex at room temperature due to the high dielectric constant of water. But in case of Be-F complexes the relatively high stability of $BeF_{2\,aq}$ in comparison to the charged species was observed as well in experiments by Mesmer and Baes [1969]. All formation reactions at ambient conditions and at 260 °C lead to a reduction in the

number of hydration water molecules of the initial complexes. This change in hydration drives the balance between attractive and repulsive force in $F(r)$.

Reactions #1b to #4b yield significantly higher energies compared to those at ambient conditions. Between run conditions b (260 °C/5 MPa) and c (427 °C/220 MPa) the free energy difference of reaction #1 does not change significantly with increasing temperature. For #2 $\Delta_r A$ only increase slightly whereas for #3 it increases from 58.6(1.9) kJ/mol to 78.7(7.1) kJ/mol. This significant increase of the stability of BeF_3^- might be explained by the stabilization of the trigonal geometry with increasing temperature, whereas the decrease of the reactions energies in #4 underline this conclusion.

The free energies obtained at 727 °C and 600 MPa for #3d and #4d decrease in comparison to the previous conditions. While the $\Delta_r A$ to form BeF^+ and $BeF_{2\,aq}$ change significantly from 113.4(6.7) kJ/mol to 154.8(1.5) kJ/mol and from 113.0(3.4) kJ/mol to 128.0(1.9)kJ/mol. That change in $\Delta_r A$ could be explained by the preferential formation of low charged species in high T aqueous fluids as observed in a variety of studies (see e.g Manning [2018]).

With increasing P/T conditions an increase of the constraint Be-F distance at which the Be-H_2O association takes place is observed . At room temperature, a water molecule is associated with the Be-F complexes when the constraint Be-F distance reaches ~2.5 Å (reactions #1-3a) or ~2.7 Å (reaction #4a). In reaction #2b, this distance increases to ~2.9 Å and in #3d slightly to ~2.7 Å. For #1 the Be-F distance for the H_2O association (2.5 Å) does not change until 727 °C/600 MPa is reached, where it increases to ~2.7 Å. This changes can be explained by the decreasing solvent hydration of the metal ion (Fig.4.3).

The influence of the second hydration shell on the association of the ions cannot precisely be determined. The change in $F(r)$ at the Be-F distance where the second shell is located is not significant for all of the aqueous reactions. This result suggests on one side that the effect of the outer shell is negligible in this system. But on the other side it could be that the implementation of the rather simple geometric constraints in terms of reaction coordinates do not cover more complex underlying free energy surfaces as indicated by Ivanov et al. [2006]. To overcome this problem it would be necessary to perform simulations with different free energy sampling methods and to compare the results.

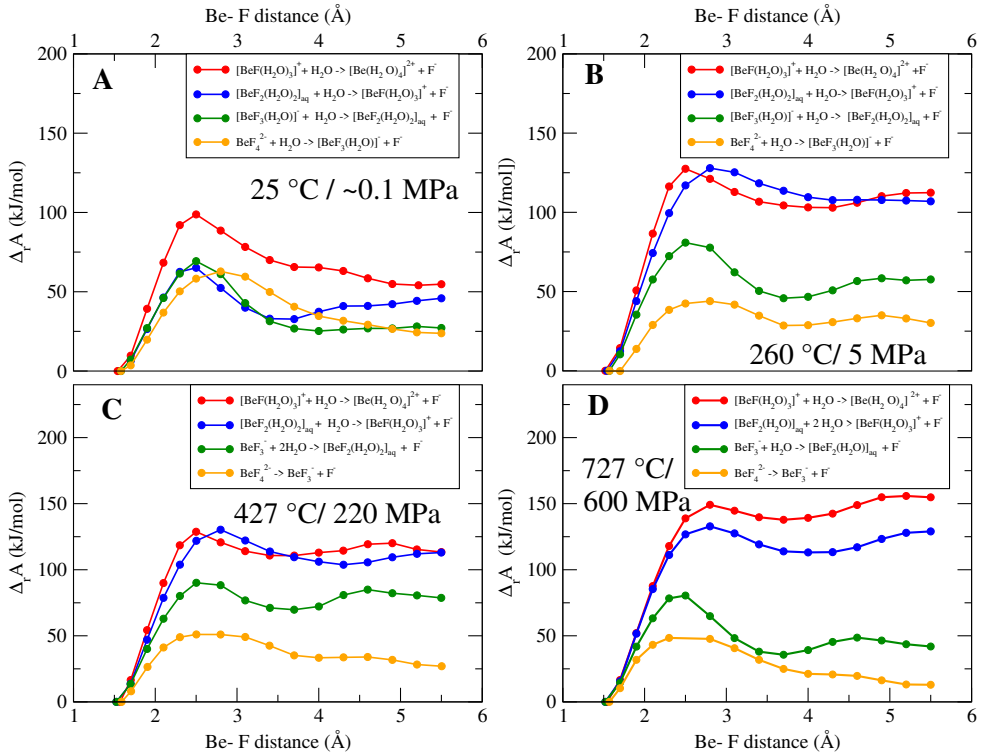

Figure 4.6: Evolution of the Helmholtz free energy difference $\Delta_r A$ as function of Be-F distance for all four complexes (A-D).

Stability Constants of the Be-F Aqueous Complexes

The stability constants of the investigated aqueous species obtained from the thermodynamic integration are listed in Table 4.4. At ambient conditions, they are compared to theoretical prediction based on HKF regression [Sverjensky et al., 1997] and the most complete and reliable experimental data set from Mesmer and Baes [1969], which is based on direct potentiometric measurements. A large variations between the TI-AIMD results and all other studies at ambient conditions can be found. Such huge difference might explained by the already mention inability of the DFT approach to represent long-range electron correlations (section 2.2) as they strongly occurs in water at ambient conditions [Grimme, 2006]. Furthermore, it must be emphasized that the computed energies strongly depends on the applied exchange correlation functional (see Schultz et al. [2005] for a comparison of more than 42 different funtionals).

The only available high temperature experimental data set is given for $BeF_{2\,aq}$ by Koz'menko et al. [1985, 1987] derived from solubility experiments of bromellite (BeO) in HF solution. Apart from that calculated stability constants derived from the isocoulombic approach up to

Table 4.3: Results of the thermodynamic integration. $\Delta_r G^\circ$ are directly converted from $\Delta_r A$ value. Further listed are the equilibrium constants (log K)

No.	Reaction	T (°C)	P (MPa)	$\Delta_r G^\circ$ (kJ/mol)	log K
# 1a	$[Be(H_2O)_4]^{2+}$+F^- →$[BeF(H_2O)_3]^+$+H_2O	25	0.1	-54.8 ± 2.4	9.59 ± 0.42
# 2a	$[BeF(H_2O)_3]^+$+F^- →$[BeF_2(H_2O)_2]_{aq}$+H_2O	25	0.1	-45.8 ± 5.3	8.03 ± 0.92
# 3a	$[BeF_2(H_2O)_2]_{aq}$+F^- → $[BeF_3(H_2O)]^-$+H_2O	25	0.1	-27.8 ± 1.3	4.86 ± 0.23
# 4a	$[BeF_3(H_2O)]^-$+F^- →$[BeF_4]^{2-}$+H_2O	25	0.1	-23.8 ± 2.0	4.16 ± 0.36
# 1b	$[Be(H_2O)_4]^{2+}$+ F^- → $[BeF(H_2O)_3]^+$+H_2O	260	5	-112.4 ± 0.7	11.01 ± 0.07
# 2b	$[BeF(H_2O)_3]^+$+ F^- →$[BeF_2(H_2O)_2]_{aq}$+H_2O	260	5	-106.9 ± 1.5	10.48 ± 0.15
# 3b	$[BeF_2(H_2O)_2]_{aq}$+F^- →$[BeF_3(H_2O)]^-$+H_2O	260	5	-58.6 ± 1.9	5.65 ± 0.19
# 4b	$[BeF_3(H_2O)]^-$+ F^- → $[BeF_4]^{2-}$ + H_2O	260	5	-30.2 ± 9.1	2.96 ± 0.89
# 1c	$[Be(H_2O)_4]^{2+}$+ F^- →$[BeF(H_2O)_3]^+$+H_2O	427	220	-113.4 ± 6.7	8.46 ± 0.50
# 2c	$[BeF(H_2O)_3]^+$+ F^- →$[BeF_2(H_2O)_2]_{aq}$+H_2O	427	220	-113.0 ± 3.4	8.43 ± 0.25
# 3c	$[BeF_2(H_2O)_2]_{aq}$+ F^- →$[BeF_3]^-$+2 H_2O	427	220	-78.7 ± 7.1	5.87 ± 0.53
# 4c	BeF_3^-+F^- → BeF_4^{2-}	427	220	-26.7 ± 2.1	1.99 ± 0.16
# 1d	$[Be(H_2O)_4]^{2+}$+F^- →$[BeF(H_2O)_3]^+$+H_2O	727	600	-154.8 ± 1.5	8.09 ± 0.14
# 2d	$[BeF(H_2O)_3]^+$+F^- →$[BeF_2(H_2O)]_{aq}$+2 H_2O	727	600	-128.0 ± 1.9	6.47 ± 0.19
# 3d	$[BeF_2(H_2O)]_{aq}$+ F^- → $[BeF_3]^-$+H_2O	727	600	-41.9 ± 3.0	2.19 ± 0.29
# 4d	BeF_3^-+F^- →BeF_4^{2-}	727	600	-16.8 ± 3.7	0.88 ± 0.37

300 °C and saturated water pressure by Wood [1992] and prediction by Sverjensky et al. [1997] using the HKF model are available in the literature. Furthermore, the stability constants of the beryllium fluoride species in the temperature range of the AIMD simulations computed using the SUPCRTBL code [Zimmer et al., 2016], which is an updated version of widely used SUPCRT92 code [Johnson et al., 1992] in conjunction with the included species database (slop98.dat) are listed. These thermodynamic calculations also based on the HKF model (slop98.dat includes parameter from Sverjensky et al. [1997]). In Fig. 4.7 the AIMD results and the fit of the AIMD results using the Ryzhenko-Bryzgalin (RB) model along the water vapor pressure curve (P_{sat}) and for each P/T condition of the simulation is shown. The applied model parameters are listed in Table 4.5. Due to the huge imbalance between the stability constants derived from the AIMD simulation and the sufficiently reliable data by Mesmer and Baes [1969], at room temperature, thus experimental values are used for RB model. The stability constants derived from the simulations at T=260 °C (P_{sat}) for $BeF_{2\,aq}$, BeF_3^+ and BeF_4^{2-} are approximately twice as high as the reported values by Wood [1992] and for BeF^+ the difference being ~5 log values.

The fit of the RB provides accurate values for $BeF_{2\,aq}$ and BeF_4^{2-} .The largest deviation are observed at 427 °C and 220 MPa for $BeF_{2\,aq}$ and BeF_3^-. However, it must be considered that the

Table 4.4: Logarithmic stability constants of BeF species.

Reaction	T (°C)	P (MPa)	log β_{AIMD}	Exp. data	Theo. data
$Be^{2+} + F^- \rightarrow BeF^+$	25	0.1	9.6	5.52 ^{MB}	0.4 ^{SC} , 5.6 ^{SSH}
$Be^{2+} + 2F^- \rightarrow BeF_{2\,aq}$	25	0.1	17.6	9.58 ^{MB}	4.5 ^{SC} , 9.7 ^{SSH}
$Be^{2+} + 3F^- \rightarrow BeF_3^-$	25	0.1	22.5	12.46 ^{MB}	7.3 ^{SC} , 12.5 ^{SSH}
$Be^{2+} + 4F^- \rightarrow BeF_4^{2-}$	25	0.1	26.7	13.67 ^{MB}	7.9 ^{SC} , 13.1 ^{SSH}
$Be^{2+} + F^- \rightarrow BeF^+$	260	5	11.0		11.5 ^{SC} , 15.9 ^{SSH} , 7.0 ^{W}
$Be^{2+} + 2F^- \rightarrow BeF_{2\,aq}$	260	5	21.5	11.14 ^{K}	16.9 ^{SC} , 21.0 ^{SSH} , 10.6 ^{W}
$Be^{2+} + 3F^- \rightarrow BeF_3^-$	260	5	27.1		23.4 ^{SC} , 27.2 ^{SSH} , 13.4 ^{W}
$Be^{2+} + 4F^- \rightarrow BeF_4^{2-}$	260	5	30.1		33.7 ^{SC} , 37.0 ^{SSH} , 14.5 ^{W}
$Be^{2+} + F^- \rightarrow BeF^+$	427	220	8.5		14.8 ^{SC} , 20.2 ^{SSH}
$Be^{2+} + 2F^- \rightarrow BeF_{2\,aq}$	427	220	16.9		20.8 ^{SC} , 26.5 ^{SSH}
$Be^{2+} + 3F^- \rightarrow BeF_3^-$	427	220	22.8		28.6 ^{SC} , 34.7 ^{SSH}
$Be^{2+} + 4F^- \rightarrow BeF_4^{2-}$	427	220	24.8		41.9 ^{SC} , 48.5 ^{SSH}
$Be^{2+} + F^- \rightarrow BeF^+$	727	600	8.1		23.2 ^{SSH}
$Be^{2+} + 2F^- \rightarrow BeF_{2\,aq}$	727	600	14.8		30.5 ^{SSH}
$Be^{2+} + 3F^- \rightarrow BeF_3^-$	727	600	17.0		40.2 ^{SSH}
$Be^{2+} + 4F^- \rightarrow BeF_4^{2-}$	727	600	17.9		57.1 ^{SSH}

log β_{AIMD} stability constant derived directly from the AIMD results, ^{MB} direct potentiometry data from [Mesmer and Baes, 1969] corrected by Wood [1992] for the standard state, ^{K} high temperature (250°C) data from Koz'menko et al. [1985, 1987] BeF_2 transcript from Wood [1992], ^{SC} HKF regression using SUPCRTBL [Zimmer et al., 2016, Johnson et al., 1992] slop98.dat, ^{SSH} calculated value by Sverjensky et al. [1997] at 25°C/0.1MPa, 200 °C/ P_{sat}, 250°C/5 MPa, 750°C/500 MPa, ^{W} [Wood, 1992] 200 °C/P_{sat}

number of points, which are included in the fit is very limited. For this reason the precision of the model is limited too. Comparing the extrapolation of the RB model with the predictions by Wood [1992] in Fig. 4.7 it is striking that with increasing temperature the difference between both models dramatically increases for all Be-F species. The same applies in respect to the high temperature experiments of Koz'menko et al. [1985, 1987] for $BeF_{2\,aq}$.

The results of the SUPCRTBL modeling and the reported data by Sverjensky et al. [1997] shows as well a huge differences to the results of Wood [1992]. Surprising are the results of the modeling and the reported predictions by Sverjensky et al. [1997] not identical. But they should, because both based on the same HKF values. Furthermore, does the SUPCRTBL modeling not reproduce the experimental log β at ambient condition, whereas the given quantities by Sverjensky et al. [1997] does. This finding implicates that the stored HKF parameter in the thermodynamic data file, that are the same as those given in the manuscript by Sverjensky et al. [1997], are not the correct ones for the Be-F complexes. Comparing the results with the AIMD

under saturated P conditions with the data sets it appears a good correlation for $BeF_{2\,aq}$ and BeF_3^- with Sverjensky et al. [1997]. Whereas, for BeF^+ and BeF_4^{2-} the AIMD results are plotted closer to the SUPCRTBL model.

Table 4.5: Parameters of the modified Ryzhenko–Bryzgalin model obtained with the OptimC code [Shvarov, 2015] derived from the thermodynamic data of the simulation (for T>25 °C). $\log\beta$(25 °C) are taken from Mesmer and Baes [1969]

Reaction	$\log\beta$(25 °C)	A	B
$Be^{2+} + F^- \rightarrow BeF^+$	4.52	0.403	1193
$Be^{2+} + 2F^- \rightarrow BeF_{2\,aq}$	9.14	0.100	2463
$Be^{2+} + 3F^- \rightarrow BeF_3^-$	11.46	-0.383	3408
$Be^{2+} + 4F^- \rightarrow BeF_4^{2-}$	13.70	-0.800	3949

Comparing the stability constants at 260 °C with results at higher T=427, 727 °C conditions from Table 4.3 a decrease in $\log\beta$ values is observed. This decrease is suspicious because one would expect that the association increase of the ions with increasing T at constant density (see Chialvo and Cummings [1999]). This is further in marked difference to the high P/T data of the other thermodynamic models. Therefore, the uncertainties of the simulation might be much as assessed. The main reasons for that could be the constraint F-H coordination and the applied neutralizing background charge density as discussed by Todorova et al. [2008]. The most reliable data point appears to be at 260 °C (P_{sat}). Because the HF formation is strongly constraint by temperature [Ellis, 1963]. Therefore, the impact of its suppression increases with temperature and it should be much stronger for T=427, 727 °C. According to this assumption the BeF aqueous complex are much more stable in hydrothermal solution than pronounced by Wood [1992]. But the low stability of $BeF_{2(aq)}$ in dissolution experiments by Koz'menko et al. [1985, 1987] argue against this assumption.

4.3 Conclusion

This study shows that the tetrahedral coordination in respect to oxygen (H_2O), which is preferred by Be^{2+} at room conditions in aqueous solutions and in minerals [Hawthorne and Huminicki, 2002] tended to become unstable in high temperature F-rich geological fluids. Zinc shows a comparable behavior in hydrothermal solutions, there it undergoes a coordination change from a octahedral to a tetrahedral in a Cl-rich environment [Harris et al., 2003a, Mei

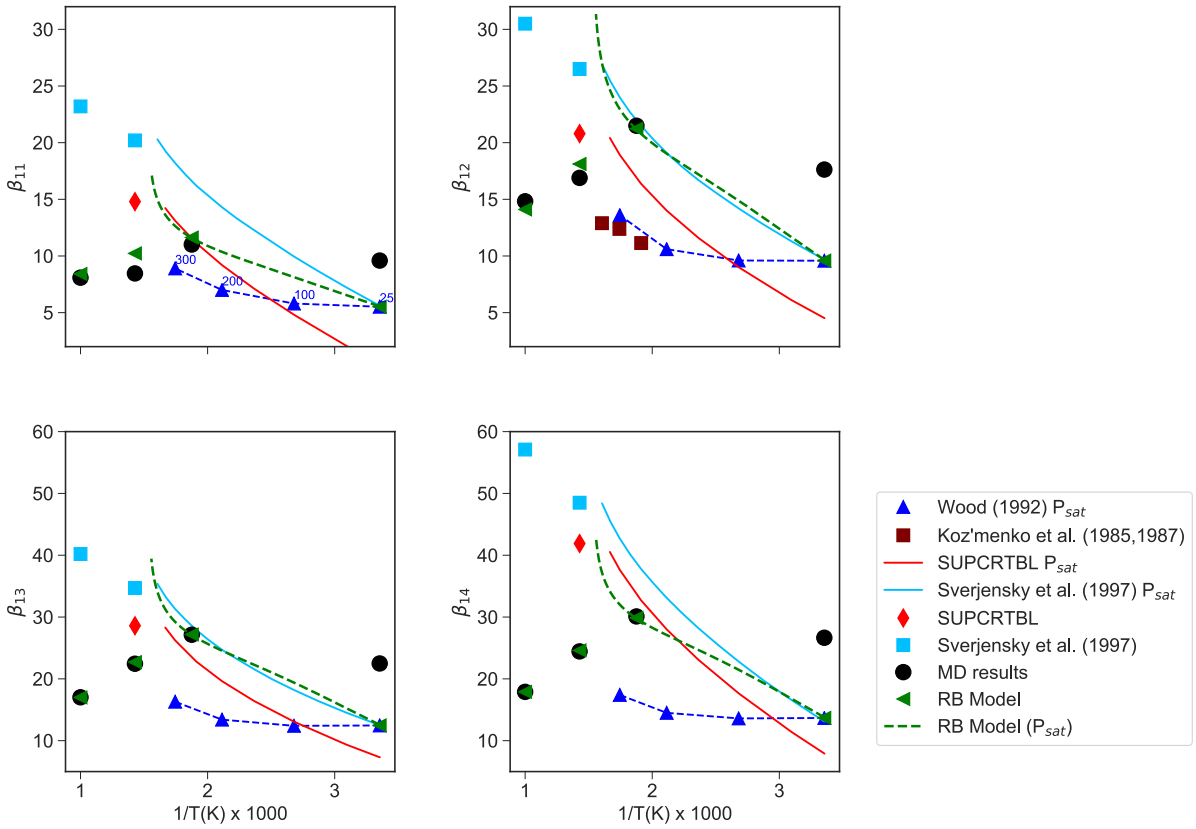

Figure 4.7: Plot of the logarithmic stability constant of this study derived from the AIMD simulations, interpolation using the Ryzheno-Bryzgalin (RB) model, thermodynamic data from Wood [1992] and results from SUPCTBL as well reported values from Sverjensky et al. [1997] as a function of the inverse temperature for a 1 molal standard solution. Additionally, the experimental data from Koz'menko et al. [1985, 1987] for $BeF_{2\,aq}$ are shown. The blue numbers in first plot provide guidance and refer to the temperature in °C.

---

et al., 2015] or to a trigonal coordination in S-rich fluids [Mei et al., 2016]. As discussed by Etschmann et al. [2019] leads this change in coordination to a stronger association and higher mobility of the metal ion as well as a higher solubility of sphalerite (ZnS). However, the coordination change observed in this study is not account in extrapolations of solvation energies measured at 25 °C based on the Born-model equation or simpler extrapolation models [Helgeson, 1967, 1969]. Therefore the Be^{+} solubility in hydrothermal solutions might be different as accept.

Moreover, it was possible to derive new thermodynamic data for the Be-F system. But this data set is to be considered as highly qualitatively and only might indicate further meanings. Firstly, beside the simplified fluid composition the formation of HF is avoided in the simulation

box. This constraint should not bias the results according to Ciccotti et al. [2005], Mei et al. [2016] but seems to have a strong effect on the resulting free energies. A possible explanation might be the change of the configuration space due to longer or shorter lifetime of the hydration environments around the F^- ion. Nerveless, the AIMD results indicate that BeF complexes are thermodynamically much stronger as predicted by Wood [1992]. This outcome is very interesting because this stability constants are mainly used for thermodynamic modeling of Be-ore deposits in the past and nowadays by different authors [Reyf, 2004, Damdinova and Reyf, 2008, Foley et al., 2012, Damdinova et al., 2019]. In order to prove this observation, additionally simulation im combination with other free energies sampling techniques are required.

This case study is not able to provide a general explanation for the beryllium transport and its concentration in geological fluids. There may be other suitable ligands for beryllium in nature fluids, which have to be considered in thermodynamic modeling, e.g. (BO_3^{3-}[Thomas et al., 2009] or more importantly CO_3^{2-}. As shown by Syromyatnikov et al. [1972], the addition of CO_2 increases strongly the solubility of Be silicate minerals. One the other side, the enthalpy of formation of Be^{2+} in aqueous fluids at elevated temperatures is required, which can only derived considering both sides of a dissolution reaction: the aqueous species and the solid. This quantity cannot be derived directly from the simulations presented here.

Chapter 5

CASE STUDY III: FORMATION OF HYDROFLUORIC ACID IN AQUEOUS SOLUTIONS UNDER HIGH TEMPERATURE AND HIGH PRESSURE

Essential components of geological aqueous fluids are halogens [Harlov and Aranovich, 2018]. They enable the solubility and transport of most metal cations. Especially fluorine increases the solubility of certain elements in aqueous fluids dramatically e.g Ti [Rapp et al., 2010], Zn [Duc-Tin et al., 2007], Al, Zr and Nb [Lecumberri-Sanchez et al., 2018] etc. The strong correlation between fluorine bearing phases and enrichment of metal in altered rocks [Barnes, 1979, Svensen et al., 2008] seems to underline the important role of fluorine in metasomatic processes. Therefore, it is assumed that fluorine is a powerful component in ore-forming systems as such Fe oxide Cu-U-Au-Ag (IOCG) deposits [McPhie et al., 2011, Montreuil et al., 2016, Chen and Zhou, 2014] or rare earth elements deposits [Williams-Jones et al., 2000, Xing et al., 2018]. But due to the low solubility of fluoride minerals such as fluorite (CaF_2) [Lecumberri-Sanchez et al., 2018] and the increasing association of fluoride with hydrogen to form hydrofluoric acid at high temperatures its role is questioned [Migdisov and Williams-Jones, 2014]. In contrast, at high pressures and high temperatures the CaF_2 solubility increases significantly [Tropper and Manning, 2007]. The essential role of fluorine for the mobility of trace and major elements in high grade metamorphism has been shown in numerous of studies (e.g Aranovich and Safonov [2018], Tropper et al. [2013], John et al. [2008], Pan and Fleet [1996]). Due to the invisibility of F to LA-ICP-MS[1] methods the fluorine concentration in aqueous geological fluid was only estimated by thermodynamic modeling [Aksyuk, 2000, Zhu and Sverjensky, 1991].

Fluorine in Geochemical Processes

The role of halogens in geochemical processes such as metamorphism, the evolution of ore deposits and volcanic systems has been investigated over decades (see Harlov and Aranovich [2018], Aiuppa et al. [2009] for an overview). Fluorine is the most abundant halogen in

[1] Laser Ablation Inductively Coupled Plasma Mass Spectrometry

Earth's crustal rocks (1040 ppm) [Wedepohl, 1995] and chlorine and fluorine are the most abundant volatile elements in the deep Earth [Beyer et al., 2012]. Both elements have significant differences in their geochemical behavior in terms of fractionation properties. Halogens in general preferentially fractionate in to the aqueous phase compared to melts or minerals (under increased P/T e.g. volcanic processes [Bureau et al., 2000]). But fluorine is an exception as it preferably partitioned into solid phases or melts (Munoz [1984], Bureau et al. [2000], Dalou et al. [2015], Aranovich and Safonov [2018]). For this reason the chlorine and fluorine cycles are decoupled [Straub and Layne, 2003, Barnes et al., 2018] and F appears to be returned to the deep mantle. But Brenan [1993] shows in hydrothermal partition experiments between brines and apatite that with increasing pressure there is a speciation contribution of fluoride in the aqueous fluid that lowers the fluorine incorporation in the apatite structure.

The main fluoride species (under hydrothermal condition and during volcanic degassing) are presumed to be NaF_{aq}, CaF^{+} and especially HF_{aq} [Weber et al., 2000, Richardson and Holland, 1979, Zhu and Sverjensky, 1991, Symonds et al., 1994]. The existence of HF_{aq} is constrained by the availability of H^{+} ions in the fluid, the dielectric constant (ϵ) of the solvent [Sverjensky, 2019] and the dissociation reaction:

$$HF_{aq} + H_2O \rightleftharpoons F^{-} + H_3O^{+} \tag{5.1}$$

The equilibrium of this reaction controls the activity of F^{-} and therefore the capacity to form metal-fluoride aqueous complexes. This equilibrium is quantified by the pK_a value referred to as the acid dissociation constant or acidity constants. pK_a ($-\log K_a$) is a fundamental property of acids and indicates their reactivity. The acidity constants of hydrofluoric acid in aqueous solution at ambient condition is well investigated and given by Hefter [1984] with pK_a=3.18. Therefore, HF_{aq} is assigned to the group of weak acids [Pauling, 1956] because it is mainly associated in aqueous solutions under room temperature conditions unlike all other acids of the halogens series. It is widely accepted that F^{-} strengthens the water network, reduce the configurational entropy and therefore it is energetically unfavorable at room conditions in solution [Elena et al., 2013, Ayotte et al., 2005, Myers, 1976].

Due to experimental difficulties to control P/T, composition and quantitative resolution of *in situ* spectroscopy experiments it is very challenging or even impossible to gain thermodynamic or structural properties of solutes (see for further details Sanchez-Valle [2013], Brugger et al.

[2016]) at condition of the Earth's crust or upper mantle and solution composition equivalent to those in nature. Especially hydrofluoric acid as a highly toxic substance is difficult to study. Nevertheless, pK_a values of HF_{aq} have been measured up to 200-300 °C and water vapor pressure ($P_v \equiv P_{sat}$) using cell potentials and conductivity measurements [Ellis, 1963, Ryzhenko, 1965, Richardson and Holland, 1979]. All these data sets are in good agreement to each other. Further, Barnes et al. [1966] reported dissociation constants based on experiments by Franck [1961] up to supercritical water conditions.

Hydrofluoric acid is an essential substance in chemical laboratories. For this reason the behavior of fluoride in H_2O respectively D_2O on a molecular scale has been intensively studied with focus on higher polymerized HF species (e.g. FH-F and FH-FH, HF_2^-) at ambient conditions (e.g. Simon and Klein [2005], Joutsuka and Ando [2011]). As shown by Laasonen et al. [2006] first principles molecular dynamics simulations are capable to reproduce experimental IR spectra as well the hydration properties of fluoride. But to my knowledge there is no study focusing the behavior of HF under extreme P/T conditions in aqueous solutions as they occur in Earth's crust and upper mantle [Keppler, 2017].

Aim of this Case Study

The aim of this case study is to understand the complexation proprieties of fluoride respectively hydrofluoric acid in aqueous environments at extreme P/T conditions from *ab initio* molecular dynamics simulations. Another goal is to gain new insight in the role of aqueous fluids during fractionation processes between melt and fluids. *Ab initio* well-tempered metadynamics (WTMetaD) simulations are performed using the *PLUMED 1.3.0* code [Bonomi et al., 2009] within in the *CPMD* code (v3.15.1) [CPMD, 1990, Marx and Hutter, 2000] to compute the free energy change during HF_{aq} dissociation.

5.1 Computation and Thermodynamic Approach

To separate the electronic and nuclear motion in the presented AIMD simulation a fictive electron mass of 600 a.u, a fictive kinetic energy of 0.12 a.u. and a time step of 0.1 fs was chosen. Simulations with numerous box sizes were performed along two different isotherms: at 327 °C and 727 °C plus one simulation at ambient conditions (see Tab. 5.1). The pressure

conditions in the simulation cell were estimated by the equation of state (EOS) reported by Zhang and Duan [2005] of pure water. One of the chosen system densities in Tab. 5.1 at 327 °C is not within the range of the EOS. Here the formalism by Wagner and Pruß [2002] was used to estimate the pressure conditions as well for a system temperature of 25 °C (see Tab. 5.1). The initial atomic configurations were obtained from a previous AIMD study by Jahn and Wunder [2009] at temperatures of 727 °C to reduce the computation coasts that would be required for the equilibration of a completed new solvent structure. The simulation cell of Jahn and Wunder [2009] contain 64 water molecules, one lithium (Li^+) ion and one fluoride (F^-). After the substitution of Li for a hydrogen ion (H^+) a re-equilibration runs was performed for 3-4 ps. The 327 °C were reached by a stepwise cooling of 100 °C per 500 fs followed also by 3-4 ps equilibration run. All unbiased production simulations run for 20 ps.

Proton transfer reactions are a key process in dissolution and precipitation of matter in aqueous solutions. The general reaction:

$$HA + H_2O \rightleftharpoons A^- + H_3O^+ \tag{5.2}$$

where HA is an acid and A^- a base. The equilibrium of this equation is defined by the acidity constant (pK_a):

$$pK_a = -\log K_a = \frac{\Delta G_r^\circ}{2.303\ RT} \tag{5.3}$$

This value depend on the ideal gas constant R, the temperature T and $\Delta_r G^\circ$ the standard Gibbs free energy of the reaction 5.2. Using the metadynamics (MetaD) approach (for further explanations see section 2.4) it is possible to probe the free energy surface of a reaction pathway [Barducci et al., 2011] and to compute the pK_a using Car-Parrinello molecular dynamics (e.g. see Pérez de Alba Ortíz et al. [2018]).

For the applied well-tempered metadynamics (WTmetaD) simulation the width of the Gaussians was set to σ=0.1 and the initial height was optimized together with the deposition rate of the hills. A too fast deposition rate of the hills results in an unsymmetrical filling of the underlying bias potential and in a inaccurate reconstruction of the free energy difference between the different states of the system. An initial height of 1.312 kJ/mol (0.0005 a.u.) is used, comparable to studies by Sakti et al. [2018] and Tummanapelli and Vasudevan [2014], and a deposition rate of 200 steps between the hills gives a good compromise between efficiency and

Table 5.1: Densities of the simulation cell at 727 °C and 327 °C with their estimated pressure from the EOS by Zhang and Duan [2005]. The value marked with † are computed using the formulation of the IAPWS[1] [Wagner and Pruß, 2002].

727 °C		
Box edge length (Å)	Density (kg/m^3)	Pressure (MPa)
10.85	1526	8377
11.11	1419	6119
11.64	1234	3377
12.17	1080	1957
12.70	951	1198
13.23	841	777
13.76	748	536
14.82	599	302
15.88	487	205
327 °C		
Box edge length (Å)	Density (kg/m^3)	Pressure (MPa)
11.11	1419	4269
11.64	1234	2046
12.17	1080	948
12.70	951	417
13.23	841	168
13.76	748	60 †
14.29	668	18 †
14.82	599	12 †[2]
25 °C		
Box edge length (Å)	Density (kg/m^3)	Pressure (MPa)
12.50	998	0.1†

[1] The International Association for the Properties of Water and Steam
[2] Extrapolation to lower pressures as they occur on the water vapor pressure curve

accuracy of the WTMetaD simulation at high temperature and high pressure. For the simulation at ambient condition the deposition rate was doubled due to the slower dynamics of the system.

The CV must be chosen in a way, that it provides a coarse-grained description of the whole reaction. In the present case, the coordination number was used to derive the dissociation free energy of HF_{aq}. For this purpose the bonding of fluorine by hydrogen has to be described by a differentiable function. This function must enable the distinction of the associated and

dissociated states of reaction 5.1. This is achieved in general by:

$$s = \sum_{i \in G_1} \sum_{j \in G_2} s_{ij} \tag{5.4}$$

the sum over all pairs of atoms within group G_1 (F) and group G_2 (all H). A switch function is applied that describes individual contributions to s_{ij} by every group member of G_2 within a certain distance:

$$s_{ij} = \begin{cases} 1 & \text{for } r_{ij} \leq 0 \\ \frac{1-(\frac{r_{ij}}{r_0})^n}{1-(\frac{r_{ij}}{r_0})^m} & \text{for } r_{ij} \geq 0 \end{cases} \tag{5.5}$$

where $r_{ij} = |r_i - r_j| - d$.

The first graph in Fig. 5.1 shows s_{ij} using the parameters d=0.5 Å, r_0=0.8 Å, n=12 and m=24. This switch function s_{ij} takes its maximum value of one when the hydrogen reaches the intramolecular HF_{aq} distance and decrease sharply from there to smaller values at a distance of the hydration shell around the fluorine species. In the central graph of Fig. 5.1 the evolution of the intramolecular F-H coordination (≡CV) represented by s_{ij} is shown and on the right site snapshots of different atomic configurations that are presented. There are three different states that can be distinguished by the function s_{ij}. Config. 1 illustrates the dissociation state at lower CV values where fluoride is hydrated by H_2O and H_3O^+ is located in the 1st or 2nd hydration shells. The association state (config. 3) the hydrofluoric acid is only coordinated by H_2O. Due to the interaction of fluorine species with more than one hydrogen the CV can reach value CV>1 when a further hydrogen gets close to the acid molecule. Between these two states a transition state can be found where $[FH_3O(H_2O)_2]_{aq}$ is formed and the hydrogen is shared between the halogen and the oxonium ion.

To evaluate the change of the coordination number as function of time the *driver* utility provided with *PLUMED 2.4.3* [Tribello et al., 2014] is used. Here, the coordination number is computed applying the same type of switch function (Eq. 5.5) with different r_0 values to encounter the separation of the different coordination shells.

A density model is applied (see chapter 2.1) to inter- and extrapolate the derived pK_avalue to unexplored steps of dissociation. Further thermodynamic modeling is conducted with the DEW code [Sverjensky et al., 2014] using HKF parameters reported by Shock et al. [1989].

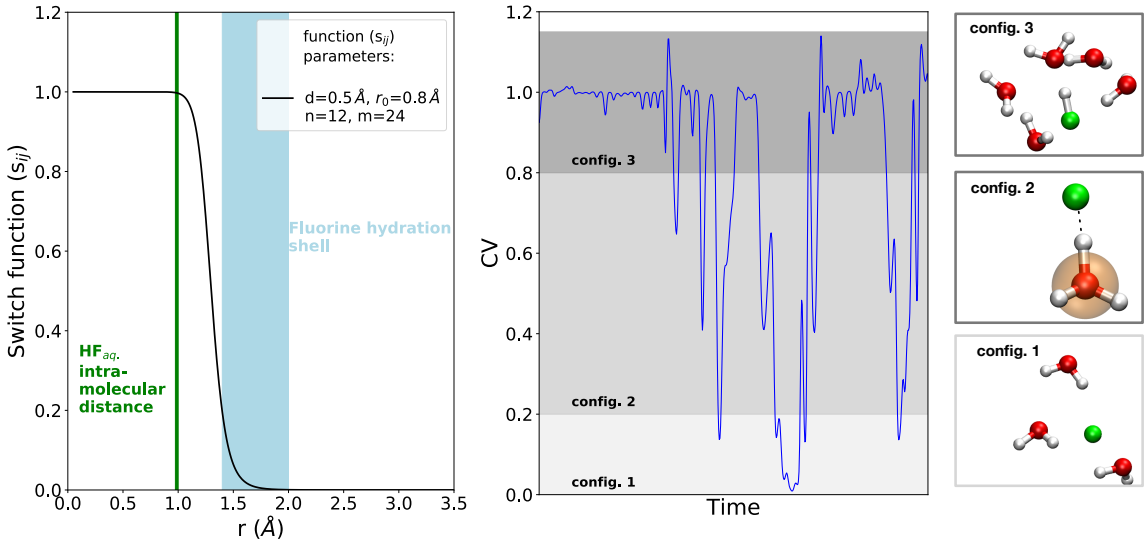

Figure 5.1: The left graph shows the applied switch function (Equation 5.5) that is used to define the CV during the WTMetaD simulation. In the middle graph an exemplary evolution of the CV over time at high temperatures is shown. Graphs on the right hand site show different atomic fluorine species configurations (config.) that can be distinguished by s_{ij}.

The outcome of this modeling refers to the standard state of the solute. The F concentration in the simulation cell is close to one (~0.9 molal). But as shown by Tummanapelli and Vasudevan [2014] an increasing number of water molecules in the system does not effect the free energies surface (FES) of a proton transfer reaction. Only if the number of water molecules in the simulation volume is too low to fully hydrate the dissolve ion (blow 30-40 H_2O) the FES is effected. The number of water molecules in the used simulation box is higher and therefore no further concentration correction is applied to the computed reaction free energies reported in the following and infinite dilute properties are assumed. Beside the WTmetaD approach, thermodynamic integration in combination with constraint AIMD was applied to the system (as used in chapter 3,4) . Here the atomic distance between the fluoride and the initially bonded hydrogen was constrained within a distance range of 1.0 Å to 3.0 Å. For each integration step the system was equilibrated for 0.2-0.5 ps followed by a production run of 6-9 ps. The error of the free energy change is estimated by the standard deviation of the constraint force between 2 Å and 3 Å. Within this distance the initially bonded hydrogen is considered to be dissociated from the fluorine.

5.2 Results

Local Fluorine Species Environment

For both temperatures the coordination environment of fluorine in the aqueous solution is changing with compression. In $g_{FH}(r)$ three main fluorine hydrogen bond distances can be distinguished (see Fig. 5.2). The intramolecular F-H distance of ~1 Å does not change significantly with pressure. But the height of this first peak in Fig. 5.2 and therefore the F-H coordination decreases with increasing compression (see listed values in Tab. 5.2 and Fig 5.3a).

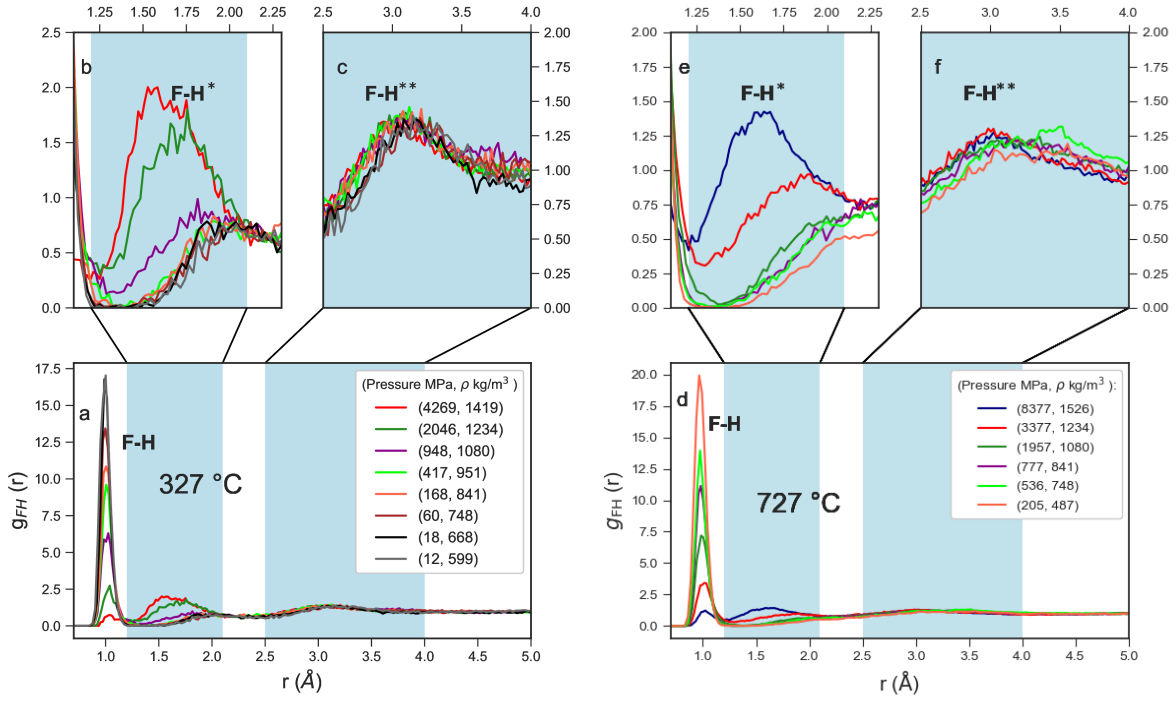

Figure 5.2: The $g_{FH}(r)$ for T=327 °C and T=727 °C and different pressure/density conditions. (b-f) are magnifications of the second and third maximum of the distribution functions.

Self-association and -dissociation within the simulation time can be observed at higher pressure conditions (see Tab. 5.2) . For T=327°C the intramolecular coordination of fluorine starts to reduce from 1.0 between 12-417 MPa to 0.2 at 4269 MPa. At 727°C a constant coordination of one up to a pressure of 1957 MPa can be observed. Above that the F-H coordination decreases to 0.3 at 8377 MPa in conjunction with the formation of H_3O^+.

The height of the second peak (F-H*) in Fig. 5.2 a,d increases with the decrease of the first intramolecular H-F peak. This second peak can be assigned to the water molecules in the

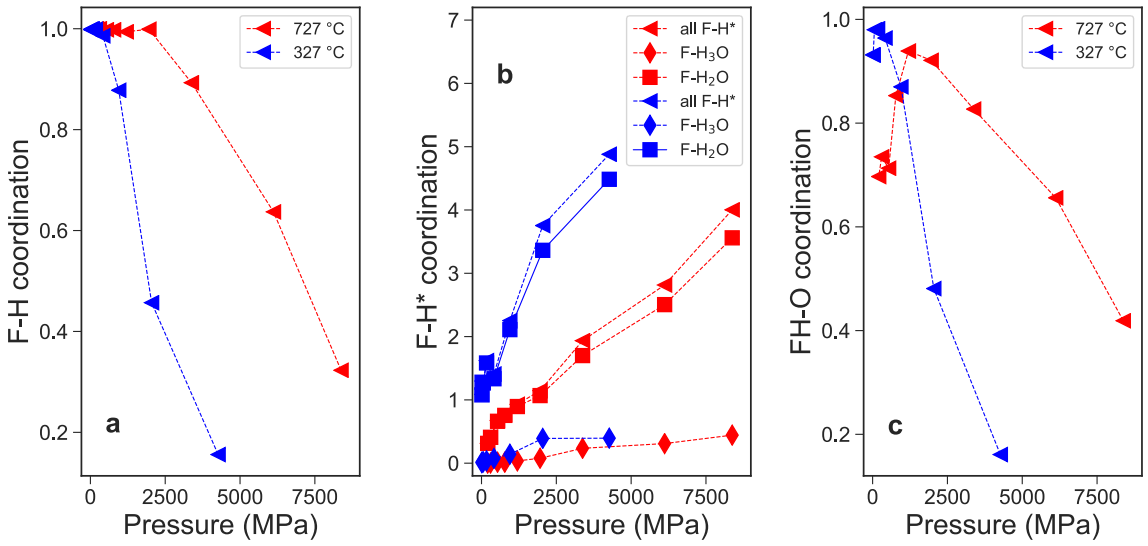

Figure 5.3: (a) shows the change of the intramolecular F-H coordination with changing pressure in the solution. (b) the coordination of fluorine by hydrogen as a function of pressure where the coordination of fluorine by H_2O and H_3O^+ is additional spited up. The color coding is the same as in the graph left and right. (c) show the average number of water molecules coordinating the hydrogen of the associated acid.

---

intramolecular H-F peak. This second peak can be assigned to the water molecules in the first hydration shell around the halogen species. This becomes more visible in the pressure range of 8377-3377 MPa at 727 °C and at 4269 to 2046 MPa at 327 °C. At both temperatures this distances decrease with increasing pressure (Fig. 5.4 a). At 727 °C and 327 °C a minimum value of ~1.6 Å at the maximum pressure can be found. In contrast, a significant difference in the F-H* distance between low and high temperatures is observed at lower pressures. At 727 °C/205 MPa the F-H* distance reaches its maximum at 2.40 Å whereas at 327 °C a F-H* distance of ~2.0 Å is reached between 12-168 MPa. Generally, the largest changes occur at pressures above ~900 MPa (Fig 5.4).

For both temperatures the number of hydrating H_2O molecules around the fluorine species increases with increasing compression (Fig 5.3 b). In particular, at pressures above $P_{727°C}$= ~2500 MPa and $P_{327°C}$=~1000 MPa a rapid increase of the F^- hydration up to 4-5 water molecules is observed. In general a faster increase of the F-H* coordination, comparing both T conditions, can be found for T=327 °C than for T=727 °C. Two snapshots of the two atomic end member configuration for the high temperature runs are shown in Fig. 5.5.

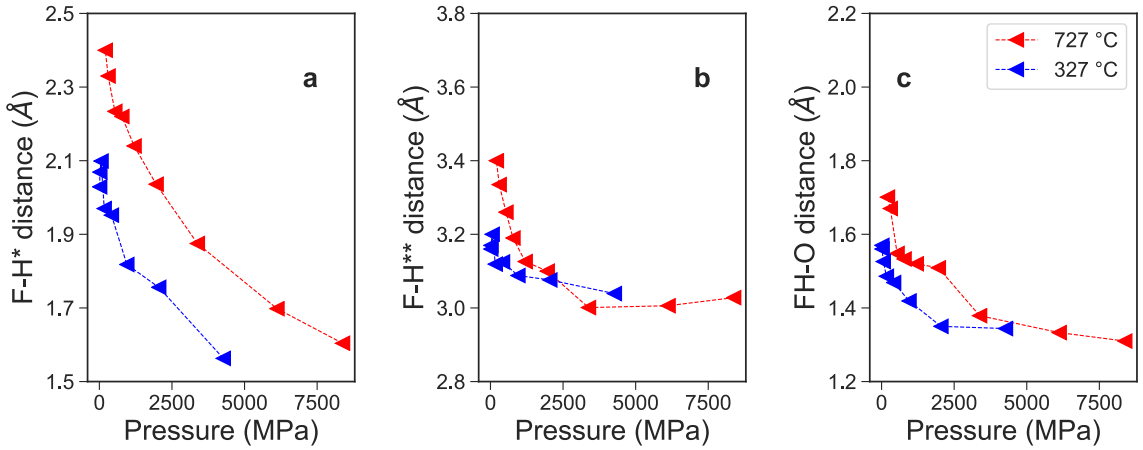

Figure 5.4: Evolution of the atomic distances as a function of pressure. (a) between the hydrogen close to the fluorine. (b) hydrogen at the side of oxygen which faces away from the fluorine. (c) distance between the hydrogen of the acid molecule and the closed oxygen.

The third maximum (F-H**) in Fig. 5.2 c,f represents the fluorine hydrogen distance of those hydrogens of H_2O and H_3O^+ that face away from the fluorine. The change of this distance as function of pressure is shown in Fig. 5.4 b. It should be underlined that the F-H** peak shape in Fig 5.2 at low P is broad and flat and therefore not well defined. Nevertheless, the differences between both temperature conditions vanish with increasing compression. Therefore, at P>1000 MPa rather equivalent F-H** distances can be found. Only at lower pressures significance higher F-H** distances up to 3.40 Å (727 °C) compared to 3.16 (327 °C) occur. While the distance between the hydrogen of the acid molecule to hydrating H_2O and the number of hydrating water molecules decrease with increasing pressure (see Fig. 5.4c and Fig. 5.3 c). The number of hydrating water molecules decreases as well toward lower pressure at least in the high temperature runs. But in average the FH-OH_2 coordination does not exceed one molecule.

Looking at the hydration changes of F^- and HF_{aq} at equal density in Fig 5.6 over time, certain similarities and differences can be seen between both conditions. Whereas, at 327 °C F^- is coordinated by 4-6 water molecules the coordination drop to 3-4 hydrating H_2O at 727 °C over time. In contrast, the fluorine in the acid molecule is coordinated by two or three molecules at lower temperatures and by one up to two at higher temperatures. However, during the transition state were the proton transfer happens the fluoride is coordinated by three H_2O in total, where two of the water molecules are orientated towards the halogen and one toward the hydrogen

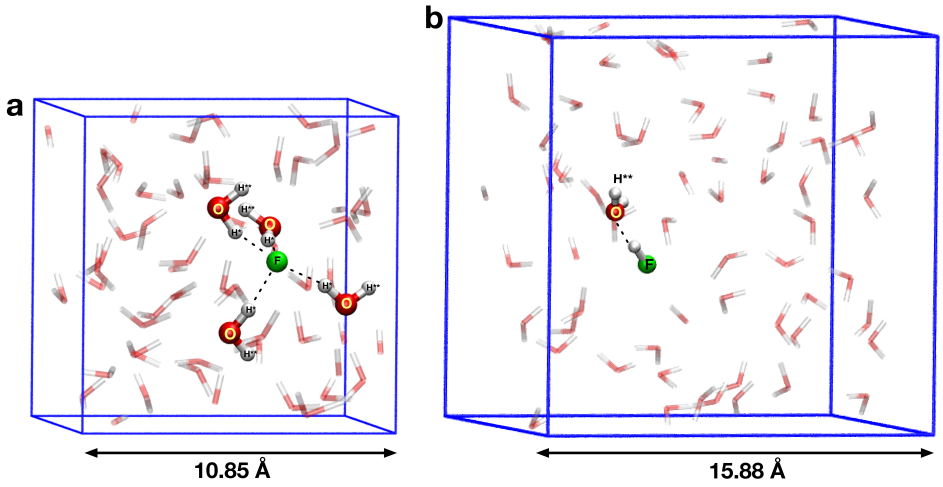

Figure 5.5: (a) shows a snapshot of the main coordination of fluorine at 727 °C and 8377 MPa. The blue cube represents the simulation box, the transparent with-red sticks are the hydrogen and oxygen atoms outside the first hydration shell of the green fluorine. The hydrating H_2O are drawn as white and red balls. The black labels (H*,H**) refer to the peak position in the radial distribution function $g_{HF}(r)$ in Fig 5.2. (b) illustrate the system at low pressure and density conditions (205 MPa / 487 kg/m^3) and 727 °C. Here, the acid is strongly associated and a single hydrating H_2O is many bonded to the hydrogen of the acid.

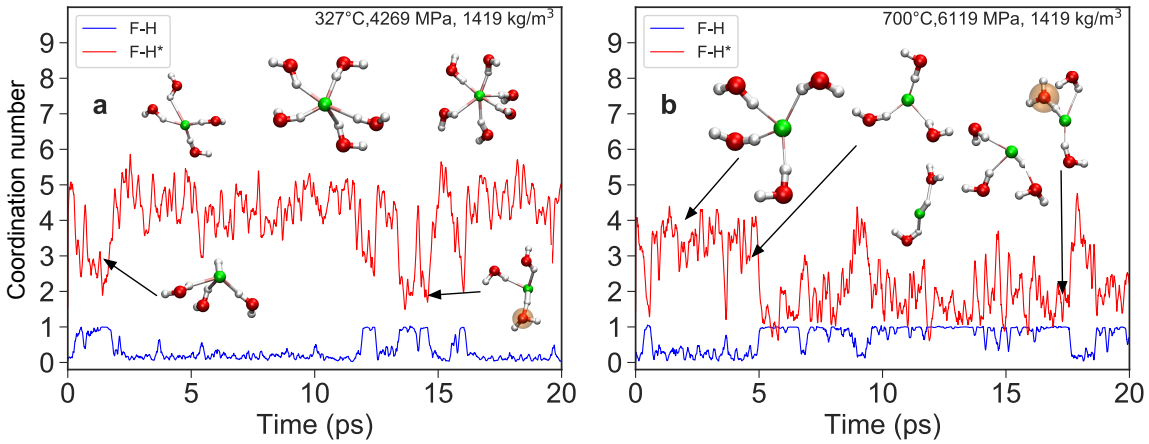

Figure 5.6: (a,b) Evolution of the F-H and F-H* coordination for both temperatures at equal densities over the simulation time.

(see Fig. 5.6). This transition configuration can be found in all unbiased simulations where the proton is exchanged between the halogen and H_3O^+.

Table 5.2: List of atomic distances and coordination numbers averaged over the whole simulation time.

Conditions		Distances (Å)			Coordination numbers				
727 °C									
Density (kg/m^3)	Pressure (MPa)	F-H*	F-H**	FH-OH_2	F-H	F-H*	F-H_2O	F-H_3O	FH-O
1526	8377	1.60	3.03	1.31	0.3	4.0	3.6	0.4	0.4
1419	6119	1.70	3.01	1.33	0.6	2.5	2.2	0.3	0.7
1234	3377	1.88	3.00	1.38	0.9	1.9	1.7	0.2	0.8
1080	1957	2.04	3.10	1.51	1.0	1.1	1.1	0.0	0.9
951	1198	2.14	3.13	1.52	1.0	0.9	0.9	0.0	0.9
841	777	2.22	3.19	1.53	1.0	0.8	0.8	0.0	0.9
748	536	2.23	3.26	1.55	1.0	0.7	0.7	0.0	0.7
599	302	2.33	3.34	1.67	1.0	0.4	0.4	0.0	0.7
487	205	2.40	3.40	1.70	1.0	0.3	0.3	0.0	0.7
327 °C									
1419	4269	1.56	3.04	1.34	0.2	4.8	4.5	0.3	0.2
1234	2046	1.76	3.08	1.35	0.5	3.5	3.1	0.4	0.5
1080	948	1.82	3.09	1.42	0.9	2.3	2.2	0.1	0.9
951	417	1.95	3.13	1.47	1.0	1.4	1.3	0.1	1.0
841	168	1.97	3.12	1.49	1.0	1.6	1.6	0.0	1.0
748	60	2.10	3.20	1.53	1.0	1.3	1.3	0.0	1.0
668	18	2.07	3.17	1.56	1.0	1.3	1.3	0.0	0.9
599	12	2.03	3.16	1.57	1.0	1.1	1.1	0.0	0.9
25 °C									
998	0.1	1.80	3.05	1.42	1.0	2.2	2.2	0.0	1.0

Free Energy Exploration

In the unbiased AIMD runs the dissociation of the initial acid molecule can only be observed at high compression of the aqueous system. Therefore, no further investigations can be made for the pure fluoride at lower pressure conditions. To enable the analysis and probing the FES of the aqueous dissociation reaction of hydrofluoric acid WTMetaD are carried out. Further, constraint AIMD simulations as applied in previous chapters were used as benchmark method. The main results of the WTMetaD simulations are listed in Tab. 5.3.

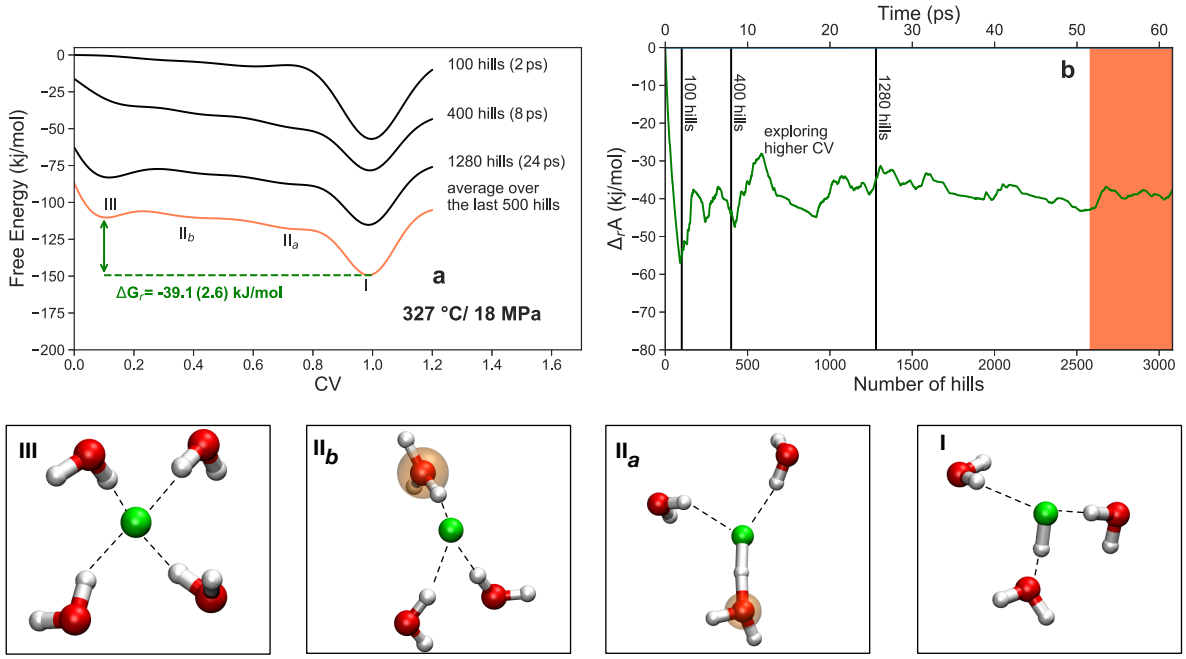

Figure 5.7: (a) the FES after 100, 400, 1280 hills were added to the system. The light red profile represents the average over the last 500 hills of the WTMetaD run at T=327 °C and P=18 MPa. (I) and (III) illustrated atomic configurations corresponding to the collective variable value of the dissociated and associated state during the reaction. (II$_a$) shows the transition state where the proton transfer between the fluoride and the oxonium ion take place. (II$_b$) the oxonium ion is closely located to the fluorine. (b) shows the evolution of the free energy difference between (I) and (III) with increasing number of hills.

Table 5.3: WTMetaD simulation conditions and the computed reaction Helmholtz free energies ($\Delta_r A$) with the derived acidity constants (pK_a) of hydrofluoric acid . Further listed are the observed coordination numbers of $HF_{aq.}$ and F^- in respect to H_2O and H_3O^+ . Additionally, pK_a^{DEW} value derived from the Deep Earth Water (DEW) code [Sverjensky et al., 2014] applying HKF parameter from [Shock et al., 1989] and experimental (Exp.) results by Hefter [1984] are added.

727°							
Density (kg/m^3)	Pressure (MPa)	Time (ps)	$\Delta_r A$ (kJ/mol)	pK_a	pK_a^{DEW}	CN_{F^-}	$CN_{HF_{aq}}$
1526	8377	112	10.4 (1.2)	-0.5 (0.1)	0.5	4.7	3.9
1234	3377	80	-15.8 (3.1)	0.8 (0.3)	3.9	3.9	3.0
1080	1957	120	-17.8 (2.2)	0.9 (0.2)	5.1	3.5	2.6
951	1198	88	-33.0 (5.1)	1.7 (0.4)	6.0	3.1	2.4
841	777	135	-46.0 (1.3)	2.4 (0.1)	6.7	2.9	2.2
748	536	80	-54.1 (2.1)	2.8 (0.2)	7.4	2.7	2.0
599	302	88	-70.6 (3.1)	3.7 (0.3)	8.2	2.4	1.7
487	205	65	-79.0 (5.9)	4.1 (0.5)	9.0	2.3	1.5
327°							
1419	4269	130	12.9 (1.6)	-1.1 (0.1)	0.1	5.2	4.2
1234	2046	150	0.3 (1.4)	0.0 (0.2)	2.5	4.7	3.7
1080	948	120	-7.0 (2.2)	0.6 (0.1)	3.9	4.4	3.4
951	417	40	-15.7 (1.1)	1.4 (0.2)	4.9	4.0	3.0
841	168	55	-23.6 (2.4)	2.1 (0.2)	5.5	4.0	3.0
748	60	62	-32.8 (2.8)	2.9 (0.2)	6.0	3.8	2.8
668	18	64	-39.1 (2.6)	3.4 (0.2)	6.5	3.7	2.7
25°							
Density (kg/m^3)	Pressure (MPa)	Time (ps)	$\Delta_r A$ (kJ/mol)	pK_a	Exp.	CN_{F^-}	$CN_{HF_{aq}}$
998	0.1	51	13.4(0.7)	2.4(0.1)	3.18(0.2)	4.6	3.5

The computed FES in the investigated P/T range are characterized by two main minima (I,III) in the CV space (see Fig 5.7), that correspondents to CV≈0.09 and CV≈0.95 and represent the dissociated and associated state of reaction 5.1. Fig. 5.7a shows exemplary the development of a FES with increasing number of deposited hills for T=327 °C and P=18 MPa. After adding the first hundred hills (2 ps) the system is enabled to leave the first minimum and to overcome the energy barrier that separates the two states (Fig. 5.7a). Between the metadynamics step 400 and 1280 the profile of FES reached its final shape and the height of the hills is significantly lower (Fig 5.8b). The convergence of $\Delta_r A$ is estimated by the change of the free energy difference between the two minima as a function of metadynamics step in Fig. 5.7 b. The final energy difference of $\Delta_r A$=-39.1(2.6) kJ/mol is computed by averaging over the last 500 hills of the WTMetaD. To estimate the error in $\Delta_r G$ the double standard deviation (2σ) of the free energy over the last 500 hills is calculated for every WTMetaD simulation.

Beside I and III further smaller local minima in the FES can be observed around 0.3 and 0.7. They represent the transition state of the reaction (Fig.5.7 II_a,II_b), where the transition species $[FH_3O(H_2O)_2]_{aq}$ is formed and the oxonium ion closely located to the fluoride. In II_a the excess proton is shared between the fluoride and the oxonium ion. During the transition the fluoride is additionally hydrated by two water molecules. Due to the applied rather sharp switch function (see Fig.5.1) two positions characterize the transition state in the CV space: one where H is closer to the halogen and one where it is closer to the oxygen. Additionally higher coordination numbers are reached by the system, where HF_{aq} is formed and one or two hydrogen of H_2O have a distance to the fluoride small than the cut-off radius of the switch function. This leads to a strong hysteresis in CV space (Fig.5.8a). Furthermore, as marked in Fig. 5.7 is the convergence of $\Delta_r A$ effected by exploration of higher F-H coordination numbers. But hysteresis even occurs after rather long AIMD time as shown in Fig. 5.8a and can be seen in all WTmetaD simulations. Here, the CV does not diffuse freely between the minima and get stucked for significant time period of several hundred femtoseconds.

As in the unbiased AIMD runs a change of hydration of the fluorine species between I and III can be seen. For instance in Fig. 5.7 the hydrated F^- is coordinated by four molecules (H_2O and H_3O^+) whereas HF_{aq} only aggregated three H_2O molecules. But it must be emphasized that after the separation of the hydrogen from the fluoride the formed H_3O^+ is located in the first or

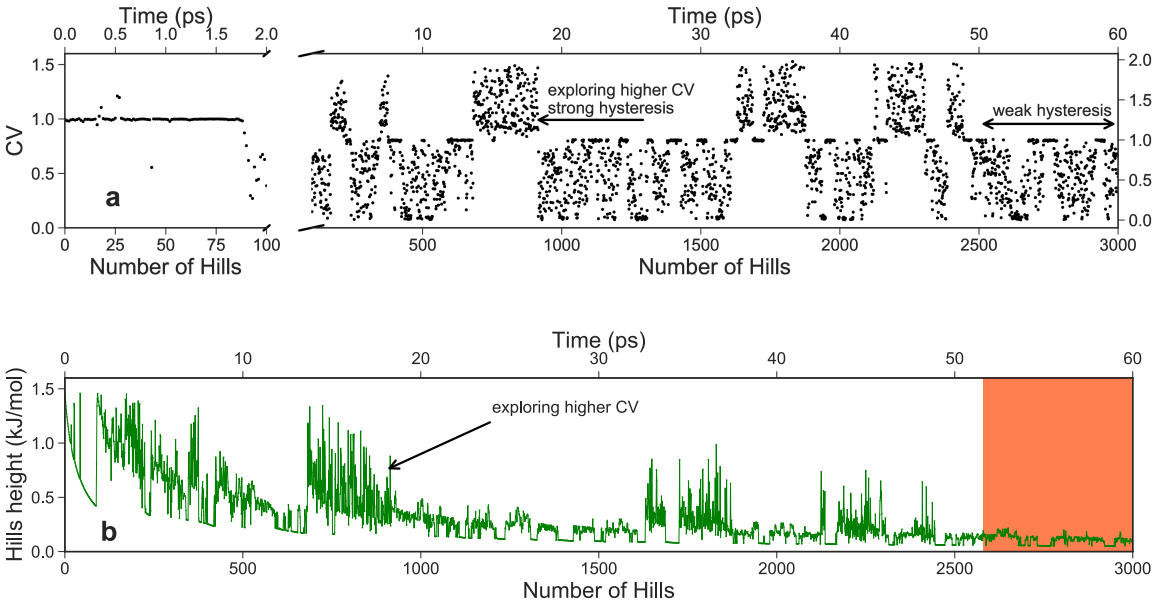

Figure 5.8: (a) time series of the collective variable CV (fluorine coordination). (b) height of deposited Gaussians (hills) as a function of time. Both graphs are derived from the WTmetaD run at 327 °C and 18 MPa.

---

second hydration shell of the fluoride. Only in the high density runs between 1526-1234 kg/m^3 the oxonium ion can be found at higher distance apart from F^-.

In Fig. 5.9 a the coordination change of the fluorine species with increasing pressure is shown. The number of coordinating molecules around F^- and HF_{aq} increase (values are listed in Tab. 5.3) with increasing compression. While F^- aggregated 2-5 molecules in its first hydration shell the acid incorporates between 1-4 H_2O. It has to be noted, that the coordination difference between both environments is approximately constant at one water molecule over the P/T range (see insert in Fig. 5.9a). Comparing the coordination numbers between both temperature conditions as a function of the fluid density in Fig. 5.9 b it appears that the hydration number is decreasing rather equally by one between 327 °C and 727 °C. A characteristic feature of all bias simulations is the occurrence of the transition species $[FH_3O(H_2O)_2]_{aq}$.

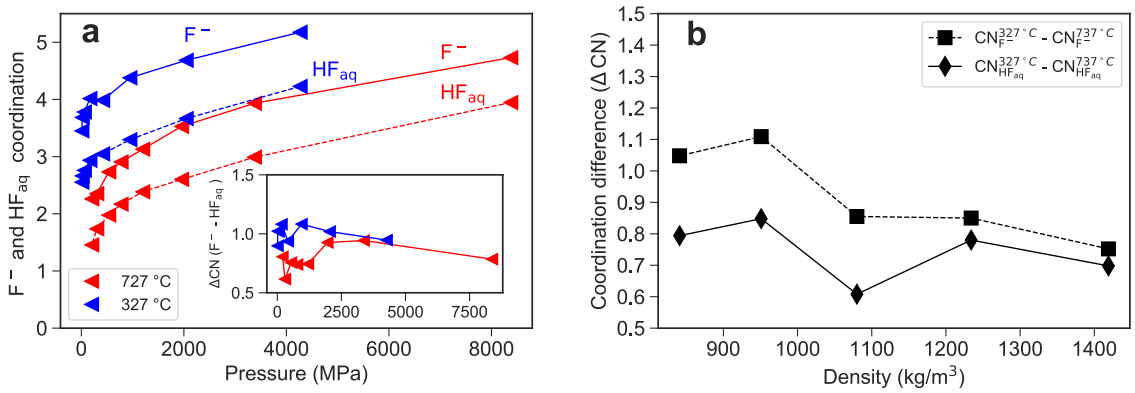

Figure 5.9: (a) change of the F^- and HF_{aq} coordination with respect to H_2O and H_3O^+ as function of pressure in the WTMetaD runs. Inset: difference of the coordination between the hydrated fluoride ion and the acid molecule. (b) difference of the fluorine species coordination number between both conditions.

For checking consistency constraint AIMD simulations in conjunction with thermodynamic integration are performed for certain P/T conditions. In Fig 5.10 I the PMF of the dissociation reaction at T=327 °C and P=18 MPa is shown and the evolution of $\Delta_r A$ with increasing F-H distance. Different stages of the dissociation are identified and shown in Fig 5.10 A-C. In the first stage the acid molecule exists and is coordinated by three water molecules it total. Here the highest attractive force is observed. In the next stage HF_{aq} is dissociated and the coordination number of the fluorine increases by one. Furthermore, the constraint force becomes more repulsive. An intermediate stage (Fig 5.10 C) appears at a constraint F-H distance of 1.6 Å. While the coordination of the fluorine ion decrease again by one the fluoride starts to associated with an unconstrained hydrogen of the coordinating H_3O^+. In last stage in Fig 5.10 D the constraint force is nearly vanished and the fluorine is associated with an unconstrained hydrogen. The integration of the PMF yield a $\Delta_r A_{\mathrm{TI}}$ of -41.4 (2.6) kJ/mol for the dissociation of HF_{aq}. Additional TI were performed: $\Delta_r A_{\mathrm{TI}}$(T=327 °C,P=4269 MPa)= 11.0 (3.6) kJ/mol and $\Delta_r A_{\mathrm{TI}}$(T=727 °C,P=205 MPa)= -75.5 (6.6) kJ/mol

Fig.5.11a shows the change in $\Delta_r A$ vs. log ρ_{H_2O} derived from both sampling approaches. A linear decrease of the Helmholtz free energy as a function of the logarithmic water density is observed. Moreover, both sampling approaches provide comparable dissociation energies. At a high solvent density the $\Delta_r A$ are converging for both temperature conditions whereas with less compression they diverge from a parallel behavior. At densities of 1234 kg/m^3 (327 °C) and

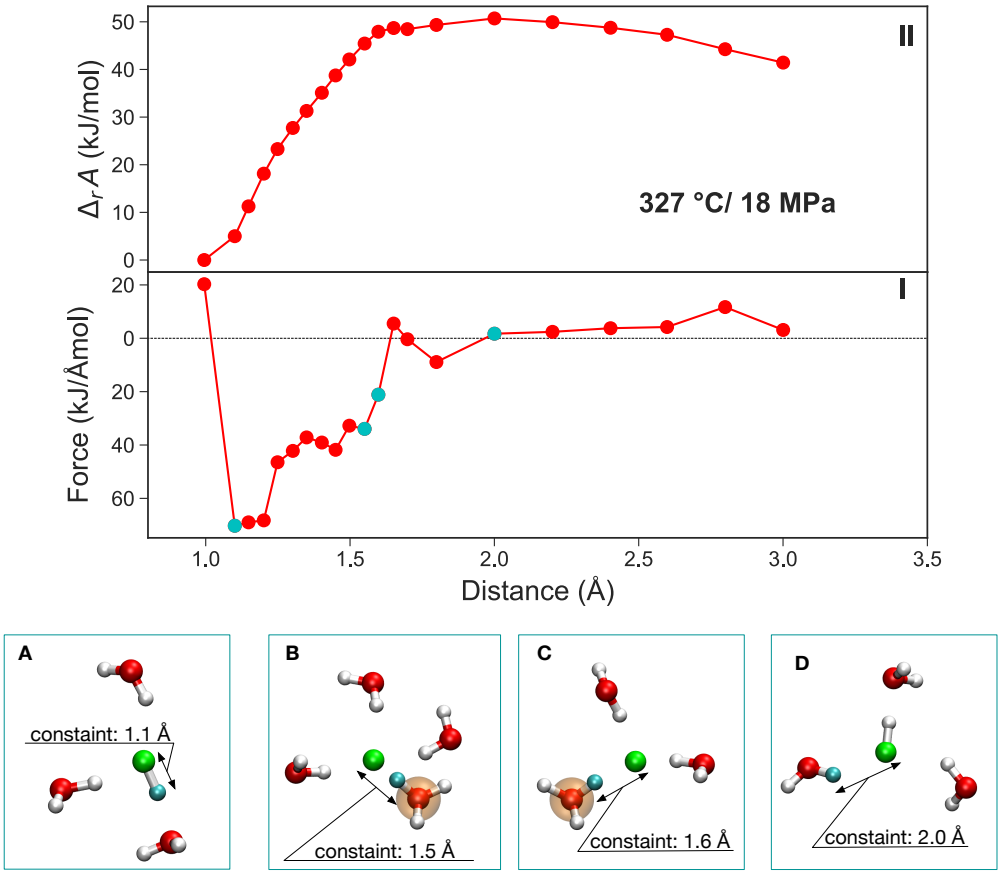

Figure 5.10: (I) Potential of mean force of the dissociation of HF_{aq} at 327°C and 18 MPa. (II) cumulative integration of the potential of mean force to determine the change in Helmholtz free energy $\Delta_r A$. (A-D) Snapshots of the change of the coordination environment around the fluorine species. The constraint hydrogen is colored cyan.

1526 kg/m^3 (727 °C) the dissociation energies become positive (see Tab.5.3).

The regression of the computed pK_a value with the density model [Anderson et al., 1991] in Fig. 5.11b shows a good correlation of the applied model with the WTmetaD results within an uncertainties of less than one logarithmic value. But at a density of ~800 kg/m^3 the acidity constants of both isotherms start to overlap. Comparing the experimental result by Ryzhenko [1965] (log K_a=6.2) at T=300 °C it appears that the computed pK_a value at 327 °C is 2.8 log value higher. Even the pK_a at 727 °C derived from the AIMD simulation are higher than the experimental values, the reported acidity constant by Barnes et al. [1966] at 450 °C as well. Only the HKF regression provides pK_a values close to the experimental data point by [Ryzhenko,

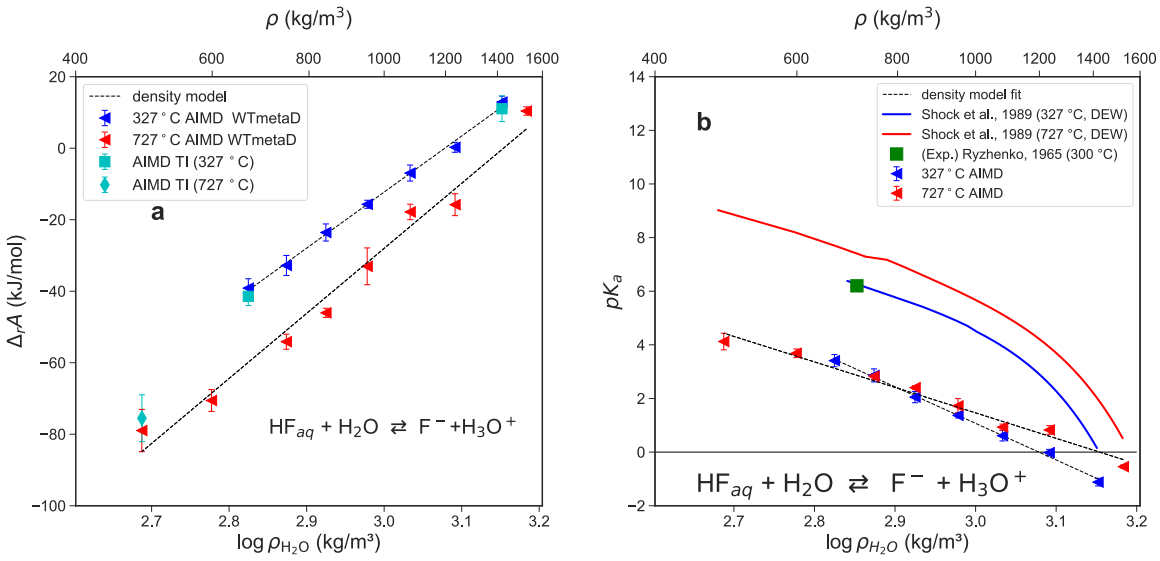

Figure 5.11: (a) the change of the Helmholtz free energy $\Delta_r A$ of the dissociation reaction of hydrofluoric acid derived from the WTmetaD simulation and thermodynamic integration as function of the logarithmic water density $\log(\rho_{H_2O})$. (b) variation in the computed acidity constant (pK_a) extracted from the WTMetaD vs. the logarithmic water density in comparison with experimental results by Ryzhenko [1965] and Barnes et al. [1966] and a HKF regression [Shock et al., 1989].

1965]. The computed acidity constants for both temperature conditions are significantly higher than the values given by Barnes et al. [1966] and the HKF regression. Only at high solvent densities (>1300 kg/m^3) the HKF results and the computed pK_a are approaching (see Tab. 5.3).

5.3 Discussion

HF Formation in Geological Fluids

The intramolecular atomic distance of hydrofluoric acid does not change significantly with changes of the system temperature and compression in accordance to previous AIMD results [Kreitmeir et al., 2003] and Monte Carlo simulations by Jedlovszky et al. [2001]. In contrast the solvent atomic configuration around the fluorine species goes through major changes over the considered P/T range. At pressures of over ~2000 MPa the atomic distances between the fluorine species and coordinating molecules become more similar between the low and high temperature runs. Further the $\Delta_r A$ of the HF_{aq} formation start to converge. This results is in agreement with observations by Mesmer et al. [1988] for $NH_{3\,aq}$, HCl_{aq} and $NaCl_{aq}$ that the variation of thermodynamic properties of solutes decreases with increasing compression.

The formation of the acid in aqueous solutions is a function of the compression of the solvent. Therefore, with increasing solvent density HF_{aq} tends to be destabilized. This can be seen in the high pressure unbiased AIMD runs and in the increase of the computed reaction Helmholtz free energies with increasing compression (Tab. 5.3). On the contrary with increasing temperature the uncharged HF_{aq} species is stabilized. Such a behavior is expected in high P/T aqueous systems and explained by the Born theory [Born, 1920, Ryzhenko, 2008, Manning, 2018, Sverjensky, 2019].

The discussed contribution of the entropic term in chapter 4 to the formation of aqueous species in solutions under high temperature seem to be rather small and constants concerning the hydration changes between the F^- and HF_{aq} in the system:

$$HF(H_2O)_m + (n - m + 1)H_2O \rightleftarrows H_3O^+ + [F(H_2O)_n]^- \qquad (n - m \simeq 1)$$

Therefore, the formation of HF_{aq} is mainly driven by the orientation of the water dipoles around the fluoride species within the WTmetaD. But due to the strong association of F^- with H_3O^+ at least at low P (and density), this contribution is not fully accounted and might lead to higher reaction free energies. To overcome this problem an additional proton acceptor could be added to the system. Therefore, a simulation cell with HF_{aq} + $NaCl_{aq}$ could be designed and metadynamics simulation performed with two collective variables: the F-H coordination and the F-Na distance. Such a setup of coupled aqueous reactions allows to sample the formation free energies of HF_{aq} and NaF_{aq}, whereas chloride would be available as proton acceptor. But the addition of a further collective variable would increases the computing time significantly. Because the computation cost scales exponentially with the number of collective variables [Valsson et al., 2016].

In the present case study the pK_a value is changing over 5 to 6 logarithmic units at the investigated pressure and temperature conditions. Comparison with experimental and theoretical predictions in Fig 5.11b indicate that the AIMD simulations results yield a much lower HF_{aq} stability at high temperatures. But the overlap of the regression lines for the low and high T conditions of the AIMD simulations is unexpected. The rather low pK_a values at 727 °C in comparison to 327 °C indicate that the applied sampling methods under estimate the HF_{aq} stability, particularly at high temperature and low solvent density. An another reason, as that

Table 5.4: Density model [Anderson et al., 1991] parameters derived in this case study from the WTMetaD simulations at 327 °C.

Parameter	Value
m_0	42.00
m_1	1.07 K
m_2	1.00 K^{-2}
m_3	0.00 K^{-3}
n_0	-13.64
n_1	0.98 K
n_2	1.00 K^{-2}

discussed above, could be the observed hysteresis that affects the reconstruction of the free energy surface [Barducci et al., 2011]. But due to the fact that both applied sampling methods gain comparable reaction energies this can not be main cause. More important should be the separation of the H_3O^+ form F^- during the dissociation reaction. As observed in the WTmetaD and in the thermodynamic integration under lower densities the oxonium ion is not completely separated from the fluoride after the intramolecular F-H bond is broken. Instead, H_3O^+ is located in the first or in the second hydration shell and a solvent separated ion pair is formed. Only at high solvent density the formed H_3O^+ separate to larger distances with respect to the halogen ion. Therefore, the computed pK_a represents only a partial dissociation constants. Whereas, the results for high solvent density (>1200kg/m^3) are considered to be more precise. The effect of insufficient ion separation is much stronger at 727 °C. Therefore, the parameters of the density model listed in Tab. 5.4 are derived only from the WTmetaD simulation at 327 °C. In Fig. 5.12 the predicted pK_a values using the listed parameters are charted with experimental results by Ellis [1963], Ryzhenko [1965], Richardson and Holland [1979] (transcribed from Richardson and Holland [1979]). It appears that the derived density model shows an offset of ~2-3 log units in comparison to results of the different studies a long the water vapor curve. It has to be emphasized, that the model parameters are derived a long an isochor and the model applicability is very limited. Furthermore, the computed pK_a=2.4 at ambient conditions (25 °C) is given. This quantity shows a much better agreement with the experiential results. Here a complete ion separation occurs during the dissociation reaction in the simulation cell.

The role of fluorine for the mobility of trace elements [Lecumberri-Sanchez et al., 2018] in metasomatic processes specially for rare earth elements (REE) is controversial [Williams-Jones

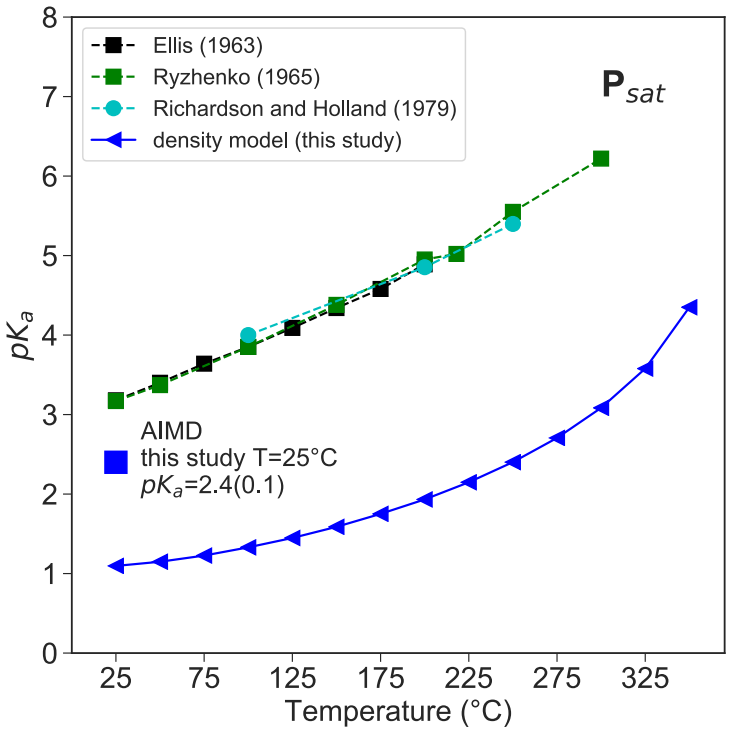

Figure 5.12: Change of the acidity constant (pK_a) of hydrofluoric acid along the water vapor curve. The density model based only on the dervied pK_a values at 327 °C

---

et al., 2012] and one of the main argument is strong association HF_{aq}. One the other hand, field experimental and theoretical studies [McPhie et al., 2011, Rapp et al., 2010, Xing et al., 2018] suggest that with increasing fluorine content in the system the solubility of trace elements as Cu, U, Ti and HREE increases under hydrothermal conditions. It needs to be emphasized that the strong association of fluorine with hydrogen highly depends on the pH value and therefore on the availability of H^+ in the system but the majority of the experimental studies use villiaumite (NaF) as a source of fluorine (see e.g. [Rapp et al., 2010, Tropper et al., 2013]) to ensure a more neural pH. Further, the relatively high fluorine content in the experiments in comparison to natural system could lead to a higher F^- activity and a higher mobility of trace elements in the experimental studies. Unfortunately, this case study can not provide new thermodynamic data of HF_{aq} at (low P) hydrothermal conditions. Only at very high solvent densities the derived thermodynamic properties are reliable. Interestingly, at high pressure conditions as in UHP metamorphism the results indicate a stronger dissociation of the acid. This outcome is in line

with observation form fluid-rock interaction in eclogite to amphibolite facies [John et al., 2011, Harlov et al., 2006] where high F activities are reconstructed from the mineral assemblage.

Implication for the Halogen Fractionation between Aqueous Fluids and Silicate Melts

At low pressures between 12-60 MPa and below the supercritical point HF_{aq} is strongly associated and hydrated by up to two water molecules. This number decreases to one in the supercritical low density regime at densities between 748-487 kg/m^3. For HCl_{aq} a hydration number of two is reported by [Mei et al., 2018] at 400°C and 30 MPa (388 kg/m^3). These two hydrogen halides are predicted to be the main species in volcanic vapors and in low density volcanic fluids [Symonds et al., 1994]. The main bromide species in such system are presumable Br_2, HBr, HOBr, BrO [Aiuppa et al., 2009, Gutmann et al., 2018]. Nevertheless, experimental EXAFS and molecular dynamics investigations of RbBr salt by Wallen et al. [1997] indicate that Br is coordinated by 3 water molecules at 425 °C and 30-70 MPa (327-514 kg/m^3). For iodine, the rarest halogen Seward and Driesner [2004], Seward et al. [2013] report a hydration of four to five water molecules in the temperature range of 315-350 °C and therefore the iodine coordination of four can be estimated at critical P/T conditions.

Combining these results a nearly linear correlation between the average integer hydration number with the ionic radius [Shannon, 1976] is obtained (Fig. 5.13). This tendency correlates with findings of Bureau et al. [2000] (see insert in Fig. 5.13) that the logarithm of the fluid/melt partition coefficient ($\ln D^{fluid/melt}$) is a linear function of the ionic radius. The higher solubility of F in silicate melts in comparison to fluids, according to different authors [Dolejš and Zajacz, 2018, Bureau et al., 2000], is driven by the formation of Si-F species in the melts [Dalou et al., 2015] due to the ionic radius of fluoride that is close to that of oxygen and hydroxide.

The solubility of solutes depends on an energetic contribution from the electrostatic interaction of the solute with the solvent and an entropic contribution due to structural reorganization of the solvent by the hydration of the solute [Hummer et al., 1996, Wolery and Jackson, 1990, Guillot et al., 1991]. At ambient conditions the free energy of hydration is mainly controlled by the energetic contribution [Webb, 1926], whereas with increasing temperature the entropic part becomes dominated [Mesmer et al., 1988] as shown for different solutes in supercritical water [Straatsma and Berendsen, 1988, Balbuena et al., 1996, Liu et al., 2011] on the molecular scale.

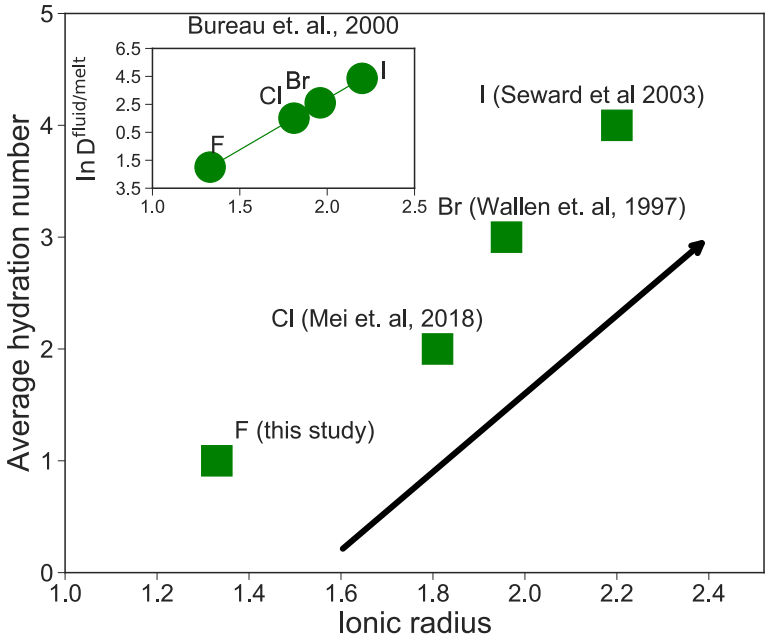

Figure 5.13: Relation between the hydration number of halogen species in low density supercritical fluids with the ionic radius. Insert: Dependency of the logarithmic fluid-melt partition coefficient ln $D^{fluid/melt}$ on the ionic radius (from Bureau et al. [2000]).

As presented in Fig. 5.13 the hydration number increases from F to I in the fluid phase while the fractionation of the halogens in to the fluid is getting stronger. There might be two possible explanations for that observation. Firstly, the decrease in the entropy due to the ordering and increasing number of the water molecules in first hydration shell, that lead to an increase of the electrostriction volume, does not change the chemical potential of the aqueous species sufficiently to overcome the structural constraint of the melt. Therefore, the melt composition and structure are the controlling factors of the halogen fractionation. Secondly, as shown for noble gas and methane by Guillot and Guissani [1993] at supercritical conditions the entropic contribution decreases with increasing polarizability (α) of the species. α for a chemical compound is constraint by the covalent character of the atomic bond. According to Pauling [1960] and assuming that all the halogens form acids in low density aqueous fluids the covalent bonding decreases from HI > HBr > HCl > HF within the halogen series. There might be a change in the chemical potential of the aqueous species due to the increasing polarizability acting as an additional driving force for the fractionation process.

Evaluating the hydration change of the fluorine species it becomes apparent that the coor-

dination number decease from 327 °C to 727 °C. Whereas, the transition species appears at all conditions. Such an behavior is known from other proton transfer reactions such as between hydroxide and water [Stefanski et al., 2018] due to geometrical constraints during the transfer reaction [Tuckerman et al., 1997].

5.4 Conclusion

In this case study *ab initio* molecular dynamics simulation in combination with the well-tempered variant of the metadynamic dynamics rare event sampling method are conducted to investigate the formation and behavior of hydrofluoric acid in geological fluids from crustal up to upper mantle P/T conditions. It has been demonstrated that the hydration structure of fluoride and its acid experience significant changes driven by compression and temperature. Further, the acidity of hydrofluoric acid was determined over a wide P/T range. Due to the insufficient separation of the fluoride and oxonium ion during the dissociation reaction the derived thermodynamic data differ significantly at high temperature and lower pressures. This outcome shows the limitation of sampling approaches when constraint on simple reaction coordinates in over simplified systems. To overcome this problem different ensembles of CVs e.g. the F-H_3O distance, or other sampling algorithm such umbrella sampling [Kumar et al., 1995, Roux, 1995] or thermodynamic integration [Carter et al., 1989, Sprik and Ciccotti, 1998] using the dummy atom transformation strategy [He et al., 2017] could be carried out in this system. Furthermore, coupled reaction could be investigated as outlined above. An alternatively approach was presented by Mei et al. [2018] by restraining the hydrogen coordination in the first coordination shell to zero. But as experience in case study II this can lead to huge uncertainties. Nevertheless, the presented results indicate a low HF_{aq} stability in high density aqueous fluids (e.g. subduction zone fluids) as ordinary HKF regression implied. Further, this case study present the first data of hydration properties of F^- and HF_{aq} so far (see Seward and Driesner [2004] for an overview).

The role of halide species in aqueous fluids and vapor during fluid/melt segregation in volcanic processes is quite unknown [Aiuppa et al., 2009]. Considering the presented results the polarizability of the species could enhance the fractionation behavior. In future investigations the speciation of the halogen series has to be verified using e.g the hydrothermal diamond

anvil cell device [Schmidt and Chou, 2012] in combination with Raman spectroscopy or x-ray absorption techniques and/or AIMD/classical MD simulations.

Chapter 6

DISCUSSION AND OUTLOOK

In recent years, the methodology to compute free energy landmarks of chemical reactions was driven forward [Shiga and Tuckerman, 2018, Pietrucci, 2017, Yang et al., 2018]. Various studies were performed focusing on aqueous reaction mechanism [Park et al., 2006, Stirling and Pápai, 2010, Galib and Hanna, 2014, Pietrucci et al., 2018], but further quantitative reproducibility of experiential results was achieved for different systems [Mangold et al., 2011, Liu et al., 2010, Galib and Hanna, 2011, Bühl and Grenthe, 2011]. Therefore, AIMD simulations becomes a powerful tool to gain semiquantitative thermodynamic data even for high temperature and/or high pressure aqueous geochemistry systems as shown by Yan Mei and co-workers (see e.g. Mei et al. [2015]). Three different case studies with two different free energy sampling methods were carried out in the framework of this PhD thesis.

A basic concept in thermodynamic is to compare energy differences for the distinction of stable system states referring to standard or reference states, rather than using absolute values of the thermodynamic potential. This thermodynamic quantities of a standard states have to be concentrated independently to use them for thermodynamic modeling. Especially AIMD simulation is limited in the system size and the Bjerrum length [Bjerrum, 1926], the minimum distance from which an ion in solution can be considered as "free", cannot be satisfied. Therefore, ion-ion interaction can affect the computed thermodynamic quantities in chemical diverse systems. In the past, infinite dilution properties of aqueous electrolyte under hydrothermal conditions have been computed, e.g. for alkali halides from rather large simulation cells containing only one unit of the investigated compound [Driesner et al., 1998, Chialvo et al., 1995, Yui et al., 2010] like in case study III (chapter 5). Activity correction using the Debye-Hückel approach as applied in case study I (see chapter 3) and by other authors [Mei et al., 2013] might not be an appropriate way to estimate properties at infinite dilution, because it is questionable that long range interactions in the strictly periodic simulation system are directly comparable to macroscopic ensembles [Todorova et al., 2008]. As demonstrated by

Hünenberger and McCammon [1999], the Ewald summation that is used to build up an infinite system of periodic replications of the simulation cell leads to strong perturbations in the solvation free energies especially for highly charge ions and low dielectric permittivity. This perturbation varies with the cubic root of the ionic strength in contrast to the square root as accounted in the Debye-Hückel approach. Apart from that, the assumption that solutes (electrolytes and non-electrolytes) behave as point charged spheres might be oversimplified. Furthermore, model parameters as the mean distance of the closest approach ($\mathring{a}$) are commonly taken from Kielland [1937b] or Marcus [1988], but those rather old data vary widely from more recently published data sets [Ribeiro et al., 2006, 2010]. In my point of view, investigations to systematically evaluate the impact of artificial periodic electrostatics and neutralizing background charge on the computed thermodynamic properties derived from AIMD simulations especially at high temperatures are necessary.

The thermodynamic integration method to gain free energy differences from constrained molecular dynamics simulation as it is applied in all three case studies, shows two fundamental problems. Firstly, the possibility to explore a new reaction pathway is very limited due to the pre-specified reaction coordinates. Secondly, a separation of intermediate states from the free energy profile as observed in case study I, is not possible. But the advantage in comparison to the metadynamics approach, that does account this limitations, is a rather fast free energy convergence.

The combination of metadynamics and DFT based MD simulations require long simulation times. This requirement is obstructive, because the number of feasible simulations is limited due to the computational costs and *ab initio* metadynamics run impede the performance of test runs to verify different CV's and metadynamic parameters (e.g. deposition time, bias factor etc.). Nevertheless, it is the most promising approach to investigate thermophysical properties of solute in geological fluids from a molecular dynamic point of view.

In the past, molecular dynamics studies e.g. of the formation of acids at ambient [Sakti et al., 2018] and hydrothermal conditions [Pietrucci et al., 2018] refer to *ab initio* approaches. The reason for that is the limitation of classic force-field potentials to encounter the proton transfer reaction between proton donors and proton acceptors. Furthermore, only a few interaction potentials are designed for high P/T conditions. New developments of reactive force-fields[1]

[1] reactive force-fields: interaction potentials that allow continuous bond formation and breaking

(e.g ReaxFF [van Duin et al., 2001, Senftle et al., 2016] or the dissociable water model by Halley et al. [1993]) enable the investigation of material at high temperature and/or high pressure (see e.g. Chenoweth et al. [2005], Ashraf et al. [2017]). Moreover, these potentials overcome the general systematic error of the DFT approach of missing longer range electron correlation (e.g. van der Waals force). An alternative approach is to combine classic force-field potentials and DFT based molecular dynamics by designing interaction potentials from small size AIMD simulations of phases of interest [Demichelis et al., 2011]. Even more capabilities are provided by new developments of neural-network potentials using machine learning algorithms [Behler and Parrinello, 2007, Behler, 2014, Ye et al., 2018, Cheng et al., 2019], which might be capable to enable the investigation of the system size and chemical diversity close to nature ensembles. For future studies, a benchmark of the different approaches at high temperature and high pressure should be carried out in a model system, where high proton mobility and P/T depended association is presumed, e.g. $NaOH_{aq}$ as conducted at ambient conditions [Hellström et al., 2018].

Nevertheless, the conducted case studies in this thesis provide new insights of import aqueous geochemistry systems: The first high temperature and high pressure thermodynamic properties of yttrium chloride aqueous species. An interesting observation is that yttrium(III) drives protolysis of its aqueous solvent as it was observed for titanium. Therefore, it might be a general property of high field strength elements in high pressure and high temperature fluids. Secondly, the coordination changes of beryllium(II) in hydrothermal fluids that might enable a higher mobility of Be in hydrothermal systems as known from zinc. Thirdly, hydration properties of F^-/HF_{aq} are investigated for the first time and could be used as reference for further experimental studies. Moreover, new HF_{aq} acidity constants is reported that could help to shed light on the role of fluorine in UHP metasomatism.

For future studies, it might be a promising approach to rigorously compute the hydration energies of alkali metals, halides etc. in aqueous solution under hydrothermal (critical) conditions to identify the geochemical systems, where the extrapolations of solvation energies measured at ambient conditions to higher P/T conditions using a Born-model-based equation of state lead to high inaccuracy. Furthermore, such a systematic study would help to gain a better understanding of the solvent structure change with increasing temperature on system specific

thermodynamic quantities. Future case studies that might be based on the results of this thesis could focus on the speciation of light rare earth elements (LREE) halides in subduction zone fluid as a comparative study. Such a study could gain deeper insights into the fraction of HREE and LREE from a molecular point of view. Building on the study of beryllium speciation in magmatic aqueous fluids, the association of Be with OH^- or CO_3^{2-} is necessary for a comprehensive understanding of the behavior of beryllium in late magmatic systems. Our knowledge of the dissolution and exsolution behavior of volatile elements particularly halogens in aluminosilicate melts and aqueous phases (vapour, hydrosaline liquid, vapour + hydrosaline liquid, fluid) in volcanic systems lacks on the speciation of these elements [Aiuppa et al., 2009]. Here, AIMD and classical MD simulations using a free energy sampling algorithm in combination with spectroscopic techniques using in-situ experimental devices as the hydrothermal diamond anvil cell could yield a variety of new insights.

BIBLIOGRAPHY

J. J. Ague. Element mobility during regional metamorphism in crustal and subduction zone environments with a focus on the rare earth elements (REE). *Am. Mineral.*, 102(9):1796–1821, 2017.

A. Aiuppa, D. R. Baker, and J. D. Webster. Halogens in volcanic systems. *Chem. Geol.*, 263 (1):1–18, 2009.

N. N. Akinfiev and L. W. Diamond. Thermodynamic description of aqueous nonelectrolytes at infinite dilution over a wide range of state parameters. *Geochim. Cosmochim. Acta*, 67(4): 613–629, 2003.

A. M. Aksyuk. Estimation of fluorine concentrations in fluids of mineralized skarn systems. *Econom. Geol.*, 95(6):1339–1347, 2000.

P. Allen and D. Tildesley. *Computer Simulation of Liquids*. Oxford University Press: Oxford, UK, 1987.

J. C. Alt, W. C. Shanks, and M. C. Jackson. Cycling of sulfur in subduction zones: The geochemistry of sulfur in the Mariana Island Arc and back-arc trough. *Earth Planet. Sci. Lett.*, 119(4):477–494, 1993.

G. Anderson. *Thermodynamics of Natural Systems*. Cambridge University Press, Cambridge, 2 edition, 2009.

G. M. Anderson and D. A. Crerar. *Thermodynamics in Geochemistry: The Equilibrium Model*. Oxford University Press, New York, 1 edition edition, 1993.

G. M. Anderson, S. Castet, J. Schott, and R. E. Mesmer. The density model for estimation of thermodynamic parameters of reactions at high temperatures and pressures. *Geochim. Cosmochim. Acta*, 55(7):1769–1779, 1991.

L. Aranovich and O. Safonov. Halogens in high-grade metamorphism. In D. E. Harlov and L. Aranovich, editors, *The Role of Halogens in Terrestrial and Extraterrestrial Geochemical Processes*, pages 713–757. Springer International Publishing, Cham, 2018.

S. Arnórsson, A. Stefánsson, and J. O. Bjarnason. Fluid-fluid interactions in geothermal systems. *Rev. Mineral. Geochem.*, 65(1):259–312, 2007.

C. Ashraf, A. Jain, Y. Xuan, and A. C. T. v. Duin. ReaxFF based molecular dynamics simulations of ignition front propagation in hydrocarbon/oxygen mixtures under high temperature and pressure conditions. *PCCP*, 19(7):5004–5017, 2017.

J. Ayers. Trace element modeling of aqueous fluid – peridotite interaction in the mantle wedge of subduction zones. *Contrib. Mineral Petrol.*, 132(4):390–404, Sept. 1998.

P. Ayotte, M. Hébert, and P. Marchand. Why is hydrofluoric acid a weak acid? *J. Chem. Phys.*, 123(18):184501, 2005.

P. B. Balbuena, K. P. Johnston, and P. J. Rossky. Molecular dynamics simulation of electrolyte solutions in ambient and supercritical water. 1. ion solvation. *J. Phys. Chem.*, 100(7):2706–2715, 1996.

E. Bali, H. Keppler, and A. Audetat. The mobility of W and Mo in subduction zone fluids and the Mo–W–Th–U systematics of island arc magmas. *Earth Planet. Sci. Lett.*, 351–352: 195–207, 2012.

D. A. Banks, B. W. D. Yardley, A. R. Campbell, and K. E. Jarvis. REE composition of an aqueous magmatic fluid: A fluid inclusion study from the Capitan Pluton, New Mexico, U.S.A. *Chem. Geol.*, 113(3–4):259–272, 1994.

A. Barducci, G. Bussi, and M. Parrinello. Well-Tempered Metadynamics: A Smoothly Converging and Tunable Free-Energy Method. *Phys. Rev. Lett.*, 100(2):020603, 2008.

A. Barducci, M. Bonomi, and M. Parrinello. Metadynamics. *WIREs Comput. Mol. Sci.*, 1(5): 826–843, 2011.

H. L. Barnes. *Solubilities of ore minerals. In: Geochemistry of hydrothermal ore deposits*. John Wiley & Sons, New York, 2 edition, 1979.

H. L. Barnes, H. C. Helgeson, and A. J. Ellis. Section 16: Ionization constants in aqueous solutions. In *Geological Society of America Memoirs*, volume 97, pages 401–414. Geological Society of America, 1966.

J. D. Barnes, C. E. Manning, M. Scambelluri, and J. Selverstone. The behavior of halogens during subduction-zone processes. In D. E. Harlov and L. Aranovich, editors, *The Role of Halogens in Terrestrial and Extraterrestrial Geochemical Processes*, pages 545–590. Springer International Publishing, Cham, 2018.

M. Bau and P. Dulski. Comparative study of yttrium and rare-earth element behaviours in fluorine-rich hydrothermal fluids. *Contr. Mineral. and Petrol.*, 119(2-3):213–223, 1995.

G. E. Bebout, J. G. Ryan, and W. P. Leeman. B/Be systematics in subduction-related metamorphic rocks: Characterization of the subducted component. *Geochim. Cosmochim. Acta*, 57 (10):2227–2237, 1993.

A. D. Becke. Density-functional exchange-energy approximation with correct asymptotic behavior. *Phys. Rev. A*, 38(6):3098–3100, 1988.

J. Behler. Representing potential energy surfaces by high-dimensional neural network potentials. *J. Phys.: Condens. Matter*, 26(18):183001, 2014.

J. Behler and M. Parrinello. Generalized neural-network representation of high-dimensional potential-energy surfaces. *Phys. Rev. Lett.*, 98(14):146401, 2007.

A. Beran and E. Libowitzky. Water in natural mantle minerals II: Olivine, garnet and accessory minerals. *Rev. Mineral. Geochem.*, 62(1):169–191, 2006.

H. J. C. Berendsen, J. R. Grigera, and T. P. Straatsma. The missing term in effective pair potentials. *J. Phys. Chem.*, 91(24):6269–6271, 1987.

A. A. Beus. *Geochemistry of beryllium and genetic types of beryllium deposits*, volume 1. W. H. Freeman and Company, Institue of Mineralogy, Geochemistry, and Crystal Chemistry of Rare Elements, Academy of Science, Moscow, The UUSR, 1966.

C. Beyer, S. Klemme, M. Wiedenbeck, A. Stracke, and C. Vollmer. Fluorine in nominally fluorine-free mantle minerals: Experimental partitioning of F between olivine, orthopyroxene and silicate melts with implications for magmatic processes. *Earth Planet. Sci. Lett.*, 337–338: 1–9, 2012.

H. M. Bibby, T. G. Caldwell, F. J. Davey, and T. H. Webb. Geophysical evidence on the structure of the Taupo Volcanic Zone and its hydrothermal circulation. *J. Volcanol. Geotherm. Res.*, 68(1):29–58, 1995.

N. Bjerrum. No title available. *Kgl. Dan. Vidensk. Selsk. Mat.-fys. Medd.*, 7(1), 1926.

M. Bonomi, D. Branduardi, G. Bussi, C. Camilloni, D. Provasi, P. Raiteri, D. Donadio, F. Marinelli, F. Pietrucci, R. A. Broglia, and M. Parrinello. PLUMED: A portable plugin for free-energy calculations with molecular dynamics. *Comput. Phys. Commun.*, 180 (10):1961–1972, 2009.

M. Borchert, M. Wilke, C. Schmidt, K. Kvashnina, and S. Jahn. Strontium complexation in aqueous solutions and silicate glasses: Insights from high energy-resolution fluorescence detection X-ray spectroscopy and ab-initio modeling. *Geochim. Cosmochim. Acta*, 142: 535–552, 2014.

R. J. Borg and G. J. Dienes. *The Physical Chemistry of Solids*. Academic Press, 1992.

M. Born. Volumen und hydratationswärme der ionen. *Zeit. Physik*, 1(1):45–48, Feb 1920.

J. M. Brenan. Partitioning of fluorine and chlorine between apatite and aqueous fluids at high pressure and temperature: implications for the F and Cl content of high P-T fluids. *Earth Planet. Sci. Lett.*, 117(1):251–263, 1993.

P. W. Bridgman. The Pressure-Volume-Temperature Relations of the Liquid, and the Phase Diagram of Heavy Water. *J. Chem. Phys.*, 3(10):597–605, 1935.

P. L. Brown and C. Ekberg, editors. *Alkaline Earth Metals*. Wiley-VCH Verlag GmbH & Co. KGaA, 2016.

J. Brugger, W. Liu, B. Etschmann, Y. Mei, D. M. Sherman, and D. Testemale. A review of the coordination chemistry of hydrothermal systems, or do coordination changes make ore deposits? *Chem. Geol.*, 447:219–253, 2016.

K. Bucher and I. Stober. Fluids in the upper continental crust. *Geofluids*, 10(1-2):241–253, 2010.

M. Bühl and V. Golubnychiy. Binding of pertechnetate to Uranyl(VI) in aqueous solution. A density functional theory molecular dynamics study. *Inorg. Chem.*, 46(20):8129–8131, 2007.

M. Bühl and I. Grenthe. Binding modes of oxalate in UO_2(oxalate) in aqueous solution studied with first-principles molecular dynamics simulations. Implications for the chelate effect. *Dalton Trans.*, 40(42):11192–11199, 2011.

M. S. T. Bukowinski. First principles equations of state of MgO and CaO. *Geophysical Research Letters*, 12(8):536–539, 1985.

K. B. Bulnaev. Origin of the fluorite-bertrandite-phenakite deposits. *Geol. Ore Depos.*, 38(2): 128–136, 1996.

H. Bureau, H. Keppler, and N. Métrich. Volcanic degassing of bromine and iodine: experimental fluid/melt partitioning data and applications to stratospheric chemistry. *Earth Planet. Sci. Lett.*, 183(1):51–60, 2000.

C. Burnham, J. Holloway, and N. Davis. The specific volume of water in the range 1000 to 8900 bars, 20 to 900°C. *Amer. J. Sci.*, 267 A(A):70–95, 1969.

R. Car and M. Parrinello. Unified approach for molecular dynamics and density-functional theory. *Phys. Rev. Lett.*, 55:2471–2474, 1985.

E. A. Carter, G. Ciccotti, J. T. Hynes, and R. Kapral. Constrained reaction coordinate dynamics for the simulation of rare events. *Chem. Phys. Lett.*, 156(5):472–477, 1989.

C. R. A. Catlow, J. M. Thomas, S. C. Parker, and D. A. Jefferson. Simulating silicate structures and the structural chemistry of pyroxenoids. *Nature*, 295(5851):658–662, 1982.

Z. S. Cetiner, S. A. Wood, and C. H. Gammons. The aqueous geochemistry of the rare earth elements. Part XIV. The solubility of rare earth element phosphates from 23 to 150 °C. *Chem. Geol.*, 217(1):147–169, 2005.

A. R. Chakhmouradian and A. N. Zaitsev. Rare Earth Mineralization in Igneous Rocks: Sources and Processes. *Elements*, 8(5):347–353, 2012.

W. T. Chen and M.-F. Zhou. Ages and compositions of primary and secondary allanite from the Lala Fe–Cu deposit, SW China: implications for multiple episodes of hydrothermal events. *Contrib. Mineral Petrol.*, 168(2):1043, 2014.

B. Cheng, E. A. Engel, J. Behler, C. Dellago, and M. Ceriotti. Ab initio thermodynamics of liquid and solid water. *PNAS*, 116(4):1110–1115, 2019.

K. Chenoweth, S. Cheung, A. C. T. van Duin, W. A. Goddard, and E. M. Kober. Simulations on the thermal decomposition of a poly (dimethylsiloxane) polymer using the ReaxFF reactive force field. *J. Am. Chem. Soc.*, 127(19):7192–7202, 2005.

A. A. Chialvo and P. T. Cummings. Molecular-based modeling of water and aqueous solutions at supercritical conditions. *Adv. Chem. Phys.*, 1999.

A. A. Chialvo, P. T. Cummings, H. D. Cochran, J. M. Simonson, and R. E. Mesmer. Na^+–Cl^- ion pair association in supercritical water. *J. Chem. Phys.*, 103(21):9379–9387, 1995.

A. A. Chialvo, P. T. Cummings, J. M. Simonson, and R. E. Mesmer. Solvation in high-temperature electrolyte solutions. I. Hydration shell behavior from molecular simulation. *J. Chem. Phys.*, 110(2):1064–1074, 1998a.

A. A. Chialvo, P. T. Cummings, J. M. Simonson, and R. E. Mesmer. Solvation in high-temperature electrolyte solutions. II. Some formal results. *J. Chem. Phys.*, 110(2):1075–1086, 1998b.

G. Ciccotti, R. Kapral, and E. Vanden-Eijnden. Blue moon sampling, vectorial reaction coordinates, and unbiased constrained dynamics. *Chem. Phys Chem.*, 6(9):1809–1814, 2005.

F. Constantinescu and E. Magyari. *Problems in Quantum Mechanics*. Elsevier, 2013.

CPMD. Copyright IBM Corp 1990-2019, Copyright MPI für Festkörperforschung Stuttgart 1997-2001, 1990. http://www.cpmd.org/.

W. A. Crawford and W. S. Fyfe. Lawsonite equilibria. *Am. J. Sci.*, 263(3):262–270, 1965.

S. T. Cui and J. G. Harris. Solubility of sodium chloride in supercritical water: A molecular dynamics study. *J. Phys. Chem.*, 99(9):2900–2906, 1995.

S. R. Dailey, E. H. Christiansen, M. J. Dorais, B. J. Kowallis, D. P. Fernandez, and D. M. Johnson. Origin of the fluorine- and beryllium-rich rhyolites of the Spor Mountain Formation, Western Utah. *Am. Mineral.*, 103(8):1228–1252, 2018.

C. Dalou, B. O. Mysen, and D. Foustoukos. In-situ measurements of fluorine and chlorine speciation and partitioning between melts and aqueous fluids in the Na_2O-Al_2O_3-SiO_2-H_2 O system. *Am. Mineral*, 100(1):47–58, 2015.

L. Damdinova and F. Reyf. The origin of low-Be quartz-fluorite field at the Ermakovskoe high-grade F-Be-ore deposit. *Russs. Geol. Geophys.*, 49(11):816–826, 2008.

L. B. Damdinova, B. B. Damdinov, M. O. Rampilov, and S. V. Kanakin. Ore formation conditions of the Aunik F-Be deposit (western transbaikalia). *Geol. Ore Deposits*, 61(1): 14–37, 2019.

E. Darve, D. Rodríguez-Gómez, and A. Pohorille. Adaptive biasing force method for scalar and vector free energy calculations. *J. Chem. Phys.*, 128(14):144120, 2008.

C. W. Davies. *Ion association*. Butterworths, Washington, 1962.

P. G. Debenedetti and M. L. Klein. Chemical physics of water. *PNAS*, 114(51):13325–13326, 2017.

R. Demichelis, P. Raiteri, J. D. Gale, D. Quigley, and D. Gebauer. Stable prenucleation mineral clusters are liquid-like ionic polymers. *Nat. Commun.*, 2:590, 2011.

J. M. Dick. Calculation of the relative metastabilities of proteins using the CHNOSZ software package. *Geochem. T.*, 9(1):10, 2008.

D. Dolejš. Thermodynamics of aqueous species at high temperatures and pressures: Equations of state and transport theory. *Rev. Mineral. Geochem.*, 76(1):35–79, 2013.

D. Dolejš and C. E. Manning. Thermodynamic model for mineral solubility in aqueous fluids: theory, calibration and application to model fluid-flow systems. *Geofluids*, 10(1-2):20–40, 2010.

D. Dolejš and Z. Zajacz. Halogens in silicic magmas and their hydrothermal systems. In D. E. Harlov and L. Aranovich, editors, *The Role of Halogens in Terrestrial and Extraterrestrial Geochemical Processes*, pages 431–543. Springer International Publishing, Cham, 2018.

K. J. Domanik and J. R. Holloway. The stability and composition of phengitic muscovite and associated phases from 5.5 to 11 GPa: Implications for deeply subducted sediments. *Geochim. Cosmochim. Acta*, 60(21):4133–4150, 1996.

T. Driesner. The molecular-scale fundament of geothermal fluid thermodynamics. *Rev. Mineral. Geochem.*, 76(1):5–33, 2013.

T. Driesner, T. M. Seward, and I. G. Tironi. Molecular dynamics simulation study of ionic hydration and ion association in dilute and 1 molal aqueous sodium chloride solutions from ambient to supercritical conditions. *Geochim. Cosmochim. Acta*, 62(18):3095–3107, 1998.

Q. Duc-Tin, A. Audétat, and H. Keppler. Solubility of tin in (Cl, F)-bearing aqueous fluids at 700 °C, 140 MPa: A LA-ICP-MS study on synthetic fluid inclusions. *Geochim. Cosmochim. Acta*, 71(13):3323–3335, 2007.

D. Eisenberg and W. Kauzmann. *The Structure and Properties of Water*. Oxford: Clarendon Press, 2005.

A. M. Elena, S. Meloni, and G. Ciccotti. Equilibrium and rate constants, and reaction mechanism of the HF dissociation in the $HF(H_2O)_7$ cluster by ab-initio rare event simulations. *J. Phys. Chem. A*, 117(49):13039–13050, 2013.

A. J. Ellis. 823. The effect of temperature on the ionization of hydrofluoric acid. *J. Chem. Soc.*, 0(0):4300–4304, 1963.

B. Ensing, A. Laio, M. Parrinello, and M. L. Klein. A recipe for the computation of the free energy barrier and the lowest free energy path of concerted reactions. *J. Phys. Chem. B*, 109 (14):6676–6687, 2005.

B. Ensing, M. De Vivo, Z. Liu, P. Moore, and M. L. Klein. Metadynamics as a tool for exploring free energy landscapes of chemical reactions. *Acc. Chem. Res*, 39(2):73–81, 2006.

J. R. Errington and P. G. Debenedetti. Relationship between structural order and the anomalies of liquid water. *Nature*, 409(6818):318–321, 2001.

B. Etschmann, W. Liu, R. Mayanovic, Y. Mei, S. Heald, R. Gordon, and J. Brugger. Zinc transport in hydrothermal fluids: On the roles of pressure and sulfur vs. chlorine complexing. *Am. Mineral.*, 104(1):158–161, 2019.

J. M. Evensen, D. London, and R. F. Wendlandt. Solubility and stability of beryl in granitic melts. *Am. Mineral*, 84(5-6):733–745, 1999.

D. P. Fernàndez, A. R. H. Goodwin, E. W. Lemmon, J. M. H. Levelt Sengers, and R. C. Williams. A formulation for the static permittivity of water and steam at temperatures from 238 K to 873 K at pressures up to 1200 MPa, including derivatives and Debye–Hückel coefficients. *J. Phys. Chem. Ref. Data*, 26(4):1125–1166, 1997.

S. Ferrando, M. L. Frezzotti, L. Dallai, and R. Compagnoni. Multiphase solid inclusions in UHP rocks (Su-Lu, China): Remnants of supercritical silicate-rich aqueous fluids released during continental subduction. *Chem. Geol.*, 223(1):68–81, 2005.

A. R. Finney, S. Lectez, C. L. Freeman, J. H. Harding, and S. Stackhouse. Ion association in lanthanide chloride solutions. *Chem. Eur. J. Chemistr.*, 0(25):1–18, 2019.

N. K. Foley, A. H. Hofstra, D. A. Lindsey, R. R. Seal, II, B. W. Jaskula, and N. M. Piatak. Occurrence model for volcanogenic beryllium deposits: Chapter F in Mineral deposit models for resource assessment. USGS Numbered Series 2010-5070-F, U.S. Geological Survey, Reston, VA, 2012.

D. I. Foustoukos and W. E. Seyfried. Fluid phase separation processes in submarine hydrothermal systems. *Rev. Mineral. Geochem.*, 65(1):213–239, 2007.

E. Franck. Hochverdichteter Wasserdampf II. Ionendissoziation von KCl in H_2O bis 750 °C. *Z. Physikal. Chem*, 8:92–107, 1956.

E. U. Franck. Überkritisches Wasser als elektrolytisches Lösungsmittel. *Angew. Chem.*, 73(10): 309–322, 1961.

E. U. Franck, S. Rosenzweig, and M. Christoforakos. Calculation of the dielectric constant of water to 1000°C and very high pressures. *Ber. Bunsenges. Phys. Chem.*, 94(2):199–203, 1990.

G. Franz and G. Morteani. Be-minerals: Synthesis, stability, and occurrence in metamorphic rocks. *Rev. Mineral. Geochem.*, 50(1):551–589, 2002.

D. Frenkel and B. Smit. *Understanding Molecular Simulation: From Algorithms to Applications*. Academic Press, Inc., 1996.

M. Galib and G. Hanna. Mechanistic insights into the dissociation and decomposition of carbonic acid in water via the hydroxide route: An ab initio metadynamics study. *J. Phys. Chem. B*, 115(50):15024–15035, 2011.

M. Galib and G. Hanna. Molecular dynamics simulations predict an accelerated dissociation of H_2CO_3 at the air–water interface. *PCCP*, 16(46):25573–25582, 2014.

G. Galli and D. Pan. A closer look at supercritical water. *PNAS*, 110(16):6250–6251, 2013.

M. E. Galvez, J. A. D. Connolly, and C. E. Manning. Implications for metal and volatile cycles from the pH of subduction zone fluids. *Nature*, 539(7629):420–424, 2016.

S. Goedecker, M. Teter, and J. Hutter. Separable dual-space Gaussian pseudopotentials. *Phys. Rev. B*, 54(3):1703–1710, 1996.

A. F. Goncharov, N. Goldman, L. E. Fried, J. C. Crowhurst, I.-F. W. Kuo, C. J. Mundy, and J. M. Zaug. Dynamic Ionization of Water under Extreme Conditions. *Phys. Rev. Lett.*, 94 (12):125508, 2005.

T. Graupner, U. Kempe, E. Dombon, O. Pätzold, O. Leeder, and E. T. C. Spooner. Fluid regime and ore formation in the tungsten(–yttrium) deposits of Kyzyltau (Mongolian Altai): evidence for fluid variability in tungsten–tin ore systems. *Chem. Geol.*, 154(1–4):21–58, 1999.

E. S. Grew. Mineralogy, petrology and geochemistry of beryllium: An introduction and list of beryllium minerals. *Rev. Mineral. Geochem.*, 50(1):1–76, 2002a.

E. S. Grew. Beryllium in metamorphic environments (emphasis on aluminous compositions). *Rev. Mineral. Geochem.*, 50(1):487–549, 2002b.

S. Grimme. Semiempirical GGA-type density functional constructed with a long-range dispersion correction. *J. Comput. Chem*, 27(15):1787–1799, 2006.

B. Guillot and Y. Guissani. Accomputer simulation study of the temperature dependence of the hydrophobic hydration. *J. Chem. Phys.*, 99(10):8075–8094, 1993.

B. Guillot, Y. Guissani, and S. Bratos. A computer-simulation study of hydrophobic hydration of rare gases and of methane. I. Thermodynamic and structural properties. *J. Chem. Phys.*, 95(5):3643–3648, 1991.

R. W. Gurney. *Ionic Processes In Solution*. McGraw-Hill Book Company, Inc, 1953.

A. Gutmann, N. Bobrowski, T. J. Roberts, J. Rüdiger, and T. Hoffmann. Advances in bromine speciation in volcanic plumes. *Front. Earth Sci.*, 6, 2018.

J. R. Haas, E. L. Shock, and D. C. Sassani. Rare earth elements in hydrothermal systems: Estimates of standard partial molal thermodynamic properties of aqueous complexes of the rare earth elements at high pressures and temperatures. *Geochim. Cosmochim. Acta*, 59(21): 4329–4350, 1995.

B. R. Hacker. H_2O subduction beyond arcs. *Geochem. Geophys. Geosyst.*, 9(3), 2008.

J. W. Halley, James R. Rustad, and A. Rahman. A polarizable, dissociating molecular dynamics model for liquid water. *J. Chem. Phys.*, 98(5):4110–4119, 1993.

D. R. Hamann, M. Schlüter, and C. Chiang. Norm-Conserving pseudopotentials. *Phys. Rev. Lett.*, 43(20):1494–1497, 1979.

C. J. Hardy, B. F. Greenfield, and D. Scargill. 33. The solvent-extraction of beryllium from aqueous solutions of mineral acids by alkyl esters of phosphoric acid. *J. Chem. Soc.*, pages 174–182, 1961.

D. E. Harlov and L. Aranovich, editors. *The Role of Halogens in Terrestrial and Extraterrestrial Geochemical Processes*. Springer Geochemistry. Springer International Publishing, Cham, 2018.

D. E. Harlov, L. Johansson, A. Van Den Kerkhof, and H.-J. Förster. The role of advective fluid flow and diffusion during localized, solid-state dehydration: Söndrum Stenhuggeriet, Halmstad, SW Sweden. *J Petrology*, 47(1):3–33, 2006.

D. J. Harris, J. P. Brodholt, and D. M. Sherman. Zinc complexation in hydrothermal chlroide brines: Results from ab initio molecular dynamcis calculations. *J. Phys. Chem. A*, 107(7): 1050–1054, 2003a.

D. J. Harris, J. P. Brodholt, and D. M. Sherman. Hydration of Sr^{2+} in hydrothermal solutions from ab initio molecular dynamics. *J. Phys. Chem. B*, 107(34):9056–9058, 2003b.

C. Hartwigsen, S. Goedecker, and J. Hutter. Relativistic separable dual-space Gaussian pseudopotentials from H to Rn. *Phys. Rev. B*, 58(7):3641–3662, 1998.

F. C. Hawthorne and D. M. C. Huminicki. The crystal chemistry of beryllium. *Rev. Mineral. Geochem.*, 50(1):333–403, 2002.

M. He, X. Liu, X. Lu, C. Zhang, and R. Wang. Structure, acidity, and metal complexing properties of oxythioarsenites in hydrothermal solutions. *Chem. Geol.*, 471(Supplement C): 131–140, 2017.

J. W. Hedenquist and J. B. Lowenstern. The role of magmas in the formation of hydrothermal ore deposits. *Nature*, 370(6490):519–527, 1994.

G. T. Hefter. Acidity constant of hydrofluoric acid. *J. Solution. Chem.*, 13(7):457–470, 1984.

K. Heger, M. Uematsu, and E. U. Franck. The static dielectric constant of water at high pressures and temperatures to 500 MPa and 550°C. *Berichte der Bunsengesellschaft für physikalische Chemie*, 84(8):758–762, 1980.

H. C. Helgeson. Thermodynamics of complex dissociation in aqueous solution at elevated temperatures. *J. Phys. Chem.*, 71(10):3121–3136, 1967.

H. C. Helgeson. Thermodynamics of hydrothermal systems at elevated temperatures and pressures. *Am. J. Sci.*, 267(7):729–804, 1969.

H. C. Helgeson and D. H. Kirkham. Theoretical prediction of the thermodynamic behavior of aqueous electrolytes at high pressures and temperatures; I, Summary of the thermodynamic/electrostatic properties of the solvent. *Am. J. Sci.*, 274(10):1089–1198, 1974.

H. C. Helgeson and D. H. Kirkham. Theoretical prediction of the thermodynamic properties of aqueous electrolytes at high pressures and temperatures. III. Equation of state for aqueous species at infinite dilution. *Am. J. Sci.*, 276(2):97–240, 1976.

H. C. Helgeson, D. H. Kirkham, and G. C. Flowers. Theoretical prediction of the thermodynamic behavior of aqueous electrolytes by high pressures and temperatures; IV, Calculation of activity coefficients, osmotic coefficients, and apparent molal and standard and relative partial molal properties to 600 °C and 5 kb. *Am, J, Sci.*, 281(10):1249–1516, 1981.

M. Hellström, M. Ceriotti, and J. Behler. Nuclear Quantum effects in sodium hydroxide solutions from neural network molecular dynamics simulations. *J. Phys. Chem. B*, 2018.

C. J. Hetherington, D. E. Harlov, and B. Buadzyń. Experimental metasomatism of monazite and xenotime: mineral stability, REE mobility and fluid composition. *Miner Petrol*, 99(3): 165–184, 2010.

P. Hohenberg and W. Kohn. Inhomogeneous electron gas. *Phys. Rev*, 136:B864–B871, 1964.

M. J. Hole, N. H. Trewin, and J. Still. Mobility of the high field strength, rare earth elements and yttrium during late diagenesis. *J. Geol. Soc.(London, U.K.)*, 149(5):689–692, 1992.

W. G. Hoover. Canonical dynamics: Equilibrium phase-space distributions. *Phys. Rev. A*, 31 (3):1695–1697, 1985.

E. Hückel and P. Debye. The theory of electrolytes: I. lowering of freezing point and related phenomena. *Phys. Z*, 24:185–206, 1923.

L. Hughes, R. Burgess, D. Chavrit, A. Pawley, R. Tartèse, G. Droop, C. J. Ballentine, and I. Lyon. Halogen behaviour in subduction zones: Eclogite facies rocks from the Western and Central Alps. *Geochim. Cosmochim. Acta*, 243:1–23, 2018.

G. Hummer, L. R. Pratt, and A. E. García. Free energy of ionic hydration. *J. Phys. Chem.*, 100 (4):1206–1215, 1996.

J. Hutter, M. Iannuzzi, F. Schiffmann, and J. VandeVondele. CP2K: atomistic simulations of condensed matter systems. *WIREs Comput. Mol. Sci.*, 4(1):15–25, 2014.

P. H. Hünenberger and J. A. McCammon. Ewald artifacts in computer simulations of ionic solvation and ion–ion interaction: A continuum electrostatics study. *J. Chem. Phys.*, 110(4): 1856–1872, 1999.

T. Ikeda, M. Hirata, and T. Kimura. Hydration structure of Y^{3+} and La^{3+} compared: an application of metadynamics. *J. Chem. Phys.*, 122(24):244507, 2005a.

T. Ikeda, M. Hirata, and T. Kimura. Hydration of Y^{3+} ion: a Car-Parrinello molecular dynamics study. *J. Chem. Phys.*, 122(2):024510, 2005b.

IUPAC. A report of IUPAC commission 1.2 on thermodynamics notation for states and processes, significance of the word "standard" in chemical thermodynamics, and remarks on commonly tabulated forms of thermodynamic functions. *The J. Chem. Thermodyn.*, 14(9): 805–815, 1982.

I. Ivanov, B. Chen, S. Raugei, and M. L. Klein. Relative pKa values from first-principles molecular dynamics: The case of histidine deprotonation. *J. Phys. Chem. B*, 110(12):6365–6371, 2006.

S. Jahn and P. M. Kowalski. Theoretical approaches to structure and spectroscopy of earth materials. *Rev. Mineral. Geochem.*, 78(1):691–743, 2014.

S. Jahn and C. Schmidt. Speciation in aqueous $MgSO_4$ fluids at high pressures and high temperatures from ab initio molecular dynamics and Raman spectroscopy. *J. Phys. Chem. B*, 114(47):15565–15572, 2010.

S. Jahn and B. Wunder. Lithium speciation in aqueous fluids at high P and T studied by ab initio molecular dynamics and consequences for Li-isotope fractionation between minerals and fluids. *Geochim. Cosmochim. Acta*, 73(18):5428–5434, 2009.

C. Jarzynski. Nonequilibrium Equality for Free Energy Differences. *Phys. Rev. Lett.*, 78(14): 2690–2693, 1997.

B. W. Jaskula. 2013 Minerals Yearbook: Beryllium. Technical report, USGS, 2013.

P. Jedlovszky, M. Mezei, and R. Vallauri. Comparison of polarizable and nonpolarizable models of hydrogen fluoride in liquid and supercritical states: A Monte Carlo simulation study. *J. Chem. Phys.*, 115(21):9883–9894, 2001.

G. Johansson and H. Wakita. X-ray investigation of the coordination and complex formation of lanthanoid ions in aqueous perchlorate and selenate solutions. *Inorg. Chem.*, 24(19): 3047–3052, 1985.

T. John, R. Klemd, J. Gao, and C.-D. Garbe-Schönberg. Trace-element mobilization in slabs due to non steady-state fluid–rock interaction: Constraints from an eclogite-facies transport vein in blueschist (Tianshan, China). *Lithos*, 103(1):1–24, 2008.

T. John, M. Scambelluri, M. Frische, J. D. Barnes, and W. Bach. Dehydration of subducting serpentinite: Implications for halogen mobility in subduction zones and the deep halogen cycle. *Earth Planet. Sci. Lett.*, 308(1):65–76, 2011.

J. W. Johnson, E. H. Oelkers, and H. C. Helgeson. SUPCRT92: A software package for calculating the standard molal thermodynamic properties of minerals, gases, aqueous species, and reactions from 1 to 5000 bar and 0 to 1000°C. *Comput. and Geosci.*, 18(7):899–947, 1992.

R. Jonchiere, A. P. Seitsonen, G. Ferlat, A. M. Saitta, and R. Vuilleumier. Van der Waals effects in ab initio water at ambient and supercritical conditions. *J. Chem. Phys.*, 135(15):154503, 2011.

T. Joutsuka and K. Ando. Hydration structure in dilute hydrofluoric acid. *J. Phys. Chem. A*, 115(5):671–677, 2011.

B. S. Kamber, A. Ewart, K. D. Collerson, M. C. Bruce, and G. D. McDonald. Fluid-mobile trace element constraints on the role of slab melting and implications for Archaean crustal growth models. *Contrib. Mineral Petrol.*, 144(1):38–56, 2002.

T. Kawamoto. Hydrous phases and water transport in the subducting slab. *Rev. Mineral. Geochem.*, 62(1):273–289, 2006.

H. Keppler. Constraints from partitioning experiments on the composition of subduction-zone fluids. *Nature*, 380(6571):237–240, 1996.

H. Keppler. Fluids and trace element transport in subduction zones. *Am. Mineral*, 102(1):5–20, 2017.

J. Kielland. Individual activity coefficients of ions in aqueous solutions. *J. Am. Chem. Soc.*, 59 (9):1675–1678, 1937a.

J. Kielland. Chemical hydration numbers. *J. Chem. Educ.*, 14(9):412, 1937b.

F. W. Klein, P. Einarsson, and M. Wyss. The Reykjanes Peninsula, Iceland, earthquake swarm of September 1972 and its tectonic significance. *J. Geophys. Res.*, 82(5):865–888, 1977.

W. Koch and M. C. Holthausen. *A Chemist's Guide to Density Functional Theory 2. Edition*. John Wiley & Sons, Weinheim, 2. edition, 2001.

W. Kohn and L. J. Sham. Self-consistent equations including exchange and correlation effects. *Phys. Rev*, 140:A1133–A1138, 1965.

O. A. Koz'menko, B. I. Peshchevitsky, and V. Belevantsev. The solubility of bromellite in solutions of hydrogen fluoride at 300 °C. *Geochem. Int.*, 22:162–169, 1985.

O. A. Koz'menko, V. I. Belevantsev, and B. I. Peshchevitsky. The solubility of BeO in aqueous HF at 250 °C and 350 °C. *Geochem. Int.*, 24:135–138, 1987.

M. Krack. Pseudopotentials for H to Kr optimized for gradient-corrected exchange-correlation functionals. *Theor. Chem. Acc.*, 114(1-3):145–152, 2005.

M. Kreitmeir, H. Bertagnolli, J. J. Mortensen, and M. Parrinello. Ab initio molecular dynamics simulation of hydrogen fluoride at several thermodynamic states. *J. Chem. Phys.*, 118(8): 3639–3645, 2003.

S. Kumar, J. M. Rosenberg, D. Bouzida, R. H. Swendsen, and P. A. Kollman. Multidimensional free-energy calculations using the weighted histogram analysis method. *J. Comput. Chem*, 16(11):1339–1350, 1995.

I.-F. W. Kuo, C. J. Mundy, M. J. McGrath, J. I. Siepmann, J. VandeVondele, M. Sprik, J. Hutter, B. Chen, M. L. Klein, F. Mohamed, M. Krack, and M. Parrinello. Liquid water from first principles: Investifation of different sampling approaches. *J. Phys. Chem. B*, 108(34): 12990–12998, 2004.

J. Kynicky, M. P. Smith, and C. Xu. Diversity of rare earth deposits: The key example of china. *Elements*, 8(5):361–367, 2012.

K. Laasonen, M. Sprik, M. Parrinello, and R. Car. Ab initio liquid water. *J. Chem. Phys.*, 99 (11):9080–90899, 1993.

K. Laasonen, J. Larrucea, and A. Sillapää. Ab initio molecular dynamics study of a mixture of HF(aq) and HCl(aq). *J. Phys. Chem. B*, 110(25):12699–12706, 2006.

A. Laio and M. Parrinello. Escaping free-energy minima. *PNAS*, 99(20):12562–12566, 2002.

P. Lecumberri-Sanchez, M. Bouabdellah, and O. Zemri. Transport of rare earth elements by hydrocarbon-bearing brines: Implications for ore deposition and the use of REEs as fluid source tracers. *Chem. Geol.*, 226:84 – 106, 2018.

C. Lee, W. Yang, and R. G. Parr. Development of the Colle-Salvetti correlation-energy formula into a functional of the electron density. *Phys. Rev. B*, 37(2):785–789, 1988.

P. Lindqvist-Reis, K. Lamble, S. Pattanaik, I. Persson, and M. Sandström. Hydration of the yttrium(III) ion in aqueous solution. An X-ray diffraction and xafs structural study. *J. Phys. Chem. B*, 104(2):402–408, 2000.

W. T. Lindsay. Estimation of concentration quotients for ionic equilibria in high temperature water. The model substance approach. *Proc. Int. Water Conf., 41st (Pittsburgh, Pa, Oct. 20, 1980)*, pages 284–294, 1980.

X. Liu, X. Lu, R. Wang, and H. Zhou. In silico calculation of acidity constants of carbonic acid conformers. *J. Phys. Chem. A*, 114(49):12914–12917, 2010.

X. Liu, X. Lu, R. Wang, and E. Jan Meijer. Understanding hydration of Zn^{2+} in hydrothermal fluids with ab initio molecular dynamics. *PCCP*, 13(29):13305–13309, 2011.

X. Liu, X. Lu, R. Wang, and H. Zhou. First-principles molecular dynamics study of stepwise hydrolysis reactions of Y^{3+} cations. *Chem. Geol.*, 334:37–43, 2012.

Y. Liu, X. Mao, M. Liu, and L. Jiang. Impact of magnesium(II) on beryllium fluorides in solutions studied by 19F NMR spectroscopy. *Chin. J. Chem.*, 32(9):878–882, 2014.

A. Loges, A. A. Migdisov, T. Wagner, A. E. Williams-Jones, and G. Markl. An experimental study of the aqueous solubility and speciation of Y(III) fluoride at temperatures up to 250 °C. *Geochim. Cosmochim. Acta*, 123:403–415, 2013.

Y.-R. Luo and R. H. Byrne. The ionic strength dependence of rare earth and yttrium fluoride complexation at 25°C. *J. Solution Chem.*, 29(11):1089–1099, 2000.

Y.-R. Luo and R. H. Byrne. Yttrium and rare earth element complexation by chloride ions at 25°C. *J. Solution Chem.*, 30(9):837–845, 2001.

Y.-R. Luo and R. H. Byrne. The influence of ionic strength on yttrium and rare earth element complexation by fluoride ions in $NaClO_4$, $NaNO_3$ and NaCl solutions at 25 °C. *J. Solution Chem.*, 36(6):673, 2007.

M. V Borisov and Y. Shvarov. Thermodynamics of geochemical processes. *Moscow: Moscow State University Press*, 1992.

M. Mangold, L. Rolland, F. Costanzo, M. Sprik, M. Sulpizi, and J. Blumberger. Absolute pKa values and solvation structure of amino acids from density functional based molecular dynamics simulation. *J. Chem. Theory Comput.*, 7(6):1951–1961, 2011.

C. Manning. The chemistry of subduction-zone fluids. *Earth Planet. Sci. Lett.*, 223(1-2):1–16, 2004.

C. Manning and L. Aranovich. Brines at high pressure and temperature: Thermodynamic, petrologic and geochemical effects. *Precambrian Res.*, 253:6–16, 2014.

C. E. Manning. Thermodynamic modeling of fluid-rock interaction at mid-crustal to upper-mantle conditions. *Rev. Mineral. Geochem.*, 76(1):135–164, 2013.

C. E. Manning. Fluids of the lower crust: Deep is different. *Annu. Rev. Earth Planet Sci.*, 46 (1):67–97, 2018.

C. E. Manning, E. L. Shock, and D. A. Sverjensky. The chemistry of carbon in aqueous fluids at crustal and upper-mantle conditions: Experimental and theoretical constraints. *Rev. Mineral. Geochem.*, 75(1):109–148, 2013.

D. Mantegazzi, C. Sanchez-Valle, and T. Driesner. Thermodynamic properties of aqueous NaCl solutions to 1073 K and 4.5 GPa, and implications for dehydration reactions in subducting slabs. *Geochim. Cosmochim. Acta*, 121(0):263 – 290, 2013.

Y. Marcus. Ionic radii in aqueous solutions. *Chem. Rev.*, 88(8):1475–1498, 1988.

A. E. Mark, S. P. van Helden, P. E. Smith, L. H. M. Janssen, and W. F. van Gunsteren. Convergence properties of free energy calculations: α–Cyclodextrin complexes as a case study. *J. Am. Chem. Soc.*, 116(14):6293–6302, 1994.

G. Markl and K. Bucher. Composition of fluids in the lower crust inferred from metamorphic salt in lower crustal rocks. *Nature*, 391(6669):781–783, 1998.

G. Markl and J. C. Schumacher. Spatial variations in temperature and composition of greisen-forming fluids; an example from the Variscan Triberg granite complex, Germany. *Econ. Geol.*, 91(3):576–589, 1996.

H. R. Marschall, R. Altherr, and L. Rüpke. Squeezing out the slab — modelling the release of Li, Be and B during progressive high-pressure metamorphism. *Chem. Geol.*, 239(3):323–335, 2007.

W. L. Marshall and E. U. Franck. Ion product of water substance, 0–1000 °C, 1–10,000 bars New International Formulation and its background. *J. Phys. Chem. Ref. Data*, 10(2):295–304, 1981.

D. Marx and J. Hutter. Ab-initio molecular dynamics: Theory and implementation. In J. Grotendorst, editor, *Modern Methods and Algorithms of Quantum Chemistry*, NIC, pages 301–449. Forschungszentrum Jülich, I edition, 2000.

D. Marx and J. Hutter. *Ab Initio Molecular Dynamics:Basic Theory and Advanced Methods*. Cambridge University Press, 2012.

D. Marx, M. Sprik, and M. Parrinello. Ab initio molecular dynamics of ion solvation. The case of Be^{2+} in water. *Chem. Phy. Lett.*, 273(5–6):360–366, 1997.

O. Matsuoka, E. Clementi, and M. Yoshimine. CI study of the water dimer potential surface. *J. Chem. Phys.*, 64(4):1351–1361, 1976.

R. A. Mayanovic, S. Jayanetti, A. J. Anderson, W. A. Bassett, and I. Chou. Comparison between Yb^{3+} and Y^{3+} ion association with the Cl^{-} ion in hydrothermal solutions: Evidence from XAFS measurements on rare earth aqueous solutions at up to 500 °C and 270 MPa. *AGU Spring Meeting Abstracts*, 22:M22A–12, 2002.

R. A. Mayanovic, A. J. Anderson, W. A. Bassett, and I.-M. Chou. Steric hindrance and the enhanced stability of light rare-earth elements in hydrothermal fluids. *Am. Mineral*, 94(10): 1487–1490, 2009.

R. S. McGary, R. L. Evans, P. E. Wannamaker, J. Elsenbeck, and S. Rondenay. Pathway from subducting slab to surface for melt and fluids beneath Mount Rainier. *Nature*, 511(7509): 338–340, 2014.

J. McPhie, V. Kamenetsky, S. Allen, K. Ehrig, A. Agangi, and A. Bath. The fluorine link between a supergiant ore deposit and a silicic large igneous province. *Geology*, 39(11): 1003–1006, 2011.

Y. Mei, D. M. Sherman, W. Liu, and J. Brugger. Ab initio molecular dynamics simulation and free energy exploration of copper(I) complexation by chloride and bisulfide in hydrothermal fluids. *Geochim. Cosmochim. Acta*, 102:45–64, 2013.

Y. Mei, W. Liu, D. M. Sherman, and J. Brugger. Metal complexation and ion hydration in low density hydrothermal fluids: Ab initio molecular dynamics simulation of Cu(I) and Au(I) in chloride solutions (25–1000 °C, 1–5000 bar). *Geochim. Cosmochim. Acta*, 131:196–212, 2014.

Y. Mei, D. M. Sherman, W. Liu, B. Etschmann, D. Testemale, and J. Brugger. Zinc complexation in chloride-rich hydrothermal fluids (25–600 °C): A thermodynamic model derived from ab initio molecular dynamics. *Geochim. Cosmochim. Acta*, 150:265–284, 2015.

Y. Mei, B. Etschmann, W. Liu, D. M. Sherman, D. Testemale, and J. Brugger. Speciation and thermodynamic properties of zinc in sulfur-rich hydrothermal fluids: Insights from ab initio molecular dynamics simulations and X-ray absorption spectroscopy. *Geochim. Cosmochim. Acta*, 179:32–52, 2016.

Y. Mei, W. Liu, J. Brugger, D. M. Sherman, and J. D. Gale. The dissociation mechanism and thermodynamic properties of HCl(aq) in hydrothermal fluids (to 700 °C, 60,kbar) by ab initio molecular dynamics simulations. *Geochim. Cosmochim. Acta*, 226:84 – 106, 2018.

R. E. Mesmer and C. F. Baes. Fluoride complexes of beryllium(II) in aqueous media. *Inorg. Chem.*, 8(3):618–626, 1969.

R. E. Mesmer, W. L. Marshall, D. A. Palmer, J. M. Simonson, and H. F. Holmes. Thermodynamics of aqueous association and ionization reactions at high temperatures and pressures. *J Solution Chem*, 17(8):699–718, 1988.

A. Migdisov, A. E. Williams-Jones, J. Brugger, and F. A. Caporuscio. Hydrothermal transport, deposition, and fractionation of the REE: Experimental data and thermodynamic calculations. *Chem. Geol.*, 439:13–42, 2016.

A. Migdisov, X. Guo, H. Nisbet, H. Xu, and A. E. Williams-Jones. Fractionation of REE, U, and Th in natural ore-forming hydrothermal systems: Thermodynamic modeling. *The J. Chem. Thermodyn.*, 128:305–319, 2019.

A. A. Migdisov and A. E. Williams-Jones. Hydrothermal transport and deposition of the rare earth elements by fluorine-bearing aqueous liquids. *Miner. Depos*, 49(8):987–997, 2014.

A. A. Migdisov, A. E. Williams-Jones, and T. Wagner. An experimental study of the solubility and speciation of the Rare Earth Elements (III) in fluoride- and chloride-bearing aqueous solutions at temperatures up to 300 °C. *Geochim. Cosmochim. Acta*, 73(23):7087–7109, 2009.

J.-F. Montreuil, E. G. Potter, L. Corriveau, and W. J. Davis. Element mobility patterns in magnetite-group IOCG systems: The Fab IOCG system, Northwest Territories, Canada. *Ore. Geol. Rev.*, 72:562–584, 2016.

S. J. Moore, W. D. Carlson, and M. A. Hesse. Origins of yttrium and rare earth element distributions in metamorphic garnet. *J. Metamorph. Geol.*, 31(6):663–689, 2013.

J. D. Morris, W. P. Leeman, and F. Tera. The subducted component in island arc lavas: constraints from Be isotopes and B–Be systematics. *Nature*, 344(6261):31–36, 1990.

R. Mosebach. Die hydrothermale Löslichkeit des Quarzes als heterogenes Gleichgewicht. *Neues Jahrb. Mineral. Abh.*, 87:351–388, 1955.

J. L. Munoz. F-OH and Cl-OH exchange in micas with applications to hydrothermal ore deposits. *Rev. Mineral. Geochem.*, 13(1):469–493, 1984.

R. T. Myers. The strength of the hydrohalic acids. *J. Chem. Educ.*, 53(1):17, 1976.

B. Mysen. Aqueous fluids as transport medium at high pressure and temperature: Ti^{4+} solubility, solution mechanisms, and fluid composition. *Chem. Geol.*, 2018.

N. Métrich and P. J. Wallace. Volatile Abundances in Basaltic Magmas and Their Degassing Paths Tracked by Melt Inclusions. *Rev. Mineral. Geochem.*, 69(1):363–402, 2008.

V. B. Naumov, V. A. Dorofeev, and O. F. Mironova. Physicochemical parameters of the formation of hydrothermal deposits: A fluid inclusion study. I. Tin and tungsten deposits. *Geochem. Int.*, 49(10):1002, 2011.

R. C. Newton and C. E. Manning. Role of saline fluids in deep-crustal and upper-mantle metasomatism: insights from experimental studies. *Geofluids*, 10(1-2):58–72, 2010.

R. C. Newton, L. Y. Aranovich, E. C. Hansen, and B. A. Vandenheuvel. Hypersaline fluids in Precambrian deep-crustal metamorphism. *Precambrian Res.*, 91(1):41–63, 1998.

S. Nosé. A unified formulation of the constant temperature molecular dynamics methods. *J. Chem. Phys.*, 81(1):511–519, 1984.

J. Näslund, P. Lindqvist-Reis, I. Persson, and M. Sandström. Steric effects control the structure of the solvated lanthanum(III) ion in aqueous, dimethyl sulfoxide, and N,N'-dimethylpropyleneurea solution. An exafs and large-angle X-ray scattering study. *Inorg. Chem.*, 39(18):4006–4011, 2000.

E. H. Oelkers, P. Bénézeth, and G. S. Pokrovski. Thermodynamic databases for water-rock interaction. *Rev. Mineral. Geochem.*, 70(1):1–46, 2009.

E. Ohtani and K. D. Litasov. The effect of water on mantle phase transitions. *Rev. Mineral. Geochem.*, 62(1):397–420, 2006.

D. Pan, L. Spanu, B. Harrison, D. A. Sverjensky, and G. Galli. Dielectric properties of water under extreme conditions and transport of carbonates in the deep Earth. *PNAS*, 110(17): 6646–6650, 2013.

Y. Pan and M. E. Fleet. Rare earth element mobility during prograde granulite facies metamorphism: significance of fluorine. *Contrib. Mineral. Petrol.*, 123(3):251–262, 1996.

J. M. Park, A. Laio, M. Iannuzzi, and M. Parrinello. Dissociation mechanism of acetic acid in water. *J. Am. Chem. Soc.*, 128(35):11318–11319, 2006.

L. Pauling. Why is hydrofluoric acid a weak acid? An answer based on a correlation of free energies, with electronegativities. *J. Chem. Educ.*, 33(1):16, 1956.

L. Pauling. *The Nature of the Chemical Bond and the Structure of Molecules and Crystals: An Introduction to Modern Structural Chemistry*. Cornell University Press, 1960. ISBN 978-0-8014-0333-0.

J. P. Perdew and A. Ruzsinszky. Density functional theory of electronic structure: A short course for mineralogists and geophysicists. *Rev. Mineral. Geochem.*, 71(1):1–18, 2010.

J. P. Perdew and Y. Wang. Accurate and simple analytic representation of the electron-gas correlation energy. *Phys. Rev. B*, 45(23):13244–13249, 1992.

J. P. Perdew, K. Burke, and M. Ernzerhof. Generalized gradient approximation made simple. *Phys. Rev. Lett.*, 77(18):3865–3868, 1996.

L. R. Pestana, N. Mardirossian, M. Head-Gordon, and T. Head-Gordon. Ab initio molecular dynamics simulations of liquid water using high quality meta-GGA functionals. *Chem. Sci.*, 8(5):3554–3565, 2017.

D. Petrović, I. Jakovljević, L. Joksović, K. M. Szecsenyi, and P. Đurđević. Study of the hydrolytic properties of the trivalent Y-ion in chloride medium. *Polyhedron*, 105:1–11, 2016.

A. Philpotts and J. Ague. *Principles of Igneous and Metamorphic Petrology*. Cambridge University Press, Cambridge, UK ; New York, 2 edition, 2009.

P. M. Piaggi, O. Valsson, and M. Parrinello. Enhancing Entropy and Enthalpy Fluctuations to Drive Crystallization in Atomistic Simulations. *Phys. Rev. Lett.*, 119(1):015701, 2017.

F. Pietrucci. Strategies for the exploration of free energy landscapes: Unity in diversity and challenges ahead. *Rev. Phys.*, 2:32–45, 2017.

F. Pietrucci, J. C. Aponte, R. Starr, A. Pérez-Villa, J. E. Elsila, J. P. Dworkin, and A. M. Saitta. Hydrothermal decomposition of amino acids and origins of prebiotic meteoritic organic compounds. *ACS Earth Space Chem.*, 2(6):588–598, 2018.

K. S. Pitzer. Characteristics of very concentrated aqueous solutions. *Phys. Chem. Earth*, 13-14: 249–272, 1981.

K. S. Pitzer. Dielectric constant of water at very high temperature and pressure. *PNAS*, 80(14): 4575–4576, 1983.

K. S. Pitzer. A thermodynamic model for aqueous solutions of liquid-like density. Technical Report LBL-23554; CONF-871014-1, Lawrence Berkeley Lab., CA (USA), 1987.

K. S. Pitzer. *Activity Coefficients in Electrolyte Solutions*. CRC Press, 1991.

A. V. Plyasunov and I. Grenthe. The temperature dependence of stability constants for the formation of polynuclear cationic complexes. *Geochim. Cosmochim. Acta*, 58(17):3561–3582, 1994.

G. S. Pokrovski, A. Y. Borisova, and A. Y. Bychkov. Speciation and transport of metals and metalloids in geological vapors. *Rev. Mineral. Geochem.*, 76(1):165–218, 2013.

M. Portnyagin, K. Hoernle, P. Plechov, N. Mironov, and S. Khubunaya. Constraints on mantle melting and composition and nature of slab components in volcanic arcs from volatiles (H_2O, S, Cl, F) and trace elements in melt inclusions from the Kamchatka Arc. *Earth Planet. Sci. Lett.*, 255(1):53–69, 2007.

A. Putnis and T. John. Replacement processes in the Earth's crust. *Elements*, 6(3):159–164, 2010.

P. Pyykko and J. P. Desclaux. Relativity and the periodic system of elements. *Acc. Chem. Res.*, 12(8):276–281, 1979. ISSN 0001-4842.

A. Pérez de Alba Ortíz, A. Tiwari, R. C. Puthenkalathil, and B. Ensing. Advances in enhanced sampling along adaptive paths of collective variables. *J. Chem. Phys.*, 149(7):072320, 2018.

J. F. Rapp, S. Klemme, I. B. Butler, and S. L. Harley. Extremely high solubility of rutile in chloride and fluoride-bearing metamorphic fluids: An experimental investigation. *Geology*, 38(4):323–326, 2010.

H. Resat and M. Mezei. Studies on free energy calculations. I. Thermodynamic integration using a polynomial path. *J. Chem. Phys.*, 99(8):6052–6061, 1993.

F. G. Reyf. Immiscible phases of magmatic fluid and their relation to Be and Mo mineralization at the Yermakovka F–Be deposit, Transbaikalia, Russia. *Chem. Geol.*, 210(1–4):49–71, 2004.

F. G. Reyf. Alkaline granites and Be (phenakite-bertrandite) mineralization: An example of the Orot and Ermakovka deposits. *Geochem. Int.*, 46(3):213–232, 2011.

F. G. Reyf and Y. M. Ishkov. Be-bearing sulfate-fluoride brine: A product of residual pegmatite distillation in an alkali granite intrusion, Yermakovka F-Be deposit, Transbaikalia. *Geochem. Int.*, 37(10):985–999, 1999.

A. C. F. Ribeiro, M. A. Esteso, V. M. M. Lobo, H. D. Burrows, A. M. Amado, A. M. Amorim da Costa, A. J. F. N. Sobral, E. F. G. Azevedo, and M. A. F. Ribeiro. Mean distance of closest approach of ions: Sodium salts in aqueous solutions. *J. Mol. Liq*, 128(1–3):134–139, 2006.

A. C. F. Ribeiro, M. C. F. Barros, A. J. F. N. Sobral, V. M. M. Lobo, and M. A. Esteso. Mean distance of closest approach of alkaline-earth metals ions in aqueous solutions: Experimental and theoretical calculations. *J. Mol. Liq*, 156(2–3):124–127, 2010.

C. K. Richardson and H. D. Holland. The solubility of fluorite in hydrothermal solutions, an experimental study. *Geochim. Cosmochim. Acta*, 43(8):1313–1325, 1979.

J. Ridley. *Ore Deposit Geology*. Cambridge University Press, Cambridge, 2013.

B. Roux. The calculation of the potential of mean force using computer simulations. *Comput. Phys. Commun.*, 91(1):275–282, 1995.

V. Rozsa, D. Pan, F. Giberti, and G. Galli. Ab initio spectroscopy and ionic conductivity of water under Earth mantle conditions. *PNAS*, 115(27):6952–6957, 2018.

J. R. Ruaya. Estimation of instability constants of metal chloride complexes in hydrothermal solutions up to 300°C. *Geochim. Cosmochim. Acta*, 52(8):1983–1996, 1988.

W. W. Rudolph, D. Fischer, G. Irmer, and C. C. Pye. Hydration of beryllium(II) in aqueous solutions of common inorganic salts. A combined vibrational spectroscopic and ab initio molecular orbital study. *Dalton Trans.*, pages 6513–6527, 2009.

L. Ruiz Pestana, O. Marsalek, T. E. Markland, and T. Head-Gordon. The quest for accurate liquid water properties from first principles. *J. Phys. Chem. Lett.*, 2018.

J.-P. Ryckaert, G. Ciccotti, and H. J. C. Berendsen. Numerical integration of the cartesian equations of motion of a system with constraints: molecular dynamics of n-alkanes. *J. Comput. Phys.*, 23(3):327–341, 1977.

B. N. Ryzhenko. Determination of the dissociation constant of hydrofluoric acid and the conditions for replacement of calcite by fluorite. *Geochem. Intl.*, 2:196–200, 1965.

B. N. Ryzhenko. Transport species and accumulation of chemical elements in hydrothermal fluids. *Geol. Ore Deposits*, 50(3):155–191, 2008.

B. N. Ryzhenko, I. Bryzgalin, M. Artmakina, M. Y. Spasenykh, and A. I. Shapkin. An electrostatic model for the electrolytic dissociation of inorganic substances dissolved in water. *Geochem. Int*, 9(22):138–143, 1985.

C. J. Sahle, C. Sternemann, C. Schmidt, S. Lehtola, S. Jahn, L. Simonelli, S. Huotari, M. Hakala, T. Pylkkänen, A. Nyrow, K. Mende, M. Tolan, K. Hämäläinen, and M. Wilke. Microscopic structure of water at elevated pressures and temperatures. *PNAS*, 110(16):6301–6306, 2013.

A. W. Sakti, Y. Nishimura, and H. Nakai. Rigorous pKa estimation of amine species using density-functional tight-binding-based metadynamics simulations. *J. Chem. Theory Comput.*, 14(1):351–356, 2018.

H. Sakuma and M. Ichiki. Electrical conductivity of NaCl-H_2O fluid in the crust. *J. Geophys. Res. Solid Earth*, 121(2):2015JB012219, 2016.

R. Sallet. Fluorine as a tool in the petrogenesis of quartz-bearing magmatic associations: applications of an improved F–OH biotite–apatite thermometer grid. *Lithos*, 50(1):241–253, 2000.

C. Sanchez-Valle. Structure and thermodynamics of subduction zone fluids from spectroscopic studies. *Rev. Mineral. Geochem.*, 76(1):265–309, 2013.

M. Scambelluri and P. Philippot. Deep fluids in subduction zones. *Lithos*, 55(1–4):213–227, 2001.

H. Schmidbaur. Recent contributions to the aqueous coordination chemistry of beryllium. *Coord. Chem. Rev*, 215(1):223–242, 2001.

C. Schmidt and I. Chou. Chapter 7: The hydrothermal diamond anvil cell (HDAC) for Raman spectroscopic studies of geological fluids at high pressures and temperatures. In J. Dubessy, M.-C. Caumon, F. Rull, and Mineralogical Society, editors, *Applications of Raman spectroscopy to Earth sciences and cultural heritage (EMU Notes in Mineralogy)*, volume 12. Mineralogical Society, 2012.

C. Schmidt, K. Rickers, D. H. Bilderback, and R. Huang. In situ synchrotron-radiation XRF study of REE phosphate dissolution in aqueous fluids to 800 °C. *Lithos*, 95(1):87–102, 2007a.

C. Schmidt, K. Rickers, D. H. Bilderback, and R. Huang. In situ synchrotron-radiation XRF study of REE phosphate dissolution in aqueous fluids to 800 °C. *Lithos*, 95(1):87–102, 2007b.

M. W. Schmidt and S. Poli. Experimentally based water budgets for dehydrating slabs and consequences for arc magma generation. *Earth Planet. Sci. Lett.*, 163(1):361–379, 1998.

E. Schreiner, N. N. Nair, and D. Marx. Influence of Extreme Thermodynamic Conditions and Pyrite Surfaces on Peptide Synthesis in Aqueous Media. *J. Am. Chem. Soc.*, 130(9): 2768–2770, 2008.

E. Schrödinger. Quantisierung als Eigenwertproblem. *Ann. Phys.*, 384(4):361–376, 1926.

N. E. Schultz, Y. Zhao, and D. G. Truhlar. Density Functionals for Inorganometallic and Organometallic Chemistry. *J. Phys. Chem. A*, 109(49):11127–11143, 2005.

T. P. Senftle, S. Hong, M. M. Islam, S. B. Kylasa, Y. Zheng, Y. K. Shin, C. Junkermeier, R. Engel-Herbert, M. J. Janik, H. M. Aktulga, T. Verstraelen, A. Grama, and A. C. T. van Duin. The ReaxFF reactive force-field: development, applications and future directions. *npj Comput. Mater.*, 2:15011, 2016.

T. M. Seward and T. Driesner. Chapter 5 - Hydrothermal solution structure: Experiments and computer simulations. In D. A. Palmer, R. Fernández-Prini, and A. H. Harvey, editors, *Aqueous Systems at Elevated Temperatures and Pressures*, pages 149–182. Academic Press, London, 2004.

T. M. Seward, C. M. B. Henderson, O. M. Suleimenov, and J. M. Charnock. Iodide Ion Hydration in Aqueous Solution to 360°C: Insight from XAS and Ab Initio MD. In *Goldschmidt Conference Abstracts*, 2013.

T. M. Seward, A. E. Williams-Jones, and A. A. Migdisov. 13.2 - The Chemistry of Metal Transport and Deposition by Ore-Forming Hydrothermal Fluids A2 - Holland, Heinrich D. In K. K. Turekian, editor, *Treatise on Geochemistry (Second Edition)*, pages 29–57. Elsevier, Oxford, 2014.

R. D. Shannon. Revised effective ionic radii and systematic studies of interatomic distances in halides and chalcogenides. *Acta. Crystallogr. A*, 32(5):751–767, 1976.

D. M. Sherman. Metal complexation and ion association in hydrothermal fluids: insights from quantum chemistry and molecular dynamics. *Geofluids*, 10(1-2):41–57, 2010.

Y. Shi, H. Scheiber, and R. Z. Khaliullin. Contribution of the covalent component of the hydrogen-bond network to the properties of liquid water. *J. Phys. Chem. A*, 122(37):7482–7490, 2018.

M. Shiga and M. E. Tuckerman. Finding Free-Energy Landmarks of Chemical Reactions. *J. Phys. Chem. Lett.*, pages 6207–6214, 2018.

K. Shmulovich, B. Yardley, and G. Gonchar, editors. *Fluids in the Crust: Equilibrium and transport properties*. Springer Netherlands, 1995.

E. L. Shock and H. C. Helgeson. Calculation of the thermodynamic and transport properties of aqueous species at high pressures and temperatures: Correlation algorithms for ionic species and equation of state predictions to 5 kb and 1000 °C. *Geochim. Cosmochim. Acta*, 52(8): 2009–2036, 1988.

E. L. Shock, H. C. Helgeson, and D. A. Sverjensky. Calculation of the thermodynamic and transport properties of aqueous species at high pressures and temperatures: Standard partial molal properties of inorganic neutral species. *Geochim. Cosmochim. Acta*, 53(9):2157–2183, 1989.

E. L. Shock, E. H. Oelkers, J. W. Johnson, D. A. Sverjensky, and H. C. Helgeson. Calculation of the thermodynamic properties of aqueous species at high pressures and temperatures. Effective electrostatic radii, dissociation constants and standard partial molal properties to 1000 °C and 5 kbar. *J. Chem. Soc., Faraday Trans.*, 88(6):803–826, 1992.

E. L. Shock, D. C. Sassani, M. Willis, and D. A. Sverjensky. Inorganic species in geologic fluids: Correlations among standard molal thermodynamic properties of aqueous ions and hydroxide complexes. *Geochim. Cosmochim. Acta*, 61(5):907–950, 1997.

D. Sholl and J. A. Steckel. *Density Functional Theory: A Practical Introduction*. Wiley, 2009.

Y. Shvarov. A suite of programs, OptimA, OptimB, OptimC, and OptimS compatible with the Unitherm database, for deriving the thermodynamic properties of aqueous species from solubility, potentiometry and spectroscopy measurements. *Appl. Geochem.*, 55:17–27, 2015.

Y. V. Shvarov. HCh: New potentialities for the thermodynamic simulation of geochemical systems offered by windows. *Geochem. Int.*, 46(8):834, 2008.

Y. Y. Shvarov and E. Bastrakov. HCh: A Software Package for Geochemical Equilibrium Modeling: User's Guide (AGSO RECORD 1999/Y). *Australian Geological Survey Organsisation*, page 61, 1999.

C. Simon and M. L. Klein. Ab initio molecular dynamics simulation of a water–hydrogen fluoride equimolar mixture. *Chem. Phys. Chem*, 6(1):148–153, 2005.

R. Sinmyo and H. Keppler. Electrical conductivity of NaCl-bearing aqueous fluids to 600 °C and 1 GPa. *Contrib. Mineral. Petrol.*, 172(1):4, 2016.

H. C. Sorby. Proceedings of Societies. *Trans. Am. Microsc. Soc.*, 6(1):190–194, 1858.

M. Sprik and G. Ciccotti. Free energy from constrained molecular dynamics. *J. Chem. Phys.*, 109(18):7737–7744, 1998.

M. Sprik, J. Hutter, and M. Parrinello. Ab initio molecular dynamics simulation of liquid water:Comparison of three gradient-corrected density functionals. *J. Chem. Phys.*, 105(3): 1142–1152, 1996.

A. G. Stack, P. Raiteri, and J. D. Gale. Accurate rates of the complex mechanisms for growth and dissolution of minerals using a combination of rare-event theories. *J. Am. Chem. Soc.*, 134(1):11–14, 2012.

J. Stefanski, C. Schmidt, and S. Jahn. Aqueous sodium hydroxide (NaOH) solutions at high pressure and temperature: insights from in situ Raman spectroscopy and ab initio molecular dynamics simulations. *PCCP*, 20(33):21629–21639, 2018.

A. Stirling and I. Pápai. H_2CO_3 Forms via HCO_3^- in Water. *J. Phys. Chem. B*, 114(50): 16854–16859, 2010.

R. H. Stokes and R. A. Robinson. Ionic Hydration and Activity in Electrolyte Solutions. *J. Am. Chem. Soc.*, 70(5):1870–1878, 1948.

T. P. Straatsma and H. J. C. Berendsen. Free energy of ionic hydration: Analysis of a thermodynamic integration technique to evaluate free energy differences by molecular dynamics simulations. *J. Chem. Phys.*, 89(9):5876–5886, 1988.

S. M. Straub and G. D. Layne. The systematics of chlorine, fluorine, and water in Izu arc front volcanic rocks: Implications for volatile recycling in subduction zones. *Geochim. Cosmochim. Acta*, 67(21):4179–4203, 2003.

Q. Sun, Q. Wang, and D. Ding. Hydrogen Bonded Networks in Supercritical Water. *J. Phys. ChemB*, 118(38):11253–11258, 2014.

S.-s. Sun and W. F. McDonough. Chemical and isotopic systematics of oceanic basalts: implications for mantle composition and processes. *J. Geol. Soc. (London, U.K.)*, 42(1):313–345, 1989.

H. Svensen, B. Jamtveit, D. A. Banks, and H. Austrheim. Halogen contents of eclogite facies fluid inclusions and minerals: Caledonides, western Norway. *J. Metamorph. Geol.*, 19(2): 165–178, 2008.

D. A. Sverjensky. Calculation of the thermodynamic properties of aqueous species and the solubilities of minerals in supercritical electrolyte solutions. *Rev. Mineral. Geochem.*, 17(1): 177–209, 1987.

D. A. Sverjensky. Thermodynamic modelling of fluids from surficial to mantle conditions. *J. Geol. Soc. (London, U.K.)*, 176(2):348–374, 2019.

D. A. Sverjensky, E. L. Shock, and H. C. Helgeson. Prediction of the thermodynamic properties of aqueous metal complexes to 1000°C and 5 kb. *Geochim. Cosmochim. Acta*, 61(7):1359–1412, 1997.

D. A. Sverjensky, B. Harrison, and D. Azzolini. Water in the deep Earth: The dielectric constant and the solubilities of quartz and corundum to 60 kb and 1200 °C. *Geochim. Cosmochim. Acta*, 129:125–145, 2014.

R. B. Symonds, W. I. Rose, G. J. S. Bluth, and T. M. Gerlach. Volcanic-gas studies; methods, results, and applications. *Rev. Mineral. Geochem.*, 30(1):1–66, 1994.

F. V. Syromyatnikov, A. P. Makarova, and I. Kupriyanova. Experimental studies of stability of beryl and phenacite in aqueous solutions. *Intl. Geol. Rev.*, 14:837–839, 1972.

B. R. Tagirov and T. M. Seward. Hydrosulfide/sulfide complexes of zinc to 250 °C and the thermodynamic properties of sphalerite. *Chem. Geol.*, 269(3–4):301–311, 2010.

B. R. Tagirov, O. N. Filimonova, A. L. Trigub, N. N. Akinfiev, M. S. Nickolsky, K. O. Kvashnina, D. A. Chareev, and A. V. Zotov. Platinum transport in chloride-bearing fluids and melts: insights from in situ X-ray absorption spectroscopy and thermodynamic modeling. *Geochim. Cosmochim. Acta*, 2019a.

B. R. Tagirov, A. L. Trigub, O. N. Filimonova, K. O. Kvashnina, M. S. Nickolsky, S. Lafuerza, and D. A. Chareev. Gold transport in hydrothermal chloride-bearing fluids: Insights from in situ X-ray absorption spectroscopy and ab initio molecular dynamics. *ACS Earth Space Chem.*, 3(2):240–261, 2019b.

M. Tang, K. Chen, and R. L. Rudnick. Archean upper crust transition from mafic to felsic marks the onset of plate tectonics. *Science*, 351(6271):372–375, 2016.

T. P. Taylor, M. Ding, D. S. Ehler, T. M. Foreman, J. P. Kaszuba, and N. N. Sauer. Beryllium in the environment: A review. *J. Environ. Sci. Health., Part A*, 38(2):439–469, 2003.

R. Thomas and P. Davidson. Hambergite-rich melt inclusions in morganite crystals from the Muiane pegmatite, Mozambique and some remarks on the paragenesis of hambergite. *Miner. Petrol.*, 100(3-4):227–239, 2010.

R. Thomas, P. Davidson, and E. Badanina. A melt and fluid inclusion assemblage in beryl from pegmatite in the Orlovka amazonite granite, East Transbaikalia, Russia: implications for pegmatite-forming melt systems. *Miner Petrol.*, 96(3-4):129–140, 2009.

R. Thomas, J. D. Webster, and P. Davidson. Be-daughter minerals in fluid and melt inclusions: implications for the enrichment of Be in granite–pegmatite systems. *Contrib. Mineral Petrol.*, 161(3):483–495, 2010.

R. Thomas, P. Davidson, and C. Schmidt. Extreme alkali bicarbonate- and carbonate-rich fluid inclusions in granite pegmatite from the Precambrian Rønne granite, Bornholm Island, Denmark. *Contrib. Mineral. Petrol.*, 161(2):315–329, 2011.

T. Todorova, P. H. Hünenberger, and J. Hutter. Car–Parrinello Molecular Dynamics Simulations of CaCl2 Aqueous Solutions. *J. Chem. Theory Comput.*, 4(5):779–789, 2008.

J. Touret. The Significance of Fluid Inclusions in Metamorphic Rocks. In D. G. Fraser, editor, *Thermodynamics in Geology*, NATO Advanced Study Institutes Series, pages 203–227. Springer Netherlands, 1977.

P. Tremaine and H. Arcis. Solution calorimetry under hydrothermal conditions. *Rev. Mineral. Geochem.*, 76(1):219–263, 2013.

P. Tremaine, K. Zhang, P. Bénézeth, and C. Xiao. Chapter 13 - Ionization equilibria of acids and bases under hydrothermal conditions. In D. A. Palmer, R. Fernández-Prini, and A. H. Harvey, editors, *Aqueous Systems at Elevated Temperatures and Pressures*, pages 441–492. Academic Press, London, 2004.

G. A. Tribello, M. Bonomi, D. Branduardi, C. Camilloni, and G. Bussi. PLUMED 2: New feathers for an old bird. *Comput. Phys. Commun.*, 185(2):604–613, 2014.

V. Trommsdorff, G. Skippen, and P. Ulmer. Halite and sylvite as solid inclusions in high-grade metamorphic rocks. *Contr. Mineral. and Petrol.*, 89(1):24–29, 1985.

P. Tropper and C. E. Manning. The solubility of fluorite in H_2O and H_2O–NaCl at high pressure and temperature. *Chem. Geol.*, 242(3–4):299–306, 2007.

P. Tropper, C. E. Manning, and D. E. Harlov. Solubility of $CePO_4$ monazite and YPO_4 xenotime in H_2O and H_2O–NaCl at 800°C and 1 GPa: Implications for REE and Y transport during high-grade metamorphism. *Chem. Geol.*, 282(1):58–66, 2011.

P. Tropper, C. E. Manning, and D. E. Harlov. Experimental determination of $CePO_4$ and YPO_4 solubilities in H_2O–NaF at 800°C and 1 GPa: implications for rare earth element transport in high-grade metamorphic fluids. *Geofluids*, 13(3):372–380, 2013.

A. Tsay, Z. Zajacz, and C. Sanchez-Valle. Efficient mobilization and fractionation of rare-earth elements by aqueous fluids upon slab dehydration. *Earth Planet. Sci. Lett.*, 398:101–112, 2014.

A. Tsay, Z. Zajacz, P. Ulmer, and C. Sanchez-Valle. Mobility of major and trace elements in the eclogite-fluid system and element fluxes upon slab dehydration. *Geochim. Cosmochim. Acta*, 198:70–91, 2017.

O. Tschauner, S. Huang, E. Greenberg, V. B. Prakapenka, C. Ma, G. R. Rossman, A. H. Shen, D. Zhang, M. Newville, A. Lanzirotti, and K. Tait. Ice-VII inclusions in diamonds: Evidence for aqueous fluid in Earth's deep mantle. *Science*, 359(6380):1136–1139, 2018.

M. E. Tuckerman and M. Parrinello. Integrating the Car–Parrinello equations. I. Basic integration techniques. *J. Chem. Phys.*, 101(2):1302–1315, 1994.

M. E. Tuckerman, P. J. Ungar, T. von Rosenvinge, and M. L. Klein. Ab initio molecular dynamics simulations. *J. Phys. Chem.*, 100(31):12878–12887, 1996.

M. E. Tuckerman, D. Marx, M. L. Klein, and M. Parrinello. On the quantum nature of the shared proton in hydrogen bonds. *Science*, 275(5301):817–820, 1997.

A. K. Tummanapelli and S. Vasudevan. Dissociation constants of weak acids from ab initio molecular dynamics using metadynamics: Influence of the inductive effect and hydrogen bonding on pKa values. *J. Phys. Chem. B*, 118(47):13651–13657, 2014.

A. K. Tummanapelli and S. Vasudevan. Estimating successive pKa values of polyprotic acids from ab initio molecular dynamics using metadynamics: the dissociation of phthalic acid and its isomers. *PCCP*, 17(9):6383–6388, 2015a.

A. K. Tummanapelli and S. Vasudevan. Ab initio MD simulations of the Brønsted acidity of glutathione in aqueous solutions: Predicting pKa shifts of the cysteine residue. *J. Phys. Chem. B*, 119(49):15353–15358, 2015b.

P. Černý. Mineralogy of Beryllium in Granitic Pegmatites. *Rev. Mineral. Geochem.*, 50(1): 405–444, 2002.

P. Ulmer and V. Trommsdorff. Serpentine stability to mantle depths and subduction-related magmatism. *Science*, 268(5212):858–861, 1995.

K. Vala Ragnarsdottir, E. H. Oelkers, D. M. Sherman, and C. R. Collins. Aqueous speciation of yttrium at temperatures from 25 to 340°C at P_{sat}: an in situ EXAFS study. *Chem. Geol.*, 151(1–4):29–39, 1998.

O. Valsson, P. Tiwary, and M. Parrinello. Enhancing Important Fluctuations: Rare Events and Metadynamics from a Conceptual Viewpoint. *Annu. Rev. Phys. Chem.*, 67(1):159–184, 2016.

A. M. Van den Kerkhof and U. F. Hein. Fluid inclusion petrography. *Lithos*, 55(1):27–47, 2001.

A. C. T. van Duin, S. Dasgupta, F. Lorant, and W. A. Goddard. ReaxFF: A reactive force field for hydrocarbons. *J. Phys. Chem. A*, 105(41):9396–9409, 2001.

J. van Sijl, N. L. Allan, G. R. Davies, and W. v. Westrenen. Molecular modelling of rare earth element complexation in subduction zone fluids. *Geochim. Cosmochim. Acta*, 73(13): 3934–3947, 2009.

J. van Sijl, N. L. Allan, G. R. Davies, and W. van Westrenen. Titanium in subduction zone fluids: First insights from ab initio molecular metadynamics simulations. *Geochim. Cosmochim. Acta*, 74(9):2797–2810, 2010.

J. VandeVondele, F. Mohamed, M. Krack, J. Hutter, M. Sprik, and M. Parrinello. The influence of temperature and density functional models in ab initio molecular dynamics simulation of liquid water. *J. Chem. Phys.*, 122(1):014515, 2004.

W. Wagner and A. Pruß. The IAPWS formulation 1995 for the thermodynamic properties of ordinary water substance for general and scientific use. *J. Phys. Chem. Ref. Data*, 31(2): 387–535, 2002.

S. L. Wallen, B. J. Palmer, D. M. Pfund, J. L. Fulton, M. Newville, Y. Ma, and E. A. Stern. Hydration of bromide ion in supercritical water: An X-ray absorption fine strucutre and molecular dynamics study. *J. Phys. Chem. A*, 101(50):9632–9640, 1997.

T. J. Webb. The free energy of hydration of ions and the eletrostriction of the solvent. *J. Am. Chem. Soc.*, 48(10):2589–2603, 1926.

C. F. Weber, E. C. Beahm, D. D. Lee, and J. S. Watson. A solubility model for aqueous solutions containing sodium, fluoride, and phosphate ions. *Ind. Eng. Chem. Res.*, 39(2):518–526, 2000.

H. K. Wedepohl. The composition of the continental crust. *Geochim. Cosmochim. Acta*, 59(7): 1217–1232, 1995.

B. Widom. Some topics in the theory of fluids. *J. Chem. Phys.*, 39(11):2808–2812, 1963.

A. E. Williams-Jones, I. M. Samson, and G. R. Olivo. The genesis of hydrothermal fluorite-REE deposits in the gallinas Mountains, New Mexico. *Econ. Geol.*, 95(2):327–341, 2000.

A. E. Williams-Jones, A. A. Migdisov, and I. M. Samson. Hydrothermal mobilisation of the rare earth elements – a tale of "Ceria" and "Yttria". *Elements*, 8(5):355–360, 2012.

P. L. Wincott and D. J. Vaughan. Spectroscopic studies of sulfides. *Rev. Mineral. Geochem.*, 61(1):181–229, 2006.

J. D. Winter. *Principles of Igneous and Metamorphic Petrology*. Pearson, New York, 2 edition edition, 2009.

T. J. Wolery and K. J. Jackson. Activity Coefficients in Aqueous Salt Solutions. In *Chemical Modeling of Aqueous Systems II*, number 416 in ACS Symposium Series, pages 16–29. ACS, 1990.

S. A. Wood. The aqueous geochemistry of the rare-earth elements and yttrium. *Chem. Geol.*, 88(1):99–125, 1990.

S. A. Wood. Theoretical prediction of speciation and solubility of beryllium in hydrothermal solution to 300°C at saturated vapor pressure: Application to bertrandite/phenakite deposits. *Ore. Geol. Rev.*, 7(4):249–278, 1992.

T. Worzewski, M. Jegen, H. Kopp, H. Brasse, and W. T. Castillo. Magnetotelluric image of the fluid cycle in the Costa Rican subduction zone. *Nat. Geosci.*, 4(2):108–111, 2011.

B. Wunder. Equilibrium experiments in the system MgO–SiO_2–H_2O (MSH): stability fields of clinohumite-OH [$Mg_9Si_4O_{16}(OH)_2$], chondrodite-OH [$Mg_5Si_2O_8(OH)_2$] and phase A ($Mg_7Si_2O_8(OH)_6$). *Contrib. Mineral Petrol.*, 132(2):111–120, 1998.

Y. Xing, B. Etschmann, W. Liu, Y. Mei, Y. Shvarov, D. Testemale, A. Tomkins, and J. Brugger. The role of fluorine in hydrothermal mobilization and transportation of Fe, U and REE and the formation of IOCG deposits. *Chem. Geol.*, 2018.

T. Yamaguchi, H. Ohtaki, E. Spohr, G. Pálinkás, K. Heinzinger, and M. M. Probst. Molecular dynamics and X-Ray diffraction study of aqueous beryllium(II) chloride solutions. *Z. Naturforsch. A*, 41(10):1175–1185, 1986.

Y. I. Yang, H. Niu, and M. Parrinello. Combining metadynamics and integrated tempering sampling. *J. Phys. Chem. Lett.*, pages 6426–6430, 2018.

B. W. D. Yardley. Apatite composition and the fugacities of HF and HCl in metamorphic fluids. *Mineral. Mag.*, 49(350):77–79, 1985.

B. W. D. Yardley and R. J. Bodnar. Fluids in the continental crust. *Geochem. perspect.*, 3(1), 2014.

W. Ye, C. Chen, Z. Wang, I.-H. Chu, and S. P. Ong. Deep neural networks for accurate predictions of crystal stability. *Nat. Commun.*, 9(1):3800, 2018.

K. Yui, M. Sakuma, and T. Funazukuri. Molecular dynamics simulation on ion-pair association of NaCl from ambient to supercritical water. *Fluid Phase Equilib.*, 297(2):227–235, 2010.

Z. Zhang and Z. Duan. Prediction of the PVT properties of water over wide range of temperatures and pressures from molecular dynamics simulation. *Phys. Earth Planet. Inter.*, 149(3–4): 335–354, 2005.

Z.-M. Zhang, K. Shen, W.-D. Sun, Y.-S. Liu, J. G. Liou, C. Shi, and J.-L. Wang. Fluids in deeply subducted continental crust: Petrology, mineral chemistry and fluid inclusion of UHP metamorphic veins from the Sulu orogen, eastern China. *Geochim. Cosmochim. Acta*, 72 (13):3200–3228, 2008.

Y. Zheng, R. Chen, Z. Xu, and S. Zhang. The transport of water in subduction zones. *Sci. China Earth Sci.*, 59(4):651–682, 2016.

Y.-F. Zheng, Q.-X. Xia, R.-X. Chen, and X.-Y. Gao. Partial melting, fluid supercriticality and element mobility in ultrahigh-pressure metamorphic rocks during continental collision. *Earth Sci. Rev.*, 107(3):342–374, 2011.

C. Zhu and D. A. Sverjensky. Partitioning of F-Cl-OH between minerals and hydrothermal fluids. *Geochim. Cosmochim. Acta*, 55(7):1837–1858, 1991.

K. Zimmer, Y. Zhang, P. Lu, Y. Chen, G. Zhang, M. Dalkilic, and C. Zhu. SUPCRTBL: A revised and extended thermodynamic dataset and software package of SUPCRT92. *Comput. and Geosci.*, 90, Part A:97–111, 2016.

APPENDIX

Numerical Implementation of the Thermodynamic Modeling

Equation of State

H_2O Equation of State IAPWS

Here the Python implementation of the IAPWS is used:

https://pypi.org/project/iapws/

http://www.iapws.org/release.html

H_2O Density Equation of State [Zhang and Duan, 2005]

```
import numpy as np
import matplotlib.pyplot as plt

def eos_density_zhang_duan2005(T,rho_in):
    """
    T in C and density in kg/m3, output  P in MPa
    EOS based on MD (SPCE)  data by Zhang and Duan (2005)
    EOS is given in Lee-Kesler-EOS form
    Function gives the density of pure H2O from 273.15 to 2000 K and 100
   MPa up to 20-30 GPa
    """
    T=T+273.15
    V=np.array(range(1*10**3,500*10**3))/10**3
    a1=3.49824207*10**-1
    a2=-2.91046273*10**0
    a3=2.00914688*10**0
    a4=1.12819964*10**-1
    a5=7.48997714*10**-1
    a6=-8.73207040*10**-1
    a7=1.70609505*10**-2
    a8=-1.46355822*10**-2
    a9=5.79768283*10**-2
    a10=-8.41246372*10**-4
    a11=4.95186474*10**-3
```

```
    a12=-9.16248538*10**-3
    a13=-1.00358152*10**-1
    a14=-1.82674744*10**-3
    gamma=1.05999998*10**-2
    Tc=647.25 #K
    Vc=55.9480373 #cm3 bar/K
    Tr=T/Tc
    R= 83.14467 #cm3 bar/(K mol)
    M=1.008+1.008+15.999 #g/mol
    B=a1+(a2/Tr**2)+(a3/Tr**3)
    C=a4+(a5/Tr**2)+(a6/Tr**3)
    D=a7+(a8/Tr**2)+(a9/Tr**3)
    E=a10+(a11/Tr**2)+(a12/Tr**3)
    F=a13/Tr
    G=a14*Tr
    Vr=V/Vc
    Z=1+(B/Vr)+(C/Vr**2)+(D/Vr**4)+(E/Vr**5)+((F/Vr**2)+(G/Vr**4))*np.exp
    (-1*(gamma/Vr**2))
    P = (Z*R*T)/V
    P = P*0.1# P in MPa


    rho=(M/V)*1000
    rho= np.asanyarray(rho)
    rho_index=(np.abs((rho) - rho_in)).argmin()
    P=P[rho_index]
    return P
```

H_2O+NaCl Density Equation of State [Mantegazzi et al., 2013]

```
import numpy as np

def eos_nacl_mategazzi2013(T,P,m_NaCl):
        """
        Function based on EOS reported by Mantegazzi et al. 2013
        Input:  T in C,P in MPa and m_Nacl in molal
        Output: density in kg/m3
        Range: 500 MPa to 4500 MPa and up to 1073 K
```

```
        """
        T=T+273.15
        P=P*10**6
        M_H2O=1.008+1.008+15.999
        M_NaCl=22.9898+35.453
        m_H2O=1000/M_H2O
        m_solution=m_H2O+m_NaCl
        X_Nacl=m_NaCl/m_solution
        X_H2O=m_H2O/m_solution

        # constant
        a1=12037.656
        a2=-8.95238
        a3=1.46209*10**-5
        b1=5.65321*10**-3
        b2=5.85867*10**-9
        c1=-21303.205
        c2=10469.393
        d1=-1.09237*10**-12
        d2=0.62224
        e1=4.27249*10**-2
        e2=-1.24044*10**-2
        e3=-2.38016*10**-9
        e4=-951.29641
        e5=1.78313*10**12
        a=(a1+a2*T)+(a3*T**2)
        b=(b1*np.sqrt(P))+(b2*P)
        c=(c1*X_H2O)+(c2*X_H2O**2)
        d=(d1*T*P)+(d2*T*np.log(P))
        e=e1*T*X_H2O*np.log(P)+e2*T*X_H2O*(np.log(P)**2) \
        +e3*T*((1-X_H2O)**2)*P \
        +e4*T*((1-X_H2O)**2)/np.log(P) \
        +e5*((1-X_H2O)**2)/P

        return a+b+c+d+e
```

Dielectric Constant of H_2O

Two correlation formulas are applied in this work. One use the Python implementation of the IAPWS [Fernàndez et al., 1997]:

https://pypi.org/project/iapws/

http://www.iapws.org/release.html

The other correlation formulae reported by Sverjensky et al. [2014]:

```
import numpy as np

def dielectric_constant_h2o(T,density):
        'Compute the dielctric constant of H2O'
        'Input: T in C and denisty in kg/m3'
        'Range: T>100C and P>100MPa using eq. from '
        'Sverjensky et al. (2014)'

                a1=-1.576377*10**-3
                a2=6.810288*10**-2
                a3=7.548755*10**-1
                b1=-8.016651*10**-5
                b2=-6.871618*10**-2
                b3=4.747973
                density=density/1000
                return np.exp((b1*T)+(b2*T**(1/2))+b3)*density**((a1*T)+(a2
   *T**(1/2))+a3)
```

Ion Product of Water [Marshall and Franck, 1981]

```
from  density_H2O import density_H2O
import numpy as np
def logK_H2O_Marshall_Franck1981(T,P):
        """
        Compute logK of H2O = OH- + H+  also called self-ionization
   constant  (Marshall and Franck (1981))
    Need: density model of pure water (density_H2O)
        Input: T in C and P in MPa
        Output: log K is a dimensionless quantity
```

```
        """
        A=-4.098
        B=-3245.2
        C=223620
        D=-3.984*10**7
        E=13.957
        F=-1262.3
        G=856410
        rho = density_H2O(T,P)*10**-3
        T=T+273.15
        return  ((A+(B/T+C/(T**2))+(D/(T**3)))+(E+(F/T)+(G/(T**2)))*np.log10(rho))*-1
```

Thermodynamic Regression Models

RB-Model [Ryzhenko et al., 1985, Shvarov and Bastrakov, 1999, Shvarov, 2008]

modified

```
from logK_H2O_Marshall_Franck1981 import logK_H2O_Marshall_Franck1981
def ryzhenko_bryzgalin_modle(logK_ambient,T,P,A,B)
        """
        LogK regession model by Ryzhenko et. al 1985 and modified by Shvarov and Bastrakov 1999
      Need: logK_H2O model
        Input: logK_i at ambient conditions, T in C, P in MPa, fit parameter  A and B
        Output: logK_i at P/T is a dimensionless quantity
         """
        T=T+273.15
        B_function=(dissociation_constants_Marshall_Franck1981(T,P)-dissociation_constants_Marshall_Franck1981(25,0.1)*(298.15/T))/1.0107
        return logK_ambient*(298.15/T)+(B_function*(A+(B/T)))
```

Density Model [Anderson et al., 1991]

```
def log_density_model(density,T,m0,m1,m2,m3,n0,n1,n2):
    """
```

```
    Density Model logK regession model (see Mesmer et al. 1988, Anderson
    1991 and Mannimg 2013, Vol 76)
    Input: density (rho) in kg/m3, T in K, model coefficients
    Output: logK_i at rho   and T   )
    """
    m = m0 + m1*T**-1 + m2*T**-2 + m3*T**-3
    n = n0 + n1*T**-1 + n2*T**-2
    return m + (n * np.log10(density))
```

Activity Model

Debye-Hückel Activity Approach [Anderson, 2009]

Input-file: species.inp

```
# Input file for species.py
# Here fill in the name of the aq. species  e.g. Species:,H,OH,H2CO3,HCO3,
    CO3 (!(m-n-1) compositions)
Species:,H,OH,H2CO3,HCO3,CO3

# Name of the reaction matrix  e.g "input_co2.xlsx" ! no spaces after the
    file name
input_co2.xlsx
```

Main program: species.py

The code is a python transcription of the species.m code by Anderson [2009] and include the Davies equation and the B-dot model. This code need a .xlsx file that include the reaction stoichiometry, å and the DH parameter as the original.

```
# species.py (J. Stefanski 29.11.2018)
# speciation program, patterned after EQBRM (species.m)

#all input data (except species labels) are in a single matrix.
#m is number of species; n is number of rxns; (m-n-1) is number of
    components.

#input matrix size is (m,m+5)
#matrix format:
#==============
```

```
#row 1    : m,n,all other columns zero.
#row 2    : stoichiometric coeffs for rxn 1.
# :
#row n+1 : stoichiometric coeffs for rxn n.
#row n+2 : mass balance  for component 1.
# :
#row m    : mass balance for component (m-n-1).
#row m+1 : (m-n-1) compositions, all other columns zero.
#row m+2 : n K values, all other columns zero.
#row m+3 : m valences.
#%row m+4 : m initial guesses.
#row m+5 : DHA, DHB, all other columns zero.
#row m+6 : m values of anot, if any (not required).
#row m+7 : m values of bdot, if any (not required).
import sys
import os
import numpy as np
import pandas as pd
import datetime
# working directory
work_dir = os.getcwd()
# read .inp
INPUT = [line.rstrip('\n') for line in open('species.inp')]
species=(INPUT[2]).split(",")
data = pd.read_excel(INPUT[5],usecols=range(len(species)-1))
################## MAIN CODEE ########################
#-------------------------------------------
# Input
#-------------------------------------------
data_matrix=data.as_matrix()

m=int(data_matrix[0,0])
n=int(data_matrix[0,1])
coeffs=data_matrix[1:m-1]
mass=data_matrix[n+1:m]
B=np.array([data_matrix[m,0:(m-n-1)]])
K=np.array([data_matrix[m+1,0:n]])
```

```
z=data_matrix[m+2]
a=data_matrix[m+3]
DHA=data_matrix[m+4,0]
DHB=data_matrix[m+4,1]
if species == "":
    print ("Pleace define names of aq. species!")
#use Davies or expanded DH?
if DHB != 0:
    anot=data_matrix[m+5,:]
    bdot=data_matrix[m+6,:]
#expand a into nxm matrix and (n-1)xm matrix
a_n   = np.kron(np.ones((n,1)),a)
a_n_1 = np.kron(np.ones((m-n-1,1)),a)
# clear an old value
gam_n=[]
test=[]
b=[]
Y=[]
#initial gamma values
gam_n=np.ones([n,m])
#-----------------------------------------------
#START ITERATION HERE
#-----------------------------------------------
test=np.ones([m])
j=0
while np.any(test>=1**-10):
    k=[]
    j+=1

    #construct Jacobian matrix of derivatives C
    dK=0.43429*coeffs/a_n
    C=np.vstack((z,mass,dK))
    A=np.vstack((z,mass))

    #construct Y vector
    zm=np.sum(z*a)

```

```
84      i=0
85      while i<(m-n-1):
86          i=i+1;
87          b=-B[i-1]+np.sum(mass[i-1]*a_n_1[i-1])
88
89      bm=b
90      i=0
91      while (i<n):
92          i=i+1
93          k.append(-K[:,i-1]+np.sum(coeffs[i-1]*np.log10(a_n[i-1]))+sum(
        coeffs[i-1]*np.log10(gam_n[i-1])))
94      km=k
95      # sum up zm,bm,km to Y
96      Y=np.vstack((np.array(([zm],[bm])),np.asarray(km)))
97
98      #evaluate deltaa matrix
99      #deltaa=C\Y;
100     deltaa=-1*np.linalg.pinv(C)@(Y) #Moore-Penrose pseudoinverse
101     deltaa=deltaa.reshape(1,len(deltaa)) # vektor shape for python is eseay
        to work with
102
103     #improve estimated compositions
104
105     aold = np.copy(a)
106     i=0
107     while (i<m):
108         i+=1
109         a[i-1]=aold[i-1]+deltaa[:,i-1]
110
111     #%prevent negative compositions
112         if(a[i-1]<=0):
113             a[i-1]=1e-60;
114
115     test=abs((a-aold)/aold)*100
116
117     #expand new a values
118     a_n    = np.kron(np.ones((n,1)),a)
```

```
119     a_n_1 = np.kron(np.ones((m-n-1,1)),a)
120 
121     #calculate new gammas
122     IS=0.5*np.sum(a*z**2)
123     if (DHB!=0):          #if DHB not zero use extended DH
124         loggam=((-DHA*z**2*IS**0.5)/(1+DHB*anot*IS**5))+bdot*IS
125     else:                 #else use Davies
126         loggam=((-DHA*z**2*IS**0.5)/(1+IS**0.5))+0.2*DHA*IS*z**2
127 
128     gam=np.exp(loggam*2.30259); #
129 
130     #expand gamma matrix
131 
132     gam_n=np.kron(np.ones((n,1)),gam)
133 
134     #should converge in less than 200 iterations
135     #if no convergence, try increasing this number. Sometimes works.
136 
137     if (j>=1000000):
138         it=1
139         print('Iterated 100000 times without convergence.')
140         break
141     else:
142         it=0
143 #-----------------------------------------------
144     #END ITERATION
145 #-----------------------------------------------
146 #this section calculates K for each reaction from calculated species
        activities
147 #and compares these with input K values as a check.
148 logact=np.log10(a*gam)
149 k=0
150 while (k < np.size(coeffs,0)):
151     k+=1
152     K1=np.sum(coeffs[k-1]*logact)
153     if (k==1):
154         K2=K1
```

```
155     elif (k>1):
156         K2=np.asarray(K2)
157         K2=np.insert(K2,np.size(K2),K1) # to have one array for next
    calculation
158 
159 #K2 is now a vector of calculated K values.
160 K3 = np.vstack((K2,K))
161 #K3 is a matrix of calculated (row 1) and input (row 2) K values.
162 #if the two rows are identical, speciation is OK.
163 
164 msg=0
165 K4=1-K2/K
166 if np.any(abs(K4)>0.0001):
167     msg=1
168     print ('K values in rxn NG')
169 
170 #output
171 print("\n")
172 print (datetime.date.today())
173 print(work_dir)
174 print("--------------------")
175 if (msg==0):
176     print ('all speciated K values are OK')
177 else:
178     print ('some speciated K values are NG')
179 print("\n")
180 print("Number of iterations:",j)
181 print("Input K",K)
182 print("Calucated K",K3[0])
183 output=np.zeros((m+1,4))
184 values=["Molalities","Gammas","Activities","Species %"]
185 print("\n")
186 for i in range(len(species)):
187     if i==0:
188         print(species[i],"\t",values[0],"\t", values[1],"\t", values[2],"\t
    ",values[3])
189     else:
```

```
190         print (species[i],"\t\t",'%.4E' % a[i-1],"\t",'%.4E' % gam[i-1],"\t
    ",
191                 '%.4E' % (a[i-1]*gam[i-1]),"\t",'%2.2f' % ((a[i-1]/np.sum(a)
    )*100))
192 print ("\n pH:",(-np.log10(a[0]*gam[0])))
193 # Export resultsiii outout.dat
194 f=open('output.dat','w')
195 f.write(str(datetime.date.today())+"\n")
196 f.write(work_dir)
197 f.write(" \n")
198 f.write("--------------------")
199 f.write(" \n")
200 if (msg==0):
201     f.write('all speciated K values are OK\n')
202 else:
203     f.write('some speciated K values are NG\n')
204 if (it==1):
205     f.write("Iterated 100000 times without convergence.\n")
206 else:
207     f.write("Number of iterations:" +  str(j) + "\n")
208 f.write("Input K" + str(K) + "\n")
209 f.write("Calucated K" + str(K3[0]) + "\n")
210 output=np.zeros((m+1,4))
211 values=["Molalities","Gammas","Activities","Species %"]
212 f.write("\n")
213 for i in range(len(species)):
214     if i==0:
215         f.write(str(species[i])+"\t"+str(values[0])+"\t"+str(values[1])+"\t
    \t"
216     +str(values[2])+"\t"+str(values[3])+"\n")
217     else:
218         f.write(str(species[i])+"\t\t"+str('%.4E' % a[i-1])+"\t"+str('%.4E'
     % gam[i-1])+"\t"+
219                 str('%.4E' % (a[i-1]*gam[i-1]))+"\t"+str('%2.2f' % ((a[i-1]/
    np.sum(a))*100))+"\n")
220 f.write("\n pH:"+ str(-np.log10(a[0]*gam[0])))
221 f.close()
```

ERKLÄRUNG DER EIGENSTÄNDIGKEIT

Ich versichere, dass ich die von mir vorgelegte Dissertation selbständig angefertigt, die benutzten Quellen und Hilfsmittel vollständig angegeben und die Stellen der Arbeit - einschließlich Tabellen, Karten und Abbildungen -, die anderen Werken im Wortlaut oder dem Sinn nach entnommen sind, in jedem Einzelfall als Entlehnung kenntlich gemacht habe; dass diese Dissertation noch keiner anderen Fakultät oder Universität zur Prüfung vorgelegen hat; dass sie - abgesehen von oben angegebenen Teilpublikationen - noch nicht veröffentlicht worden ist sowie, dass ich eine solche Veröffentlichung vor Abschluss des Promotionsverfahrens nicht vornehmen werde. Die Bestimmungen der Promotionsordnung sind mir bekannt. Die von mir vorgelegte Dissertation ist von Prof. Dr. Jahn betreut worden.

Ort, Datum

Johannes Stefanski